Nonlinear optics in chip-based microresonators and their applications

Thesis by

Myoung-Gyun Suh

In Partial Fulfillment of the Requirements

for the Degree of

Doctor of Philosophy in Applied Physics

CALIFORNIA INSTITUTE OF TECHNOLOGY

Pasadena, California

2017

(Defended May 25, 2017)

Myoung-Gyun Suh

ORCID: 0000-0002-9527-0585

To my parents,

Byoung-Kil and In-Sook,

and my beloved family,

Hui-Chen, Violet and Chloe.

Acknowledgments

This thesis is the result of my PhD program at Caltech and my life in a new environment: the United States. This important outcome of my life comes into the world not only by me, but by many people who collaborated with me, and advised and mentally supported me. I sincerely thank all of them.

First of all, I would like to thank my advisor Prof. Kerry Vahala for his guidance and support throughout my PhD program. I am grateful for him having provided me with invaluable advice and I feel very fortunate to have had the opportunity to be a part of his lab. Also, his passion for science and good personality will remain in my memory as a good example of a true scholar.

I would also like to thank Profs. Oskar Painter, Keith Schwab, and Andrei Faraon for their support and advice during my graduate study at Caltech. As a student and a teaching assistant, I could learn a lot both academically and personally from the interactions I had with them. Similarly, I want to thank Dr. Scott Diddams. His research always inspired me and I enjoyed the discussions with him during his visit to Caltech in 2012. His comments on the spiral reference cavity project particularly helped me to successfully finish the first project in my PhD study.

Senior lab members, Jiang Li, Tong Chen, and Hansuek Lee, who already left Vahala lab, are who I want to thank. Their research and effort in the lab were the steppingstones of my PhD research, and discussion with them educated me during my early PhD years. I also thank the current lab members, Ki Youl Yang, Dongyoon Oh, Seunghoon Lee, Xu Yi, Yu-Hung Lai, Qi-Fan Yang, Boqiang Shen, Heming Wang, and Xinbai Li. Their work always inspired me, and the support that I received in many ways made my PhD life much easier. The collaboration and discussion with them also made me grow intellectually.

My thanks to Melissa Melendes, Guy DeRose, and many other KNI staff. Without their help, I couldn't have made any devices for my research. My thanks to Cecilia Gamboa, Christy Jenstad, Connie Rodriguez, and Jennifer Blakenship. Without their support, I couldn't survive at Caltech.

Thanks to Dongwan Kim and Hyunsik Kim, my dear Korean friends who entered the

APhMS department in the same year. Our enjoyable discussions and the interaction enriched my life on campus. Lastly, thank you to my neighbors the Sinchul Yeom family, Sungwook Woo family, Daniel and Claire Thomas family, Seungil You family, Euncheol Shin family, and the Yonil Jung family. The difficult time in my life as a parent and a PhD student at the same time was easier because I have comrades like them.

Lastly, I'd like to thank my parents and family. Their love and support were the driving force of my research and what make this thesis meaningful for me.

Abstract

Optical micro-resonators have been studied for decades as a platform to investigate optical physics, and to miniaturize bulky optical systems. In the last decade, optical frequency combs, which have revolutionized the precision measurement of time and frequency, have been demonstrated in optical micro-resonators via the combined effect of parametric oscillation and cascaded four-wave mixing. More recently, soliton mode-locking has made possible low-noise/reproducible generation of these miniature combs (microcombs). In this thesis, we demonstrated the generation of soliton microcombs from silica wedge disk micro-resonators and the characteristics of the soliton microcombs are described. We also applied soliton microcombs to dual-comb spectroscopy and distance measurement (LIDAR) for the first time. Also, ways to improve spectral resolution, signal-to-noise ratio, and spectral coverage are discussed. In addition to soliton microcombs, a novel spiral resonator is studied as a stable optical frequency reference. Combined with a frequency comb, this new type of chip-based reference cavity is also applied to generate stable microwaves via optical frequency division. Lastly, we generated a stimulated Brillouin laser (SBL) from the optical micro-resonator and its phonon-limited linewidth is studied. Application of the SBL for rotation measurement is also demonstrated. This thesis is organized into six chapters. Throughout the thesis, the implication and potential of my PhD work toward chip-based advanced optics system are discussed.

In chapter 1, the research field of optical microresonators is briefly reviewed. The basic concepts and terminology of the research topics in this thesis are also introduced. The fabrication process and characteristics of the typical silica wedge disk resonator are also described.

In chapter 2, conventional optical frequency comb technology is overviewed and the emerging microresonator-based comb technology is introduced. Generation and characteristics of soliton microcombs from silica wedge disk microresonators are also described.

In chapter 3, application of microresonator soliton to dual-comb spectroscopy is described. Detection of $H^{13}CN$ is demonstrated and detection of CH_4 by expanding spectral coverage via Raman stokes process is discussed. Approaches to improve spectral resolution

and signal-to-noise ratio are also discussed.

In chapter 4, application of microresonator soliton to distance detection is described. Time-of-flight measurement is demonstrated using the chip-based dual-soliton source from a single pump laser and a single microresonator.

In chapter 5, laser frequency stabilization and low-noise microwave generation are demonstrated using on-chip spiral reference cavity. The theoretical noise limit of the spiral reference cavity is also discussed.

In chapter 6, stimulated Brillouin lasers generated from optical microresonators are introduced and the phonon-limited linewidth at cryogenic temperature is studied. Application of the stimulated Brillouin laser to gyroscope is also described.

Published Contents and Contributions

(Journal papers)

[1] Lee, Hansuek, Myoung-Gyun Suh, Tong Chen, Jiang Li, Scott A. Diddams, and Kerry J. Vahala. "Spiral resonators for on-chip laser frequency stabilization." *Nature communications* 4 (2013). DOI: 10.1038/ncomms3468

M.G.S built the experimental setup, measured the devices, analyzed the data, and participated in the writing of the manuscript.

[2] Yi, Xu, Qi-Fan Yang, Ki Youl Yang, Myoung-Gyun Suh, and Kerry Vahala. "Soliton frequency comb at microwave rates in a high-Q silica microresonator." *Optica* 2, no. 12 (2015): 1078-1085. DOI: 10.1364/OPTICA.2.001078

M.G.S participated in the measurement of devices and the analysis of the data.

[3] Suh, Myoung-Gyun, Qi-Fan Yang, Ki Youl Yang, Xu Yi, and Kerry J. Vahala. "Microresonator soliton dual-comb spectroscopy." *Science* 354, no. 6312 (2016): 600-603. DOI: 10.1126/science.aah6516

M.G.S participated in the conception of the project, built the experimental setup, measured the devices, analyzed the data, and participated in the writing of the manuscript.

[4] Li, Jiang, Myoung-Gyun Suh, and Kerry Vahala. "Microresonator Brillouin gyroscope." *Optica* 4, no. 3 (2017): 346-348. DOI: 10.1364/OPTICA.4.000346

M.G.S participated in the conception of the project, fabricated the devices, and participated in the writing of the manuscript.

(Conference papers)

[1] Suh, Myoung-Gyun, Hansuek Lee, Jiang Li, Scott Diddams, and Kerry Vahala. "Stablization of fiber lasers using chip-based high-Q optical resonators." *Conference on Lasers and Electro-Optics (CLEO)*, pp. 1-2. IEEE, 2013. DOI: 10.1364/CLEO_SI.2013.JM2N.4

M.G.S built the experimental setup, measured the devices, analyzed the data, and participated in the writing of the manuscript.

[2] Li, Jiang, Myoung-Gyun Suh, and Kerry Vahala. "Microresonator Brillouin Gyroscope." *Nonlinear Optics*, pp. NTh3A-2. Optical Society of America, 2015. DOI: 10.1364/NLO.2015.NTh3A.2

M.G.S participated in the conception of the project, fabricated the devices.

[3] Yang, Qifan, Xu Yi, Ki Youl Yang, Myoung-Gyun Suh, and Kerry Vahala. "Microwave-Rate Soliton Mode-Locking on a Chip." *Nonlinear Optics*, pp. NTh3A-8. Optical Society of America, 2015. DOI: 10.1364/NLO.2015.NTh3A.8

M.G.S participated in the measurement of devices and the analysis of the data.

[4] Yi, Xu, Qi-Fan Yang, Ki Youl Yang, Myoung-Gyun Suh, and Kerry Vahala. "Demonstration of a soliton frequency comb in a high-Q silica microresonator." *Conference on Lasers and Electro-Optics (CLEO)*, pp. 1-2. IEEE, 2016. DOI: 10.1364/CLEO_SI.2016.STu3Q.5

M.G.S participated in the measurement of devices and the analysis of the data.

[5] Li, Jiang, Myoung-Gyun Suh, and Kerry Vahala. "Stimulated Brillouin laser microcavity gyroscope." *IEEE Photonics Conference (IPC)*, pp. 345-346. IEEE, 2016. DOI: 10.1109/IPCon.2016.7831129

M.G.S participated in the conception of the project, fabricated the devices.

[6] Suh, Myoung-Gyun, Qi-Fan Yang, Ki Youl Yang, Xu Yi, and Kerry J. Vahala. "Microresonator Soliton Dual-Comb Spectroscopy." *Frontiers in Optics*, pp. FF2C-2. Optical Society of America, 2016. DOI: 10.1364/FIO.2016.FF2C.2

M.G.S participated in the conception of the project, built the experimental setup, measured the devices, analyzed the data, and participated in the writing of the manuscript.

[7] Spencer, Daryl T., et al. "Towards an Integrated-Photonics Optical-Frequency Synthesizer With¡ 1 Hz Residual Frequency Noise." *Optical Fiber Communication Conference*, pp. M2J-2, Optical Society of America, 2017. DOI: 10.1364/OFC.2017.M2J.2

M.G.S fabricated the devices.

[8] Qi-Fan Yang, Myoung-Gyun Suh, Ki Youl Yang, Xu Yi, and Kerry J. Vahala. "Microresonator Soliton Dual-Comb Spectroscopy." *Conference on Lasers and Electro-Optics (CLEO)*, pp. SM4D.4, IEEE, 2017. DOI: 10.1364/CLEO_SI.2017.SM4D.4

M.G.S participated in the conception of the project, built the experimental setup, measured the devices, analyzed the data, and participated in the writing of the manuscript.

[9] Erin S. Lamb, Jordan R. Stone, Myoung-Gyun Suh, Kerry Vahala, Scott Diddams, Scott Papp. "Octave broadening of a 15 GHz Kerr soliton comb." *Conference on Lasers and Electro-Optics (CLEO)*, pp. SF1C.4, IEEE, 2017. DOI: 10.1364/CLEO_SI.2017.SF1C.4

M.G.S fabricated the devices.

(Patents)

[1] Vahala, Kerry, Tong Chen, Lee Hansuek, and Myoung-gyun Suh. "On-chip optical reference cavity exhibiting reduced resonance center frequency fluctuations." *U.S. Patent 8,848,760*, issued September 30, 2014.

M.G.S built the experimental setup, measured the devices, and analyzed the data.

Table of Contents

Acknowledgments iv

Abstract vi

Published Contents and Contributions viii

Table of Contents xiii

List of Figures xvi

1 Optical Microresonators **1**

1.1 Introduction 1

1.2 Silica Wedge Optical Microresonators 2

1.2.1 Fabrication Process 3

1.2.2 Optical Mode Structure 5

1.3 Coupling Light into Microresonator via Tapered Fiber 6

1.4 Quality Factor 9

1.5 Nonlinear Phenomena in Optical Microresonators 11

1.5.1 Parametric Oscillation and Four-Wave Mixing 11

1.5.2 Stimulated Brillouin Scattering 11

2 Microresonator-based Optical Frequency Comb **14**

2.1 Introduction to Optical Frequency Comb 14

2.2 Generation of Optical Frequency Combs from Microresonators 17

2.3 Soliton Mode Locking in Microresonators 20

2.3.1 Soliton Generation 20

2.3.2 Breather-to-Soliton Transition 25

3 Microresonator Soliton Dual-Comb Spectroscopy **29**

3.1 Introduction 30

3.2 Microresonator-based Dual-Soliton Source and $H^{13}CN$ Detection 32

3.2.1 Microresonator-based Dual-Soliton Generation 32

3.2.2 Interferogram and Initial Spectroscopic Test 34

3.2.3 Detection of $H^{13}CN$ $2\nu_3$ Absorption Band 37

3.3 Higher Spectral Resolution : Lower Repetition Rate Solitons 40

3.4 Higher Signal-to-Noise Ratio : Dual-Soliton Source from Single Microresonator. 43

3.5 Expanding Spectral Coverage : Stokes Soliton and Methane (CH_4) Detection 47

4 Microresonator Soliton LIDAR **53**

4.1 Introduction 53

4.2 Distance Measurement using Microresonator Dual-Soliton Source 55

4.2.1 Time-Of-Flight Distance Measurement 59

4.2.2 Precision of Distance Measurement and Resolving Ambiguity Range 61

5 On-Chip Spiral Reference Cavity : Frequency Stabilization and Low-Noise Microwave Generation **65**

5.1 Introduction 66

5.2 Optical Characteristics of Spiral Reference Cavity 67

5.3 Frequency Stabilization using Spiral Reference Cavity 71

5.4 Theoretical Noise Limit of Spiral Reference Cavity 76

5.5 Low-Noise Microwave Generation via Optical Frequency Division 82

6 Stimulated Brillouin Laser from Optical Microresonator **90**

6.1 Introduction 90

6.2 The Phonon-Limited-Linewidth of Brillouin Lasers at Cryogenic Temperatures 92

6.3 Application of Chip-based Stimulated Brillouin Laser : Microresonator Brillouin Gyroscope 102

Bibliography **108**

List of Figures

1.1 **Silica optical microresonators** . . . 3
1.2 **Fabrication process of silica disk resonator** . . . 4
1.3 **Cross section of device and optical modes** . . . 5
1.4 **Fiber taper profile and pulling setup** . . . 6
1.5 **Tapered-fiber coupling setup** . . . 8
1.6 **Example of quality(Q)-factor measurement** . . . 10
1.7 **Schematic of backward stimulated Brillouin scattering.** . . . 12

2.1 **Concept of optical frequency combs** . . . 15
2.2 **Various material systems generating microcombs** . . . 17
2.3 **Principle of microcomb generation** . . . 18
2.4 **Typical optical spectra of microcomb** . . . 19
2.5 **Soliton generation setup** . . . 21
2.6 **Oscilloscope traces showing controllable soliton mode locking via direct laser frequency tuning** . . . 22
2.7 **Optical spectra of four different soliton states** . . . 24
2.8 **Generation of soliton and breather soliton** . . . 25
2.9 **Transition from breather soliton to soliton** . . . 26
2.10 **Oscillation in comb power at different breathing frequencies** . . . 27
2.11 **Transition from breather to Stokes soliton** . . . 28

3.1 **Microresonator-based dual-comb spectroscopy** . . . 31
3.2 **Detailed experimental setup** . . . 33
3.3 **Soliton comb spectral charaterization** . . . 34

3.4 **Measured electrical interferogram and spectra** 35
3.5 **Measured molecular absorption spectra** 39
3.6 **Simulated absorption spectra with varying free spectral range (FSR)** . . 40
3.7 **Soliton microcombs with narrower FSR** 42
3.8 **Dual-soliton generation from single microresonator** 44
3.9 **Characteristics of dual-soliton source** 46
3.10 **Primary-Stokes mode pair analysis using COMSOL** 48
3.11 **Stokes soliton for Methane R-branch detection** 49
3.12 **Stokes solitons for Methane Q-branch detection** 50
3.13 **Counter-Propagating Stokes soliton for Methane Q-branch detection** . . 52

4.1 **Experimental setup for dual-soliton generation and LIDAR measurement** 56
4.2 **Characteristics of microresonator dual-soliton source** 58
4.3 **Distance measurement** 60
4.4 **Precision of distance measurement versus averaging time** 62
4.5 **Resolving range ambiguity** 63

5.1 **Photograph of spiral waveguide resonators** 68
5.2 **Measured Q factor versus resonator length in meters** 70
5.3 **Experimental setup for laser frequency stabilization** 72
5.4 **Phase noise spectra and linewidth measurement** 73
5.5 **Allan deviation measurement result** 75
5.6 **Packaged silica spiral resonator and experimental setup for laser frequency stabilization** 77
5.7 **Electrical spectra and phase noise spectra of the frequency-stabilized fiber lasers** 79
5.8 **Allan deviations of the frequency-stabilized fiber lasers** 81
5.9 **Experimental setup for optical frequency division using a spiral reference cavity** 84
5.10 **Phase noise spectra of the heterodyned two fiber lasers near 1550 nm** . . 86

5.11 **Stable microwave generation via optical frequency division** 87

6.1 **Experimental setup and Brillouin laser action** 93
6.2 **Picture of the open-loop continuous-flow cryostat system** 94
6.3 **Aligning the 3$^{\mathrm{rd}}$ Stokes wave to the Brillouin gain spectrum maximum** . . 96
6.4 **Measured Brillouin gain coefficient (g_0)** 98
6.5 **Estimation of SBL linewidth and n_T from phase noise measurements** . . 100
6.6 **Principle of Brillouin laser gyroscope operation and experimental setup** . 103
6.7 **Packaged microresonator billouin gyroscope and output voltage oscillation from sinusoidal rotation** 105
6.8 **Rotation sensitivity of microresonator Brillouin gyroscope** 106

Chapter 1

Optical Microresonators

Optical microresonators have been studied for over two decades and the interest in this research field is ever increasing with the advancement of micro/nano fabrication technologies. This subject of research has distinct and rich optical physics, and the applications of optical microresonators have huge implication on miniaturization of bulky optical systems and potential integration on a chip similar to the case of electronics. This chapter briefly reviews the role of optical microresonators in integrated optics, and introduces silica wedge disk resonators which are studied in this thesis. Basic concepts and background knowledge are also introduced.

1.1 Introduction

Conventional optical components in free-space and fiber optics are large compared with the wavelength, and this limits their density of integration. With the success of semiconductor industry, advances in micro/nano fabrication technologies allowed us to make optical structures with sizes in the order of the optical wavelength. In this wavelength-order size limit, optical components can be integrated similar to integrated microwave components. The ideas of optical circuits and design concept in the integrated optics are originated from microwave circuits due to the similarity. For integrated optical circuits, researchers have demonstrated and developed various optical components, such as waveguide, add/drop filter, splitter, polarization splitter-rotator, and grating coupler. In these integrated optics, mircoresonators are used for various purposes, such as cavities for laser emission and add/drop

filters, and have a crucial role.

Optical microresonators not only miniaturize optical components, but also significantly increase the optical field intensity by confining light to small volumes by resonant recirculation. The high optical field intensity can allow the study of cavity quantum electrodynamics (QED) and many optical nonlinear phenomena, such as parametric oscillation and stimulated brillouin scattering. Recently, application area of microresonators has expanded to sensors and metrology and various types of microresonators (microsphere, ring resonator, toroid, wedge-disk resonator, ridge-disk resonator, etc.) are demonstrated in many material systems. In this thesis, we'll study silica wedge disk resonators fabricated on a silicon wafer, which will be introduced in the next section.

1.2 Silica Wedge Optical Microresonators

Achieving high optical Q-factor in microresonators relies critically on two things: low material absorption loss at the wavelength and low surface scattering loss. Although microresonators made of crystalline materials (MgF_2,CaF_2, etc.) provide Q-factors greater than 10^9, silica provides the lowest material loss (highest-Q) among chip-based microresonators. Making the resonator surface smooth is also very important. Among chip-based silica resonators, silica microtoroid resonators show very high Q-factor and finesse (free spectral range divided by cavity linewidth) because the reflow process utilizes the surface tension to make a smooth surface. However, the reflow process is not scalable and hard to use to make large devices. Moreover, the reflow process makes it difficult to precisely control the size of the resonators.

Recently, silica wedge disk resonator with the Q-factor as high as 875 million is reported [1]. This device is scalable to larger size (millimeter/centimeter scale) and the size is precisely controllable. As shown in figure 1.1, the silica wedge disk microresonators with various sizes and designs are fabricated and used for the studies in this thesis.

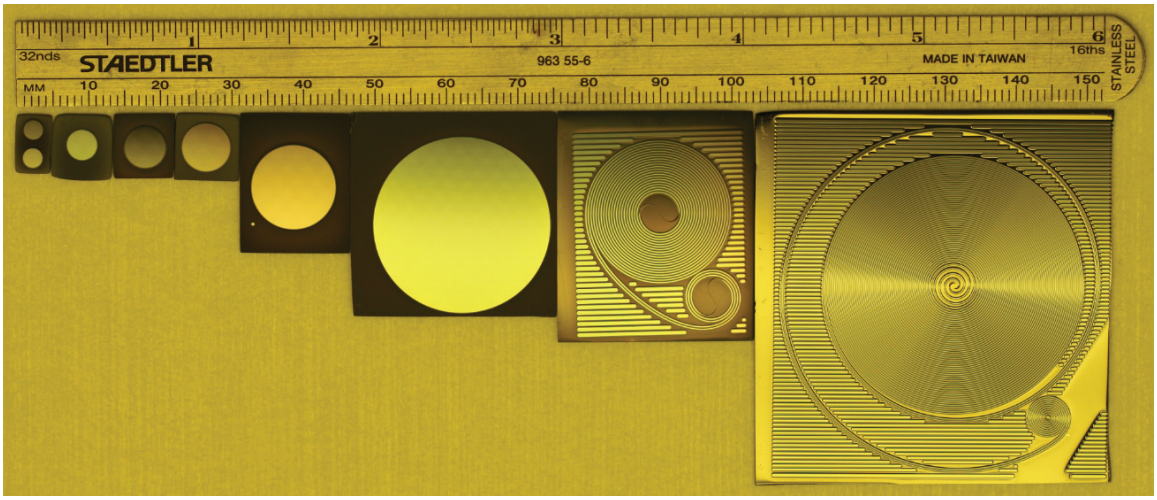

Figure 1.1: **Silica optical microresonators** silica wedge disk resonotors with various diameters (3 mm, 4.5 mm, 6 mm, 7 mm, 12 mm, 24 mm) and spiral resonators with the roundtrip lengths 1.2 m and 4 m (from left to right). The devices are whispering-gallery-mode resonators, which guide light at the silica wedge.

1.2.1 Fabrication Process

The process flow chart for the fabrication of silica wedge microresonators is shown in figure 1.2. An 8-micron-thick silica layer is thermally grown on a 4-inch (100) prime-grade float-zone silicon wafer. Disk patterns are defined through standard photolithographic methods: Spin coating of the photoresist (S1813), soft baking, UV exposure (Either MA6 aligner or GCA 6300 stepper), post-exposure hard baking, and developing using MF-319. After the photolithography, the photoresist disk pattern is transfered onto the silica layer by buffered hydrofluoric acid wet etching. Wet etching time for 8 μm silica layer is 80 $\sim$ 90 minutes, but the etching time is typically extended to 120 min $\sim$ 180 min to make a smoother etch surface and control the diameter and wedge angle of the device. Wedge angle increases a few degrees as the wet etch time is increased from 120 min to 180 min. After the HF etching, the conventional organic cleaning process is followed to remove the photoresist layer using Remover PG, Acetone and IPA. Finally, silicon substrate is isotropically etched by xenon difluoride (XeF_2) to create air cladding around the silica wedge region where the optical whispering-galley-modes are confined.

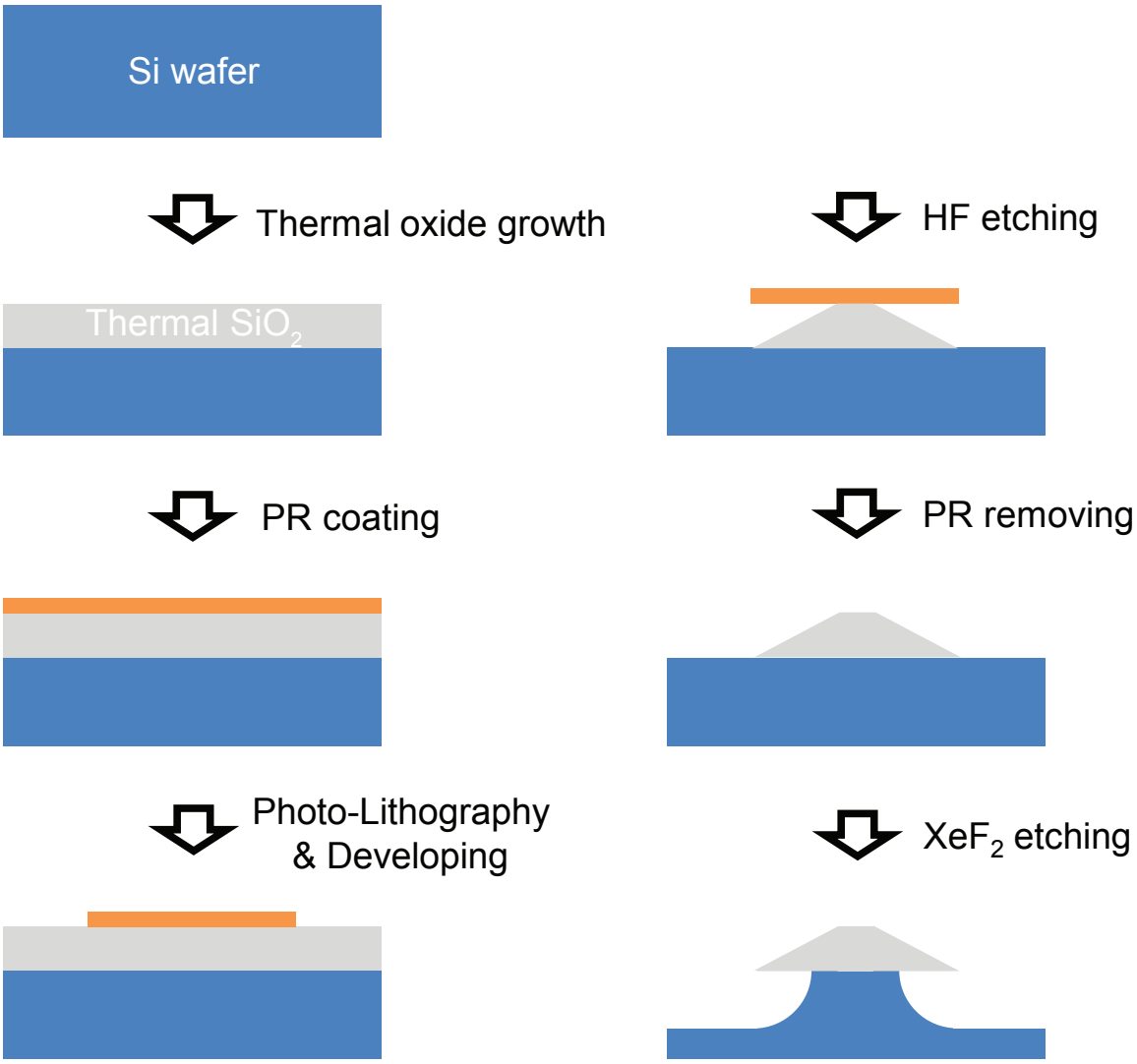

Figure 1.2: **Fabrication process of silica disk resonator** Starting from thermal oxide growth (typically ~ 8 μm) on a crystalline silicon wafer, a photoresist layer is coated on the silica layer for standard photo-lithography. 2-dimensional resonator pattern is transferred from a chrome-coated quartz mask onto the photoresist. Buffered hydrofluoric acid wet etching transfers the photoresist pattern onto the oxide layer and the photoresist layer is removed via organic cleaning. Final whispering-gallery mode silica resonator is made by creating an air-cladding around the silica wedge through Xenon difluoride isotropic etching of silicon underneath the silica wedge.

1.2.2 Optical Mode Structure

Figure 1.3(a) shows the SEM image of the device cross section. The silica disk has a wedge-shaped feature at the circumference as shown in figure 1.3(b). The wedge angle of the device in the SEM image is around 20 degrees, but can be controlled by adjusting the surface energy of the photoresist. Typically, adhesion promoter (e.g. HMDS), baking temperature, and HF etching time are used for the wedge angle control.

Figure 1.3(c) shows various optical whispering-gallery-modes supported by the 20 degree wedge resonator device. COMSOL is used for the simulation and the electric field intensities of the different transverse optical modes are shown. Each transverse mode has its own longitudinal mode family with a similar cross-sectional mode profile.

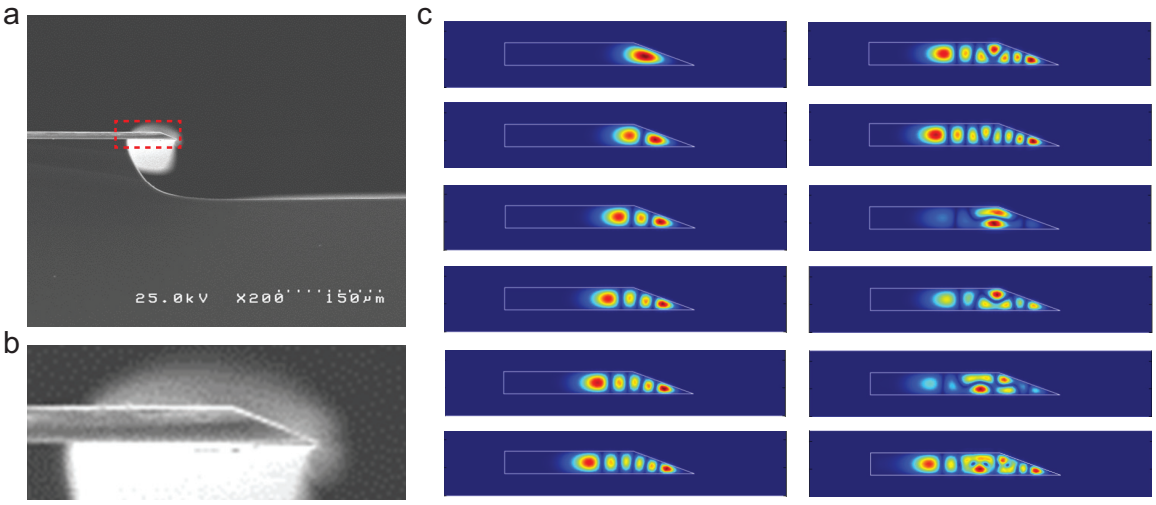

Figure 1.3: **Cross section of device and optical modes.** (a) SEM image showing the cross section of the silica wedge resonator. (b) Zoom-in of the red dotted box in (a). (c) Various simulated optical modes guided by the silica wedge. The simulated device has $\sim$ 8 μm thickness, 6 mm diameter, and 20 degree wedge angle.

1.3 Coupling Light into Microresonator via Tapered Fiber

Efficient coupling of the whispering gallery modes is a prerequisite for studying optical microresonators. Since the fundamental whispering gallery modes are confined by the wedge surface of our silica microresonators, evanescent coupling techniques can provide powerful means in controlling the coupling properties. Tapered optical fibers allow both efficient excitation and extraction of optical power from the same fiber, while maintaining fiber-optic compatibility[2, 3].

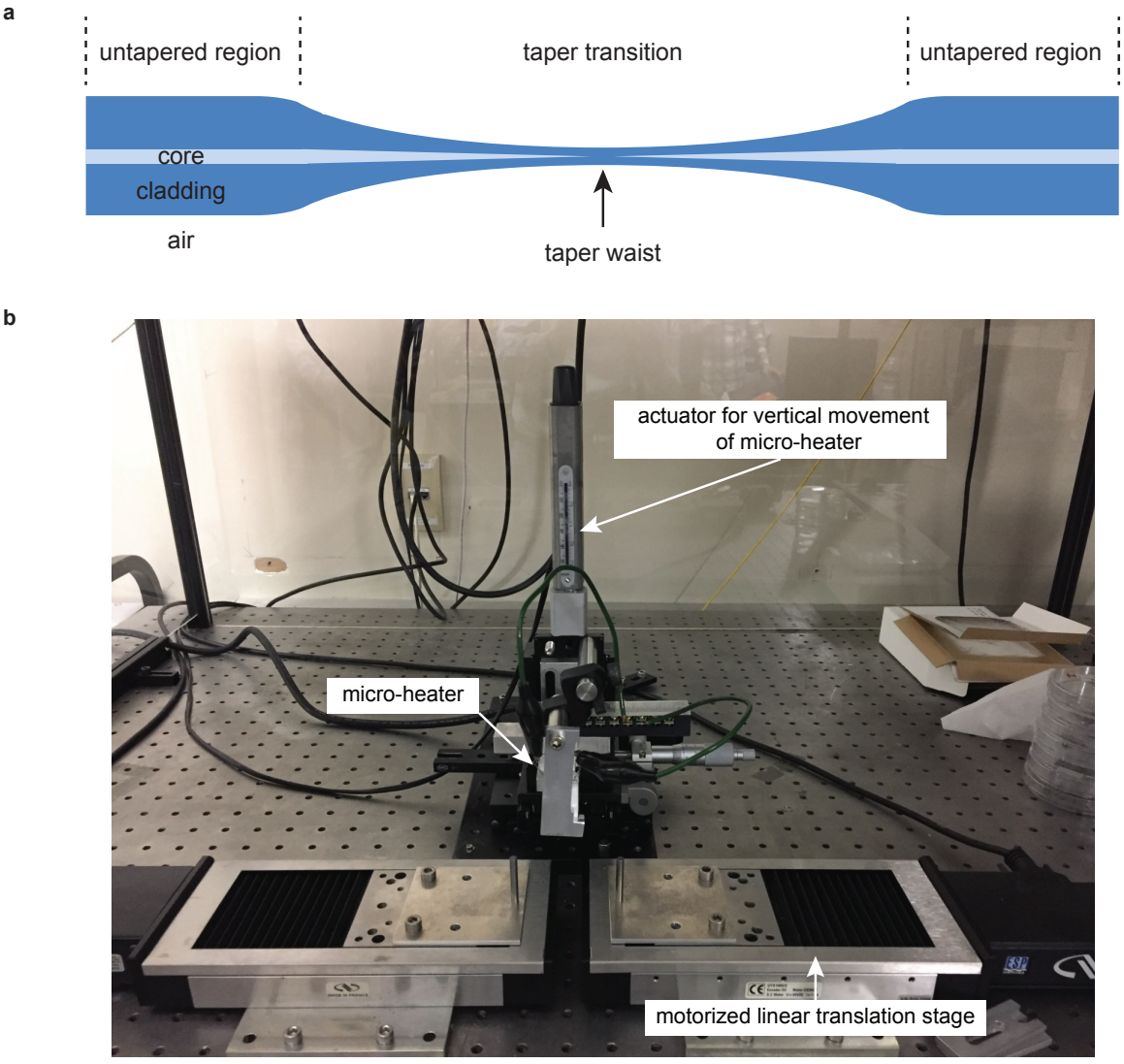

Figure 1.4: **Fiber taper profile and pulling setup** a. Schematic profile of fiber taper. b. Fiber taper pulling setup.

Tapered optical fibers are made by heating a single-mode fiber (typically SMF-28 for the wavelength near 1550 nm) using a microheater and slowly pulling the fiber apart until a waist region only a few microns in diameter is created. Transferable fiber holding stage is used to pull the tapered fiber and hold the tapered fiber during our experiments. The heating temperature is typically $>$ 1000 degree C and the pulling speed is $\sim$ 3 mm / min. The taper profile is adjusted by varying the heating temperature and pulling speed. By maintaining an adiabatic taper profile, an initially launched fiber mode is converted to an air-guided taper mode and converted back to the fiber mode upon propagating through the tapered region. Tapers used in our work typically have losses less than 0.5 dB. The schematic diagram of tapered fiber profile is illustrated in figure 1.4(a) and the taper pulling setup used in this work is shown in figure 1.4(b).

Coupling laser light into the microresonator requires three conditions. First, the evanescent field of the fiber taper and the microresonator should spatially overlap. Second, the frequency of laser light must be resonant with the WGM mode of the microresonator. Finally, the propagation constants of the taper and WGM mode should be matched (phase-matching). In the experiment, phase matching can be done by adjusting the position of tapered fiber that is coupled to the microresonator. Figure 1.5(a) shows a typical tapered fiber coupling setup, which consists of tapered fiber, tapered fiber holder, a microscope to monitor the relative position of tapered fiber and resonator, XYZ stage to adjust the relative position of the device from the tapered fiber, and the thermoelectric cooler (TEC) to control the temperature of the device. Figure 1.5(b) is the top view of the device at the tapered fiber coupling region monitored through the microscope. Figure 1.5(c) shows the entire microresonator sitting on the TEC element.

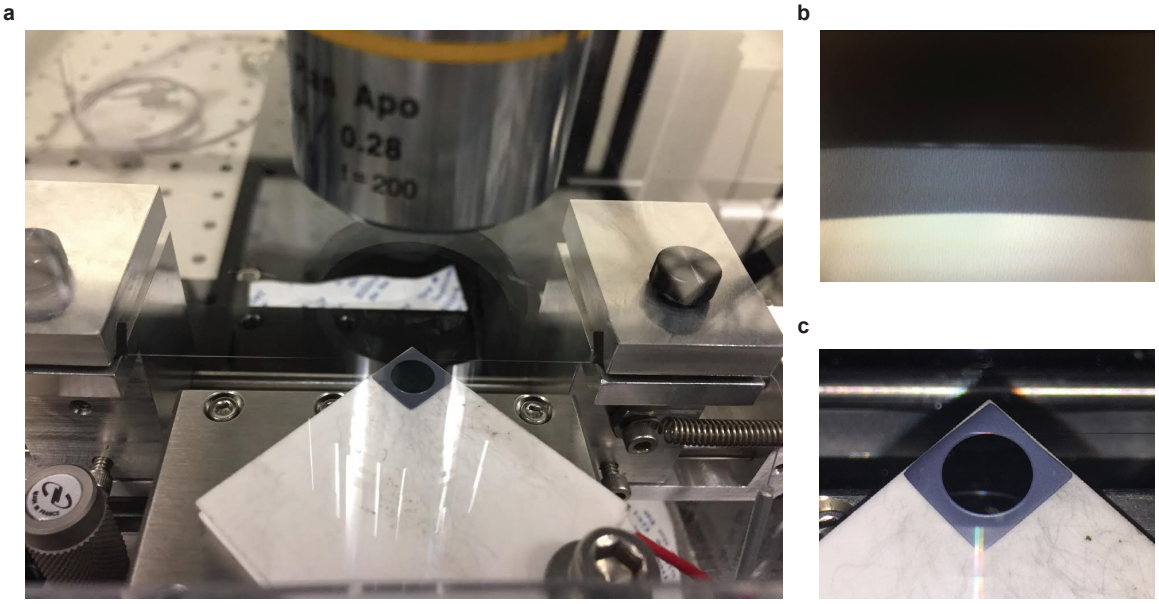

Figure 1.5: **Tapered-fiber coupling setup** a. Silica resonator is place on the XYZ stage to change the its relative position from the tapered-fiber suspended by a separate fiber holder. The coupling area is monitored via a microscope above the system. Thermoelectric cooling and heating unit is installed on the XYZ stage to tune the temperature of the resonator. b. Zoomed-in top view seen through the microscope. To couple laser light into the resonator, the taperd fiber contacts on the silica microresonator near the silica wedge where whispering-gallery-modes exist. c. Typical silica wedge disk resonator sitting on the tapered-fiber coupling setup.

1.4 Quality Factor

Quality (Q) factor is an universal measure to characterize numerous resonating systems. The general definition of the Q factor is

$$Q = 2\pi \times \frac{\text{Energy stored}}{\text{Energy loss per cycle}}. \tag{1.1}$$

It quantifies how many cycles the input signal can stay inside the resonator until it lose half of its energy, and it also characterizes the resonance frequency of a resonator relative to its linewidth.

$$Q = \frac{\omega}{\Delta\omega}, \tag{1.2}$$

where ω is the resonance frequency and $\Delta\omega$ is the full-width at half-maximum (FWHM) of the resonance lineshape.

Optical Q-factor is the most commonly used and important specification of optical microresonators studied in this thesis. Q-factor of the silica wedge disk resonator microresonators mainly depends on the material absorption loss and the surface scattering loss, which can vary with the geometry of devices (thickness, diameter, wedge angle, etc.) and the surface roughness due to imperfect fabrication process. Figure 1.6 shows how the Q-factor of the microresonators is measured. Briefly, pump laser is coupled to the microresonator via a tapered fiber and the transmitted pump laser intensity is monitored while the laser frequency is swept. Relative frequency is measured by Mach-Zehnder interferometer (MZI). The linewidth of the resonance is obtained by Lorentzian fit of the resonance dip in the transmitted laser power intensity. The typical Q-factor of the microresonators in this study is 10 million $\sim$ 500 million.

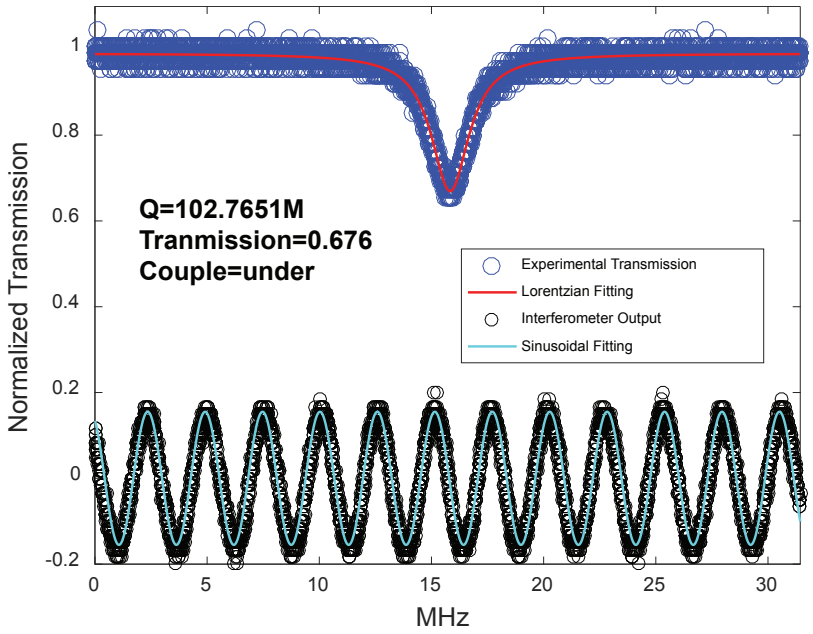

Figure 1.6: **Example of quality(Q)-factor measurement.** Typical oscilloscope traces for the Q-factor measurement are shown. Pump laser is coupled to the microresonator and the transmitted pump laser intensity(blue circles) is monitored while the laser frequency is swept. Relative frequency is measured by Mach-Zehnder interferometer (MZI) with 2.56 MHz period as shown in black circles. The transmitted pump laser intensity trace and MZI trace are fitted using Lorentzian function and sinusoidal function, respectively. Q-factor is estimated from the linewidth and coupling depth of the resonance dip.

1.5 Nonlinear Phenomena in Optical Microresonators

1.5.1 Parametric Oscillation and Four-Wave Mixing

For a material in general, the electric polarization (P) depends on the electric field (E). In a simple mathematical form,

$$P_i = \varepsilon_0 \sum_{j=1}^{3} \chi_{ij}^{(1)} E_j + \varepsilon_0 \sum_{j=1}^{3}\sum_{k=1}^{3} \chi_{ijk}^{(2)} E_j E_k + \varepsilon_0 \sum_{j=1}^{3}\sum_{k=1}^{3}\sum_{l=1}^{3} \chi_{ijkl}^{(3)} E_j E_k E_l + \cdots , \quad (1.3)$$

where i = 1, 2, 3. Here, ϵ_0 is the vacuum permittivity and $\chi^{(n)}$ is the n-th order electric susceptibility of the material.

In silica microresonators, the lowest order nonlinearity is the third-order nonlinearity due to the inversion symmetry of silica material. If high power pump laser is coupled into the high-Q microresonators, the intra-cavity field intensity become high enough to see the optical nonlinearity. The third-order $\chi^{(3)}$ nonlinearity (Kerr-nonlinearity) induces optical parametric oscillation (OPO) and four-wave mixing (FWM). OPO process converts two pump photons at ω_p into "signal" photon at ω_s and "idler" photon at ω_I. This OPO process requires energy and momentum conservation, and phase matching of the involved optical fields is critical. On the other hand, four-wave mixing can occur if at least two lasers with different frequencies propagate together in a nonlinear medium. Assuming two input lasers with frequencies ω_1 and ω_2 (with $\omega_2 > \omega_1$), a refractive index modulation at the difference frequency occurs, and creates two new lasers with frequencies $\omega_3 = 2\omega_1 - \omega_2$ and $\omega_4 = 2\omega_2 - \omega_1$.

The generation of optical frequency combs in microresonators, which will be discussed in chapter 2-4, is possible due to these important nonlinear effects: parametric oscillation and four-wave mixing.

1.5.2 Stimulated Brillouin Scattering

Stimulated Brillouin Scattering (SBS) is also a third-order (χ^3) optical nonlinearity that results from the interaction between light and acoustic (mechanical) fields in a dielectric

material due to the coupling by electrostriction [4, 5, 6, 7]. In a quantum mechanical picture, a pump photon having k_p (wave vector) and ω_p (angular frequency) annihilates and creates a down-shifted Stokes photon (k_s, ω_s) and a phonon (β_B, Ω_B). This SBS process requires the conservation of energy and momentum as follows:

$$\omega_p = \omega_s + \Omega_B \tag{1.4}$$

$$k_p = k_s + \beta_B. \tag{1.5}$$

For backward Brillouin scattering, which will be discussed in chapter 6, this gives the Brillouin shift frequency, $\Omega_B/2\pi = 2nV_a/\lambda_p$, where V_a is the sound velocity and λ_p is the pump laser wavelength. Figure 1.7 illustrates the principle of the backward SBS process. When pump laser propagates through the dielectric medium, variation of light intensity creates periodic refractive index change (Bragg grating) via electrostriction. Then, the pump laser sees the Bragg grating and is reflected backward. To satisfy the momentum conservation, the refractive index grating (acoustic phonon) is moving forward.

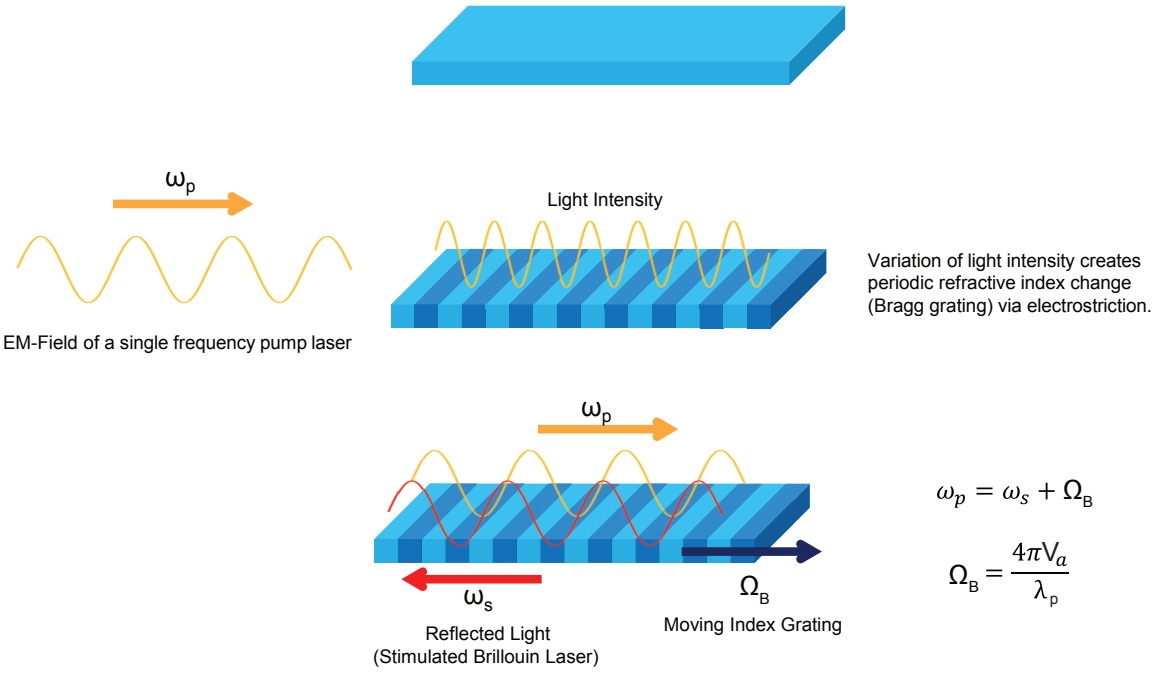

Figure 1.7: **Schematic of backward stimulated Brillouin scattering.**

In optical fiber systems, SBS process has been an important signal impairment mechanism in long-distance optical communication systems [8]. It is also useful and applied to all-fiber lasers [9] and slow-light generation [10]. Recently, the SBS process has attracted considerable interest in micro/nano-scale devices [11]. Brillouin laser action has been demonstrated in various microresonator systems including silica resonators [12, 1, 13, 14] and CaF_2 resonators [15]. Brillouin amplification has also been observed in integrated Chalcogenide waveguides [16], and confinement-enhanced amplification has been realized in silicon waveguides [17]. SBS also provides a powerful tool for integrated photonics signal processing [18, 19, 20].

The SBS process was originally a parametric process. In the case that we will discuss in chapter 6, the acoustic field (phonon) decays much faster than optical field (photon). Under this circumstances, the more strongly damped field (phonon) will be eliminated adiabatically and the less-strongly damped optical field (photon) will be amplified. Thus, the parametric process will look like a stimulated scattering process. However, in certain systems, the phonon damping rate is lower or comparable to the photon damping rate. In these systems, cavity optomechanical effects [21] including optomechanical cooling [22] and optomechanical-induced transparency [23] can be observed.

Chapter 2

Microresonator-based Optical Frequency Comb

Since their demonstration in the late 1990s [24, 25, 26], optical frequency combs have revolutionized a wide range of research areas requiring precision measurements of time and frequency, including optical clocks, precision spectroscopy, precision distance measurement, microwave signal synthesis, and astronomical spectrograph calibration. In this chapter, optical frequency comb technology will be briefly overviewed and the generation of optical frequency combs from microresonators will be introduced. Microresonator soliton, which is the mode-locked frequency comb, and the method to trigger/stabilize the soliton will also be discussed.

2.1 Introduction to Optical Frequency Comb

Optical frequency comb is a very precise tool for measuring different frequencies of light and it is the only technology that can accurately measure optical frequencies. The technology is made possible by recent advances in mode-locked ultrafast lasers that emit femtosecond pulses lasting millionths of a billionth of a second. In a mode-locked laser, peaks of many laser fields at different frequencies coincide at regular time intervals. By the destructive and constructive interference, the laser lights form very short light pulses containing many different frequencies. Figure 2.1(a) illustrates the relationship between frequency comb and mode-locked laser.

The properties of the optical frequency combs rely on the properties of mode-locked

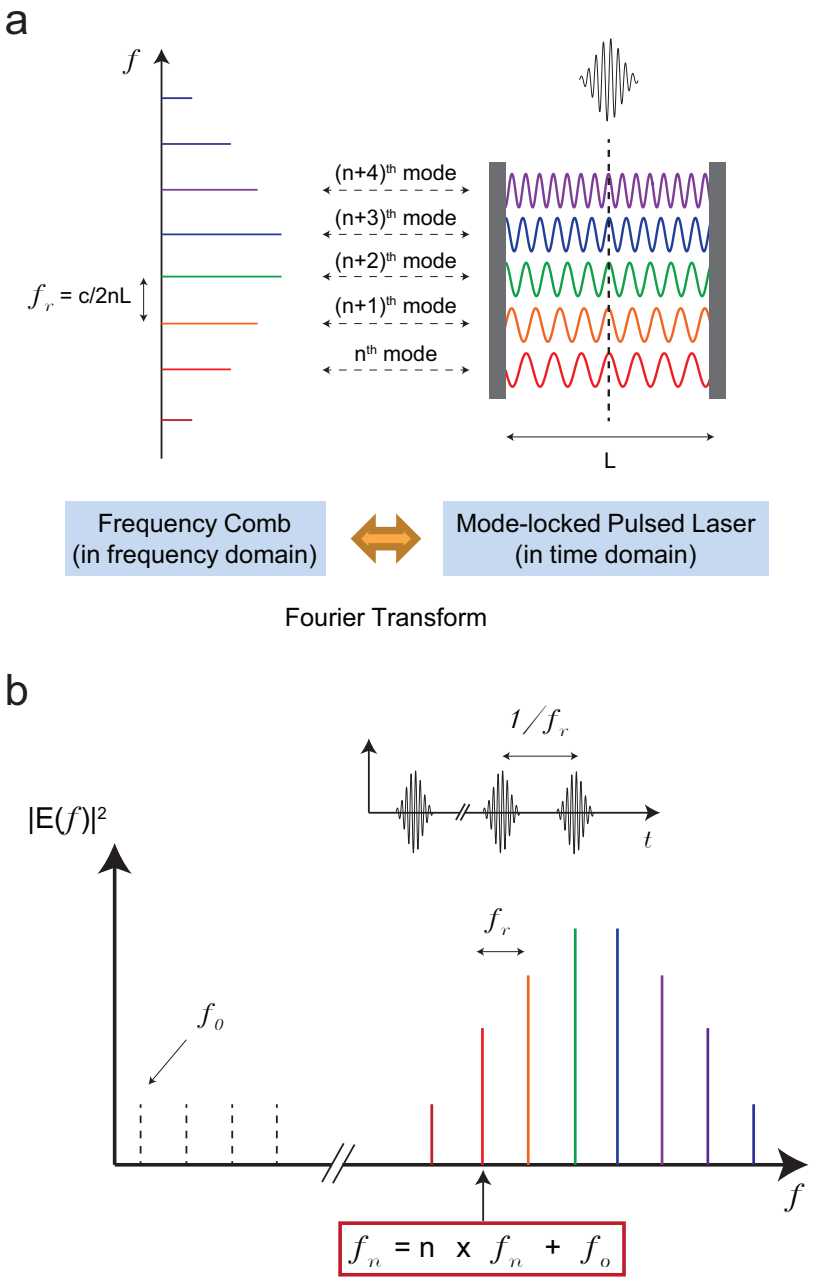

Figure 2.1: **Concept of optical frequency combs.** (a) Schematic diagram showing the relationship between the femtosecond mode-locked laser and the optical frequency comb. (b) Schematic diagram showing a frequency comb as a frequency ruler. The two degrees of freedom (f_r and f_0) determines the property of a frequency comb and these two frequencies must be stabilized for an "absolute" frequency ruler. f_r is the pulse repetition frequency and f_0 is the offset frequency at baseband.

pulse in time domain by the inverse relationship between time and frequency. The pulse width determines the span of the frequency comb, and the timing between pulses determines the spacing between the teeth of the frequency comb. The shorter the laser pulses, the broader the range of frequencies in the comb. The faster the pulse repetition rate, the wider the spacing between the teeth. Frequency comb systems exist across a broad spectral range spanning ultraviolet to infrared, and have very fine, evenly spaced teeth. The teeth can be used like a ruler to measure the light emitted by lasers, atoms, stars with high precision.

The stability of the laser frequency determines the linewidth, or precision, of the each comb teeth. As shown in figure 2.1(b), the optical frequency of n-th comb tooth (f_n) can be expressed as $f_n = n \times f_r + f_0$, where f_r is the pulse repetition frequency and f_0 is the offset frequency at baseband. Typically, these two frequencies are not stable and drifting around. To make optical frequency combs as an absolute frequency ruler, the two frequencies should be detected and stabilized. This process of stabilizing frequency comb is called "self-referencing" and the stabilized comb is called the "self-referenced frequency comb".

Frequency combs are already widely used in metrology and physics research, and there are several commercially available products based on femtosecond lasers, such as Ti:sapphire, Er:fiber, and Yb:fiber mode-locked lasers.

2.2 Generation of Optical Frequency Combs from Microresonators

Although conventional optical frequency comb technology based on fiber lasers is robust and become a commercial technology, it would be advantageous to further reduce the size, cost, and power consumption. In addition, it would be useful in some applications to have repetition frequency above 10 GHz. For this reason, miniature optical frequency combs or microcombs[27, 28] have been demonstrated across a range of emission bands using several dielectric materials[27, 29, 30, 31, 32, 33] as shown in figure 2.2. Some of the material systems are suitable for monolithic integration with other chip-based photonic components[34, 35, 36].

Figure 2.3 illustrates the principle of microcomb generation. Under continuous-wave laser pumping, the laser light coupled into the microresonator builds up the intracavity optical field intensity above the threshold of optical nonlinearity. The combs are initiated by way of parametric oscillation [37, 38] and are broadened by cascaded four-wave mixing[27, 28]. Typically, the generated microcombs are not phase-locked, which means the comb

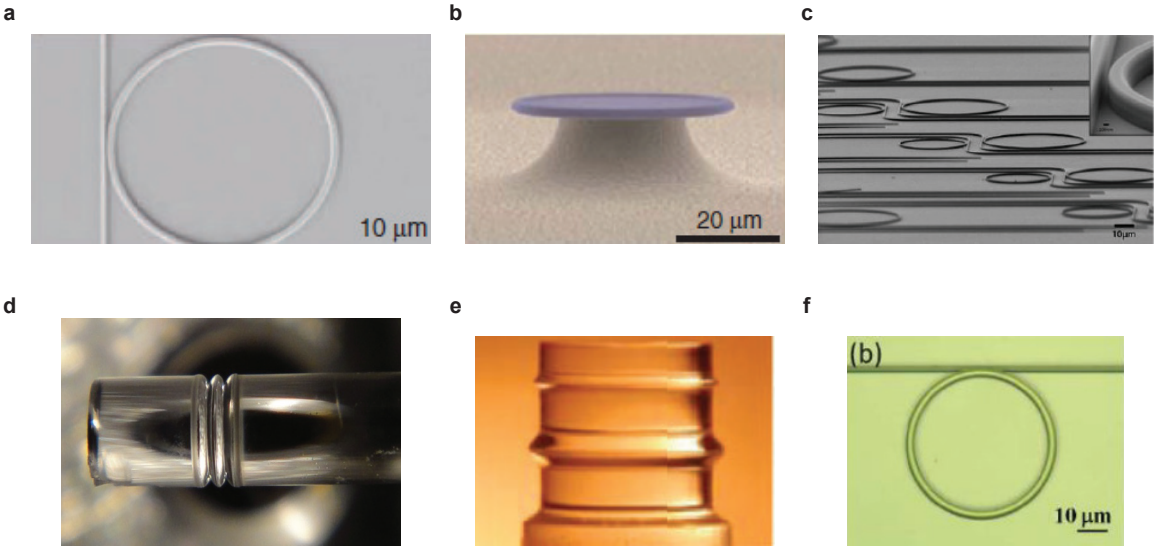

Figure 2.2: **Various material systems generating microcombs.** (a) Silicon nitride ring resonator. (b) Silica microtoroid. (c) Diamond ring resonator. (d) Silica micropillar. (e) Crystalline (MgF_2, CaF_2) microresonator. (f) Aluminum nitride ring resonator.

teeth are not equally-spaced.

The silica wedge disk resonators used in this work have been applied to generate combs with the free spectral range (FSR) ranging from 2.6 GHz to 220 GHz[32]. Phase-locked states are also observed from the devices. Figure 2.4 shows two examples of microcomb optical spectra.

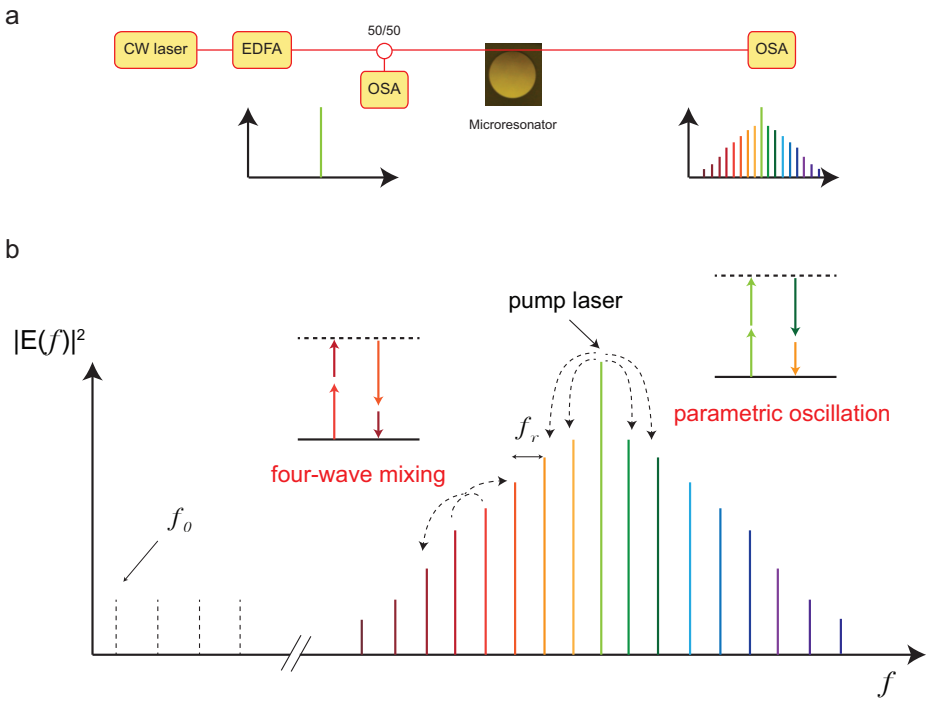

Figure 2.3: **Principle of microcomb generation.** (a) Continuous-wave (CW) laser is amplified using an erbium-doped fiber amplifier (EDFA) and coupled into the microresonator. Inside the microresonator, the intracavity optical field intensity builds up above the threshold of optical nonlinearity, and the micocomb is generated by parametric oscillation and four-wave mixing process. OSA : Optical spectrum analyzer. (b) Schematic diagram showing the parametric oscillation and four-wave mixing processes involved in microcomb generation.

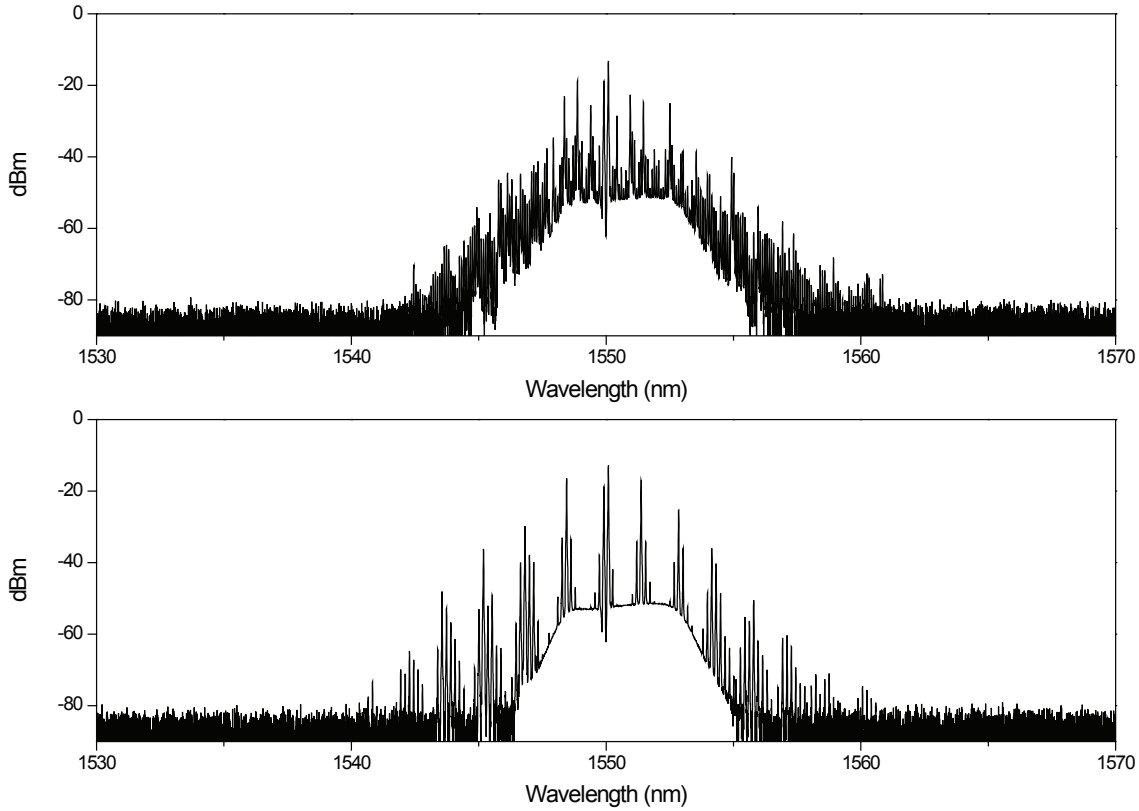

Figure 2.4: **Typical optical spectra of microcomb.** The microresonator is pumped at 1550 nm and generates sidebands via parametric oscillation and cascaded four-wave mixing process. The two optical spectra are obtained by adjusting the pump-resonator detuning frequency.

2.3 Soliton Mode Locking in Microresonators

While phase-locked states and pulse generation have been demonstrated in earlier works on microcombs, microcombs typically were not phase-locked and the noise characteristics were difficult to control. Recently, temporal soliton mode-locking[39, 40, 41, 42, 43], a major advancement in microcomb research, has been realized. Optical solitons are propagating pulses of light that retain their shape, and soliton microcombs are temporal solitons because the pulse shape coming out of the cavity is same at each time period. Soliton microcombs feature dissipative Kerr solitons that leverage the Kerr nonlinearity to both compensate dispersion and to overcome cavity loss by way of parametric gain[39]. Unlike earlier microcombs, this new device provides phase-locked femtosecond pulses with well-defined, repeatable spectral envelopes. Their pulse repetition rate is typically several GHz to THz, and has excellent phase noise characteristics[40]. Different from conventional mode-locked lasers, microresonator-based solitons don't require active gain or saturable absorber. Self-referencing of microcombs has also been demonstrated via external broadening[44, 45] or generation of dispersive wave[41].

2.3.1 Soliton Generation

Solitons form when the pump frequency is red detuned relative to an optical mode, and shows quantized power steps in the pump power transmission versus frequency tuning. To generate soliton microcombs, the mode family must feature anomalous dispersion[37] and the dispersion is minimally distorted by other resonator modes. Typically, the excitation of soliton pulse trains is complicated by the thermal nonlinearity of the resonator. To reduce thermal nonlinearity originated from wet oxidation process and surface adsorption of H_2O, the silica wedge disk resonators are annealed at 1000 degree C for several hours.

In the measured silica resonators in this work, typical threshold power for microcomb generation is several mW. This value is consistent with the theoretical formula of the threshold of parametric oscillation,

$$P_{th} = \frac{\pi n \omega_0 A_{eff}}{4\eta n_2} \frac{1}{D_1 Q^2}, \tag{2.1}$$

where n is the refractive index, ω_0 is the optical frequency of pump laser, A_{eff} is the effective mode area, D_1 is the cavity FSR, and $\eta = Q/Q_{ext}$ is the cavity loading factor where Q_{ext} and Q are external and total Q-factor, respectively.

The soliton power and pulse width are also given by the following formula [39, 46, 47]:

$$P_{sol} = \frac{2\eta A_{eff}}{n_2 Q}\sqrt{-2nc\beta_2\delta\omega}, \tag{2.2}$$

$$\tau = \sqrt{-\frac{c\beta_2}{2n\delta\omega}}, \tag{2.3}$$

where $\beta_2 = -nD_2/cD_1^2$ is the group velocity dispersion and $\delta\omega = \delta\omega_0\delta\omega_p$ is the pump-resonator detuning. Here, $\delta\omega_0$ is the resonator frequency and $\delta\omega_p$ is pump frequency. From the equation 2.2, it is obvious that soliton power depends on the pump-resonator detuning frequency. Throughout this thesis, soliton microcombs are servo-locked to the soliton-

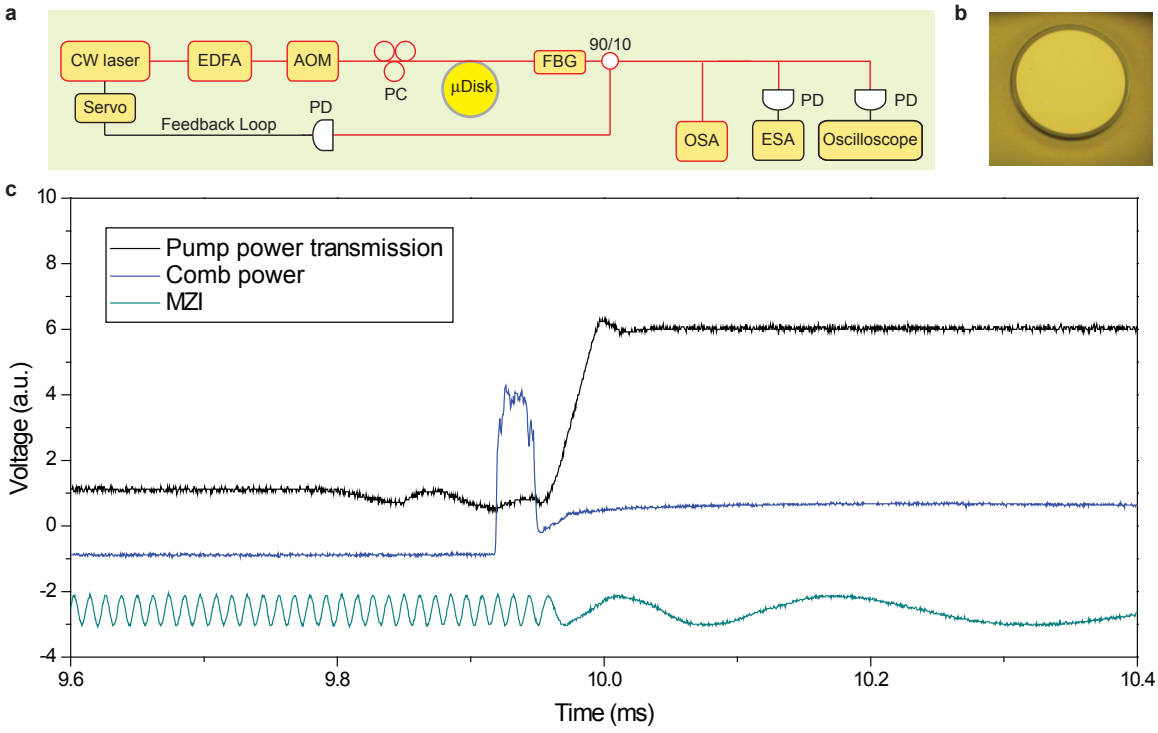

Figure 2.5: **Soliton generation setup.** (a) Typical soliton generation setup using power-kick method. (b) Top view of typical silica wedge disk microresonator. (c) Typical oscilloscope trace monitored for soliton generation.

existing detuning frequency by using the soliton power change around a fixed set point as the discriminator of pump-resonator detuning frequency[40, 48].

Figure 2.5(a) shows typical soliton generation setup. Here, the frequency of the pump laser is tuned towards the resonance from the lower frequencies at a speed of approximately $\sim$ 1 GHz/ms. The pump frequency tuning is stopped before reaching the resonance and the pump power is modulated using an AOM to induce a power kick, which deterministically generates soliton steps[40]. A feedback loop is then turned on to selectively lock to specific soliton numbers according to their comb power levels. The linewidth of the pump lasers is $\sim$2 kHz and the pump power used for a soliton generation is in the range between 100 $\sim$ 500 mW. The generated solitons are stable indefinitely until the system was turned off by the operators. Figure 2.5(b) shows the top view of silica wedge disk microresonator used for soliton generation. Devices having diameters of 3 mm, 4.5 mm, 6 mm, and 7 mm are used in this work. Typical oscilloscope trace monitored during the soliton generation procedure is also shown in figure 2.5(c).

If an optical mode has a high enough quality factor and less thermal broadening, the soliton step becomes longer and controllable soliton mode locking is possible via direct frequency tuning. Compared to the power-kick method, controllable soliton generation using direct frequency tuning method is typically harder to achieve. However, it requires less components and remove the optical power loss at AOM. For this reason, direct frequency tuning method is more desirable, especially for portable microcomb systems.

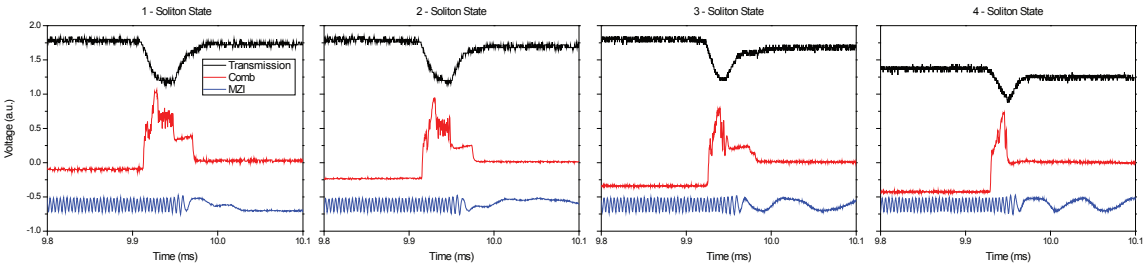

Figure 2.6: Oscilloscope traces showing controllable soliton mode locking via direct laser frequency tuning: (From left to right) single, two, three, and four soliton states. At each figure, transmitted pump power (black), comb power (red), and MZI signal (blue) are shown.

Figure 2.6 shows the oscilloscope traces of four different cases, from single-soliton to four-soliton state, which are generated using direct frequency tuning method. By offsetting the comb power level of single-soliton step to zero using servo box, single soliton state is captured. Capturing two-, three-, and four-soliton state is also possible by increasing the offset level by 2, 3, and 4 times. The optical spectra of four different soliton states are shown in figure 2.7(a-d)

It is worth noting that the maximum comb tooth power at the center of spectral envelop is determined purely by the resonator properties. This can be easily shown by eliminating $\delta\omega$ in eq. 2.2 and eq. 2.3.

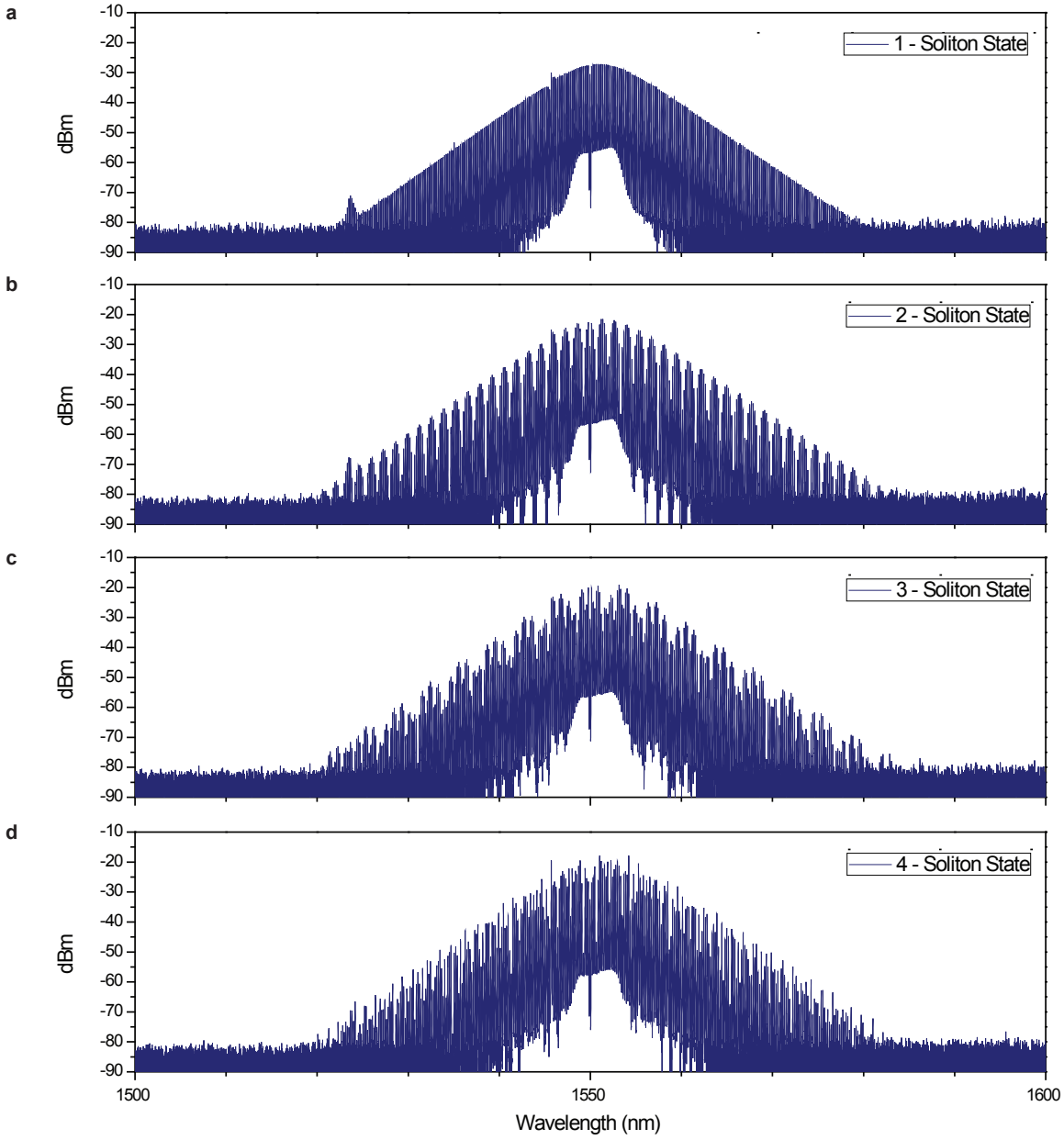

Figure 2.7: **Optical spectra of four different soliton states.** (a) 1-soliton state, (b) 2-soliton state, (c) 3-soliton state, (d) 4-soliton state.

2.3.2 Breather-to-Soliton Transition

Microresonator can exhibit numerous localized intracavity patterns and provide rich insights into nonlinear dynamics. Breather soliton, which represents pulses with oscillating amplitude and duration, is a particular solution of such nonlinear systems. It is also known to exhibit Fermi-Pasta-Ulam (FPU) recurrence, a paradoxical evolution of nonlinearly coupled oscillators that periodically returns to the initial state. Study of breather solitons will help to understand many nonlinear systems and it gives more information about the different operating regimes and evolution of soliton microcombs.

Breathing solitons were first demonstrated in fiber cavities [49], and have been widely predicted in microresonators. Observations of the breather soliton in SiN and MgF_2 microresonators are also reported[50, 51, 52]. Here, we observe and study the breather soliton in our silica wedge disk device. This helps to understand how dissipative Kerr solitons are generated from chaotic noisy comb states.

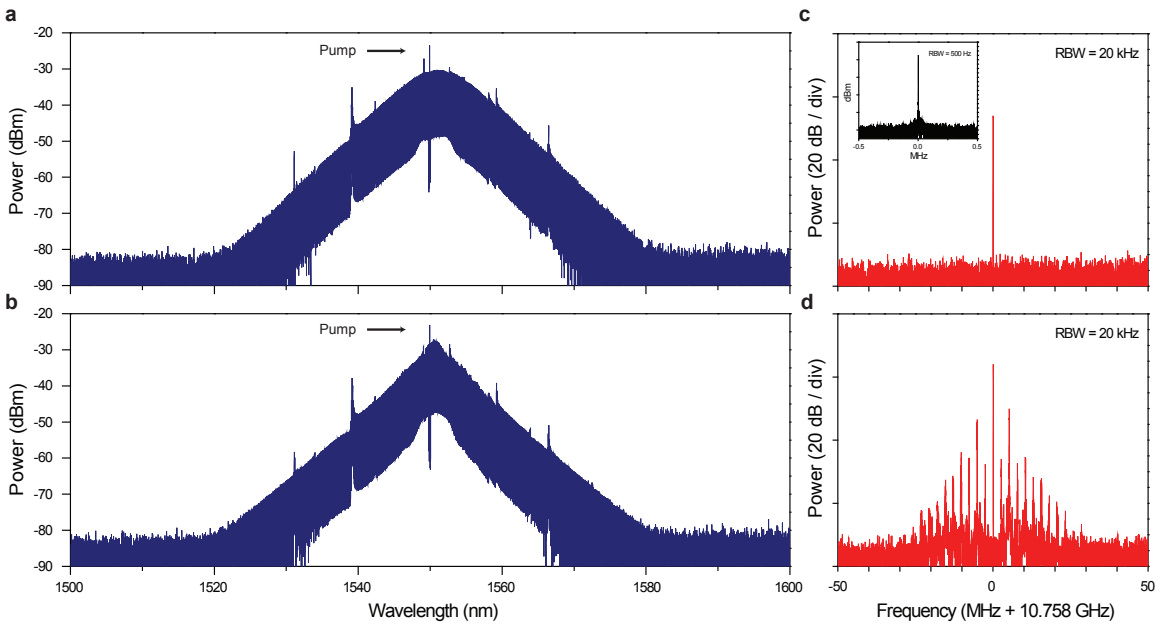

Figure 2.8: **Generation of soliton and breather soliton.** Optical spectra of (a) soliton and (b) breather soliton having 10.7 GHz repetition frequency. Electrical spectra of (c) soliton and (d) breather soliton showing the repetition frequency and breathing frequency. Measurement is performed over 100 MHz span with the resolution bandwith(RBW) of 20 kHz.

To generated breather solitons, the same experimental setup shown in figure 2.5(a) is used. First, single soliton state is generated and deterministic transition into breather soliton state is achieved by reducing the soliton power set point of the servo loop. Lower soliton power indicates blue detuning of pump laser frequency, which can be seen in figure 2.5(c). Typical optical spectra of single-soliton state and breather soliton state are shown in figure 2.8(a) and (b), respectively. Attenuated pump laser peak is shown near 1550 nm and mode-crossing-induced spurs are also shown in the spectra. The electrical spectrum of breather soliton in figure 2.8(d) shows many sidebands near the repetition frequency. In comparison, the electrical spectrum of single soliton in figure 2.8(c) does not have such sidebands.

Figure 2.9 shows the electrical spectra of the repetition frequencies at four different pump frequency detunings from larger frequency (blue detuning) to smaller frequency (red

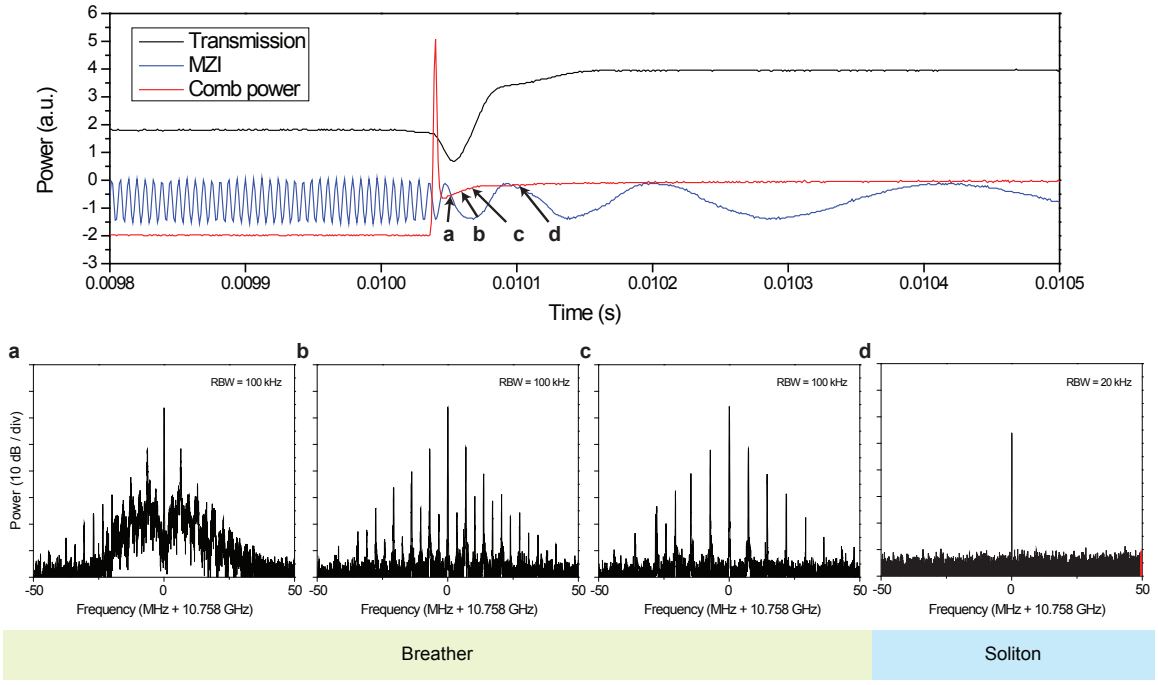

Figure 2.9: **Transition from breather soliton to soliton.** Upper panel shows the oscilloscope trace monitored during the measurement. The pump laser transmission power (black), comb power (red), and Mach-Zehnder interferometer(MZI) signal (blue) are shown. The period of MZI is 3.225 MHz. (a-d) Electrical spectra near the repetition frequency of 10.7 GHz at different pump detuning frequencies. As the pump frequency is detuned from blue to red, the comb state evolves in the order of chaotic state, sub-harmonic breather, breather, and soliton.

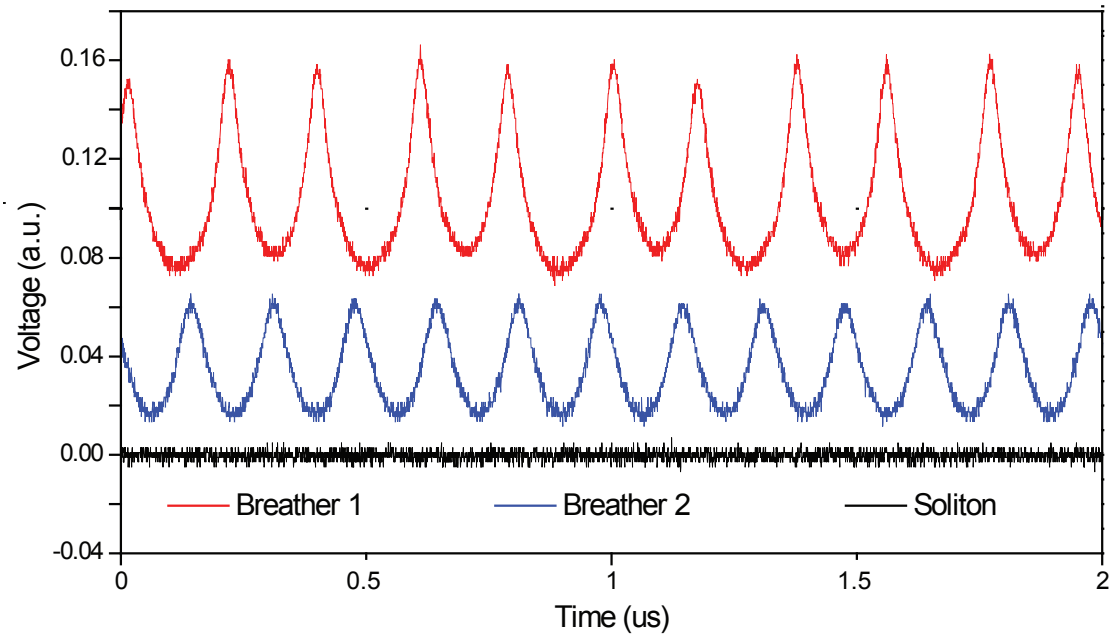

Figure 2.10: **Breathing frequencies.** Comb powers in three different states are recorded using an oscilloscope.

detuning). Mach-Zehnder interferometer (MZI) signal (blue trace in the upper panel) is an indicator of the pump laser frequency. The electrical spectra in figure 2.9 (a-d) show that the single soliton state (figure 2.9(d)) evolves from chaotic state ((figure 2.9(a)), subharmonic breather soliton state (figure 2.9(b)) and breather soliton state (figure 2.9(c)).

Figure 2.10 shows the oscilloscope time traces of photodetected comb powers at three different pump detunings. When the pump frequency is detuned from blue to red (Breather 1 state to Breather 2 state), the breathing frequency is increasing and eventually there's no breathing (soliton state). This corresponds to the electrical spectra data shown in figure 2.9. It's interesting to note that, in some cases, further red-detuning of the pump laser frequency results in a new soliton at longer wavelength (Figure 2.11). The new soliton is generated by Stokes Raman scattering of the original soliton near 1550 nm, and is called "Stokes soliton". The generation of Stokes soliton and its application will be discussed in detail in chapter 3.

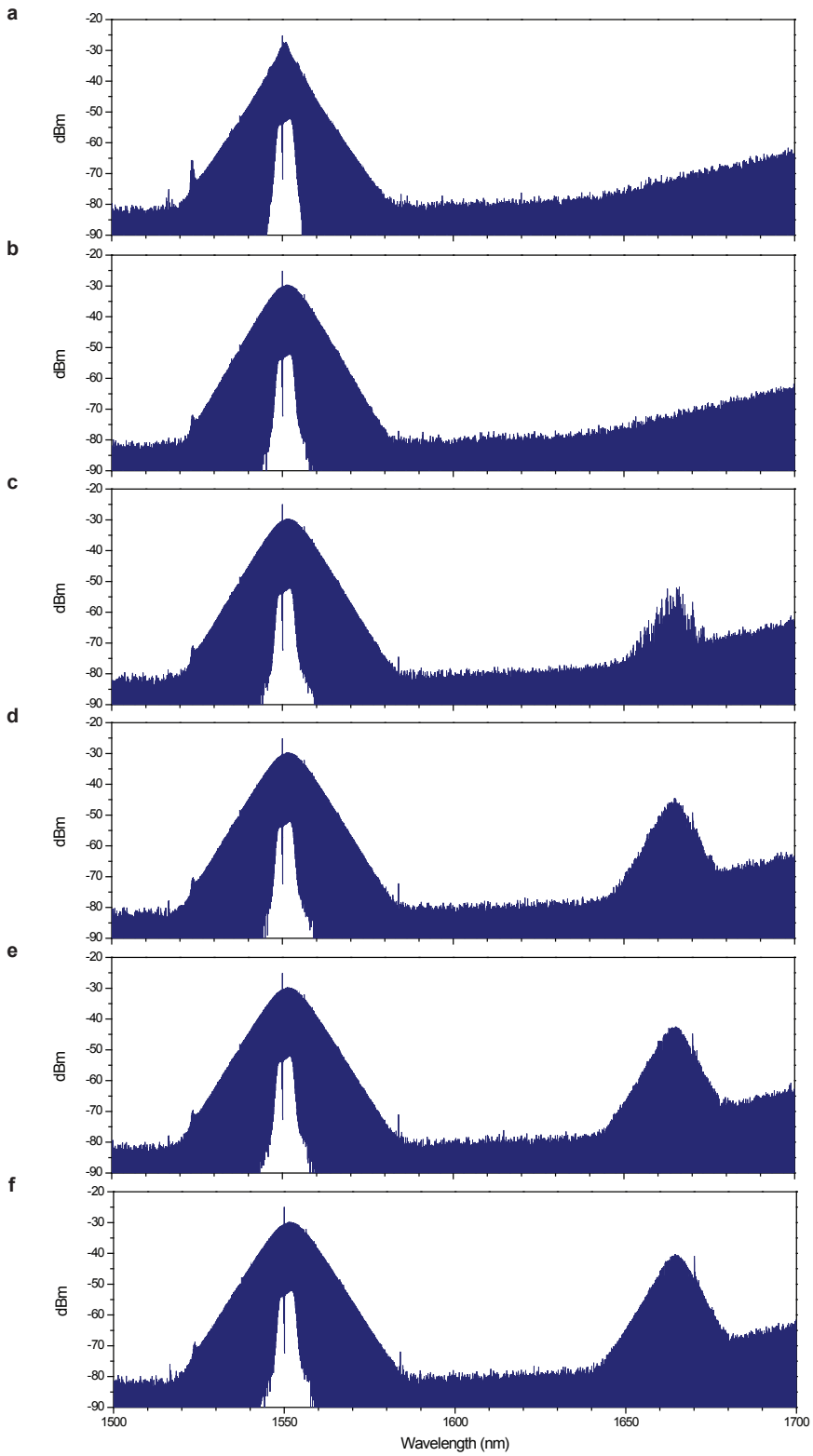

Figure 2.11: **Transition from breather to Stokes soliton.** By adjusting the pump detuning from larger frequency to smaller frequencies, continuous transition from (a) breather state to (b) soliton state and (c-f) Stokes soliton generation state is observed.

Chapter 3

Microresonator Soliton Dual-Comb Spectroscopy

Rapid characterization of optical and vibrational spectra with high resolution is important in many spectroscopic applications. In this regard, dual-comb spectroscopy has emerged as a powerful approach to acquire nearly instantaneous Raman and optical spectra with unprecedented resolution. The dual-comb spectroscopy method enables the direct acquisition of material information from the electrical spectra instead of using bulky mechanical spectrometers. Soliton microcombs, which are introduced in the previous chapter, can potentially transfer the dual-comb method to a chip platform. These soliton microcombs feature high-coherence (pulsed mode locking) and broad, reproducible spectral envelopes, which is essential for dual-comb spectroscopy. In this chapter, dual-comb spectroscopy is demonstrated using the dual-soliton source generated from microresonators. Improvements in the performance parameters of this chip-based dual-soliton source, such as spectral resolution, signal-to-noise ratio, and spectral coverage, are also discussed. Our work shows the potential for integrated dual-comb source on a chip, which can provide a new solution for the next generation spectroscopy system featuring compact size, high signal-to-noise, and fast acquisition rate.

3.1 Introduction

Since their demonstration in the late 1990s [24, 25, 26], optical frequency combs have revolutionized precision measurements of time and frequency and enabled new technologies such as optical clocks[26]. One remarkable method they make possible is dual-comb spectroscopy, which leverages the coherence properties of combs for rapid, broad-band spectral analysis with high accuracy[53, 54, 55, 56, 57, 58, 59]. Frequency comb systems exist across a broad spectral range spanning ultraviolet to infrared, making this method well suited for spectroscopic analysis of diverse molecular species[59].

As introduced in chapter 2, miniature optical frequency combs or microcombs[27, 28] have been demonstrated for the widespread use of comb-based technologies. Not only are the microcombs genenerated from microresonators via parametric oscillation [37, 38] and cascaded four-wave mixing[27, 28], but frequency modulation (FM) combs [60] are also demonstrated via four-wave mixing in the ultra-fast intraband gain medium of quantum cascade lasers (QCL). These FM systems generated frequency combs in mid infrared and have been applied to demonstrate dual-comb spectroscopy [61]. Heterodyne of two microresonator-based microcombs in the mid infrared has also been demonstrated for dual-comb spectroscopy[62]. However, these microcombs are typically not phase-locked and the spectral envelop is not reproducible. On the other hand, soliton microcombs, which provide phase-locked femtosecond pulses, can offer well-defined, repeatable spectral envelopes. They also provide excellent phase noise characteristics[40].The low-noise and reproducible characteristics are important for reliable dual-comb spectroscopy.

In this chapter, we demonstrate dual-comb spectroscopy using the soliton microcombs. A schematic view of the microresonator soliton dual-comb spectroscopy is shown in Fig. 3.1. It shows two soliton pulse trains having different repetition rates ($\Delta f_r = f_{r1} - f_{r2}$) are generated from distinct microresonators and then combined using a directional coupler. One of the combined streams is coupled through a test sample (a gas cell of molecules whose absorption spectrum is to be measured) and photodetected to provide a ”signal”. The other combined stream is directly photodetected to provide a ”reference”. The slight difference in repetition rates of the soliton pulse streams creates a periodically time-varying

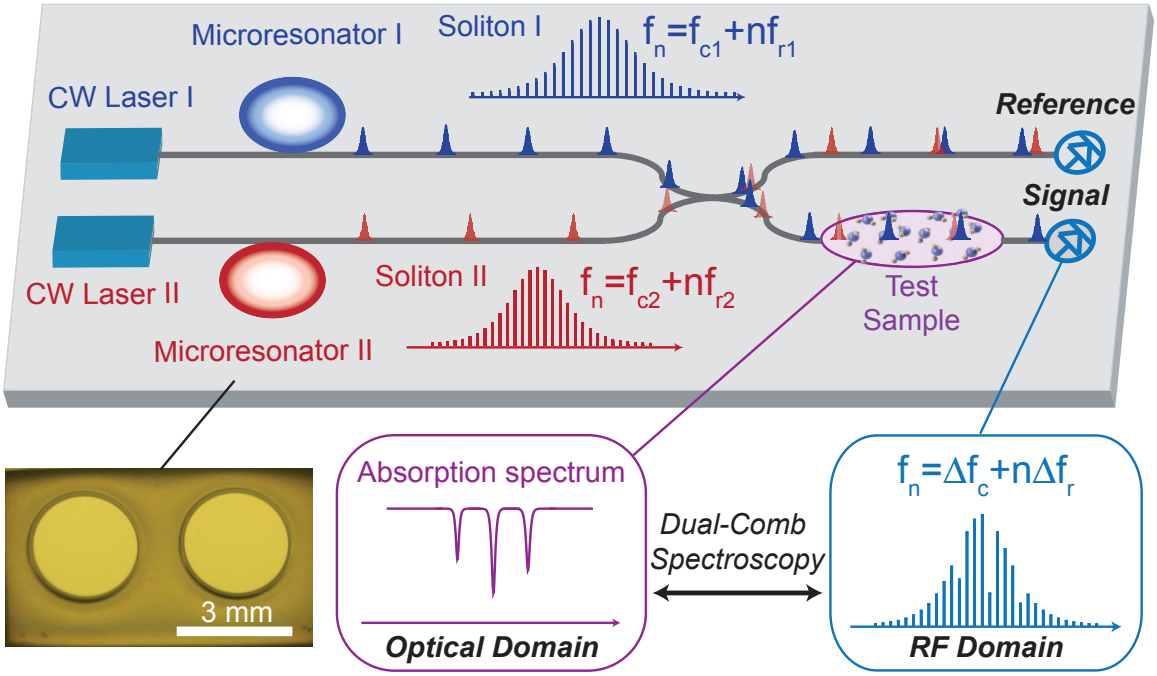

Figure 3.1: **Microresonator-based dual-comb spectroscopy**. Two soliton pulse trains with slightly different repetition rates are generated by continuous optical pumping of two microresonators. The pulse trains are combined in a fiber bidirectional coupler to produce a signal output path that passes through a test sample as well as a reference output path. The output of each path is detected to generate an electrical interferogram of the two soliton pulse trains. The interferogram is Fourier transformed to produce comb-like electrical spectra having spectral lines spaced by the repetition rate difference of the soliton pulse trains. The absorption features of the test sample can be extracted from this spectrum by normalizing the signal spectrum by the reference spectrum. Also shown is the image of two silica disk resonators. The disks have a 3 mm diameter and are fabricated on a silicon chip.

interferogram in the detected photocurrent with a period $1/\Delta f_r$. Fourier transform of this time-varying intergerogram reveals the optical spectra of interfering soliton microcombs, now shifted to radio-frequency domain. The signal spectrum containing the molecular absorption information is then normalized using the reference spectrum to obtain the spectral absorption of the test sample.

3.2 Microresonator-based Dual-Soliton Source and $H^{13}CN$ Detection

3.2.1 Microresonator-based Dual-Soliton Generation

Details on experimental setup for microresonator dual-soliton generation is shown in Fig. 3.2. Starting from two fiber lasers (Orbits Lightwave) at 1549.736 nm and 1549.916 nm (the difference frequency of the pumps was determined to be 22.5 GHz by detecting their electrical beat note and measurement on a spectrum analyzer), the pump lasers are amplified by erbium-doped fiber amplifier and coupled to an acousto-optic frequency modulators (AOM). Each frequency-shifted output of the AOM is used to provide a controllable optical pumping power that is required for soliton triggering[48]. The pump light is evanescently coupled into the silica microresonator via a tapered fiber[2, 3]. Using a fiber Bragg grating (FBG) filter, residual pump power that is transmitted past each resonator is attenuated and a 90/10 tap is used to monitor the soliton power for feedback control of the pump laser frequency so as to stabilize the triggered soliton indefinitely [48]. The optical spectra of the individual soliton pulse streams were monitored using a Yokogawa optical spectrum analyzer. Additional precision calibration of the spectra was performed using a Wavelength References Clarity laser locked to a molecular absorption line.

Typical soliton optical spectra are presented in figure 3.3(a-b), and feature the characteristic sech^2 envelope observed over a 60 nm wavelength span. The detected electrical spectrum for each soliton source was measured using a spectrum analyzer with a bandwidth of 26 GHz (Figure 3.3(c-d)). The narrow spectral lines have a signal-to-noise greater than 75 dB, showing that corresponding repetition rates are extremely stable. Resolution

bandwidth (RBW) of 500 Hz is used for the measurement. The high-Q resonators used in this work are silica whispering-gallery devices fabricated on a silicon wafer using a combination of lithography and wet/dry etching[1]. The unloaded quality factor of the microresonators is approximately 300 million, and the solitons have repetition rates of approximately 22 GHz that were determined primarily by the diameter of the devices (3 mm). The soliton pulse streams are detected by u2t photodetectors with the detection bandwidths of 50 GHz. Then, the interferograms are recorded on an oscilloscope and the repetition rates of the soliton pulse streams are also monitored by an electrical spectrum analyzer (ESA).

Using a 50/50 bidirectional coupler, the two stabilized soliton pulse streams are combined and coupled into two paths (Figure 3.1 and figure 3.2). One path contained a $H^{13}CN$ gas cell which functions as the test sample. The $H^{13}CN$ gas cell (manufactured by Wavelength References, Inc.) is 16.5 cm long and pressurized to 300 Tor. The estimated

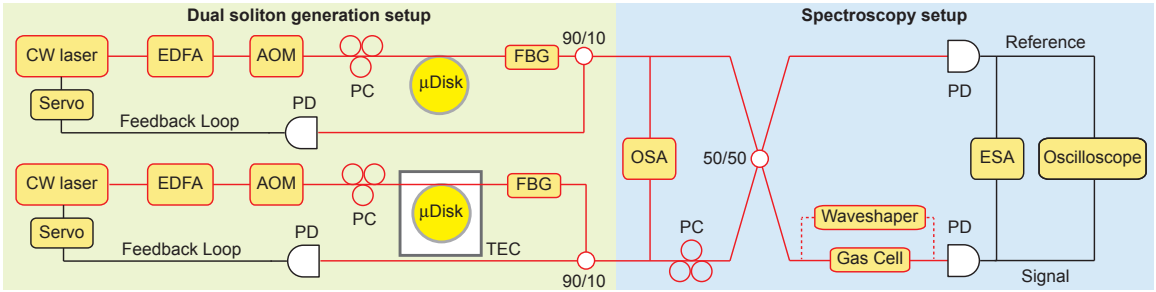

Figure 3.2: **Detailed experimental setup**. Continuous-wave (CW) fiber lasers are amplified by erbium-doped fiber amplifiers (EDFA) and coupled into high-Q silica wedge microresonators via tapered fiber couplers. An acousto-optic modulator (AOM) is used to control pump power to trigger soliton generation in the microresonators. Polarization controllers (PC) are used to optimize resonator coupling. A fiber Bragg grating (FBG) removes the transmitted pump power in the soliton microcomb. The pump laser frequency is servo controlled to maintain a fixed detuning from the microcavity resonance by holding the soliton average power to a fixed setpoint. An optical spectrum analyzer (OSA) monitors the spectral output from the microresonators. The two soliton pulse streams are combined in a bidirectional coupler and sent to a gas cell (or a WaveShaper) and a reference path. The interferograms of the combined soliton pulse streams are generated by photodetection (PD) and recorded on an oscilloscope. The repetition rates of the soliton pulse streams are also monitored by an electrical spectrum analyzer (ESA). The temperature of one resonator is controlled by a thermoelectric cooler (TEC) to tune the optical frequency difference of the two solitons.

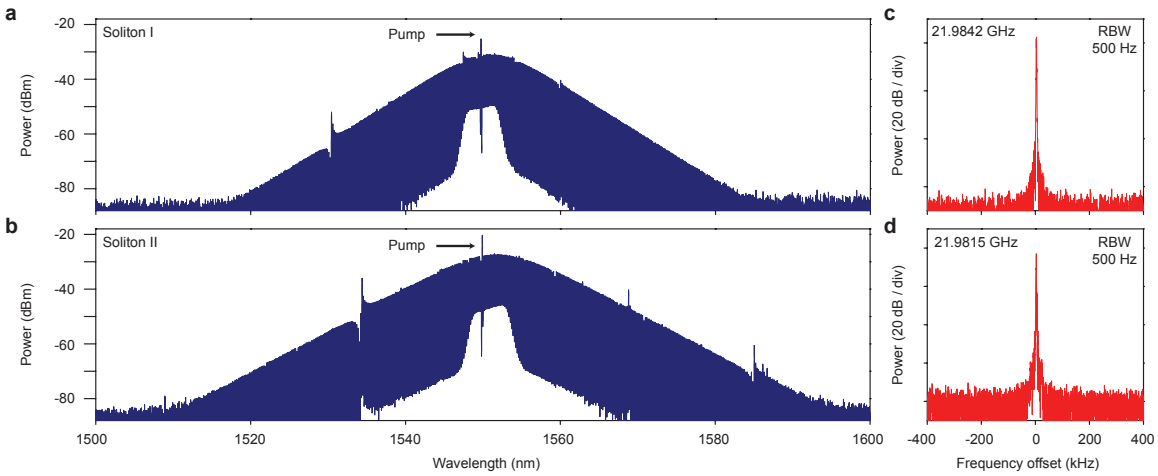

Figure 3.3: **Soliton comb spectral charaterization**. (**a** and **b**) Optical spectra of the microresonator soliton pulse streams. (**c** and **d**) Electrical spectra showing the repetition rates of the soliton pulse streams. The rates are given in the legends.

linewidth of the $H^{13}CN$ spectral features is 200 pm or approximately 25 GHz at 1550 nm. The other path is coupled directly to a photodetector and functions as the reference. The test sample path also includes an alternate path in which a WaveShaper is inserted. Using a thermoelectric cooler, the temperature of one microresonator is controlled to tune the relative optical frequency difference of the two solitons streams. In the measurements this difference was held below 1 GHz, allowing the observation of the interferogram on an 1 GHz-bandwidth oscilloscope. The soliton pulse streams are also detected by u2t photodetectors with the detection bandwidths of 50 GHz, and the repetition rates of the soliton pulse streams ($\sim$ 22 GHz) are also monitored by an electrical spectrum analyzer (ESA).

3.2.2 Interferogram and Initial Spectroscopic Test

The reference interferogram is shown in figure 3.4(a). It has a period of 386 ns, corresponding to a soliton repetition rate difference of 2.6 MHz. This relatively small repetition rate difference was possible by precise control of the resonator diameter using calibrated wet etching of the silica[1]. Figure 3.4(b) shows the calculated Fourier transform of the reference interferogram. The small repetition rate difference on the much larger 22 GHz

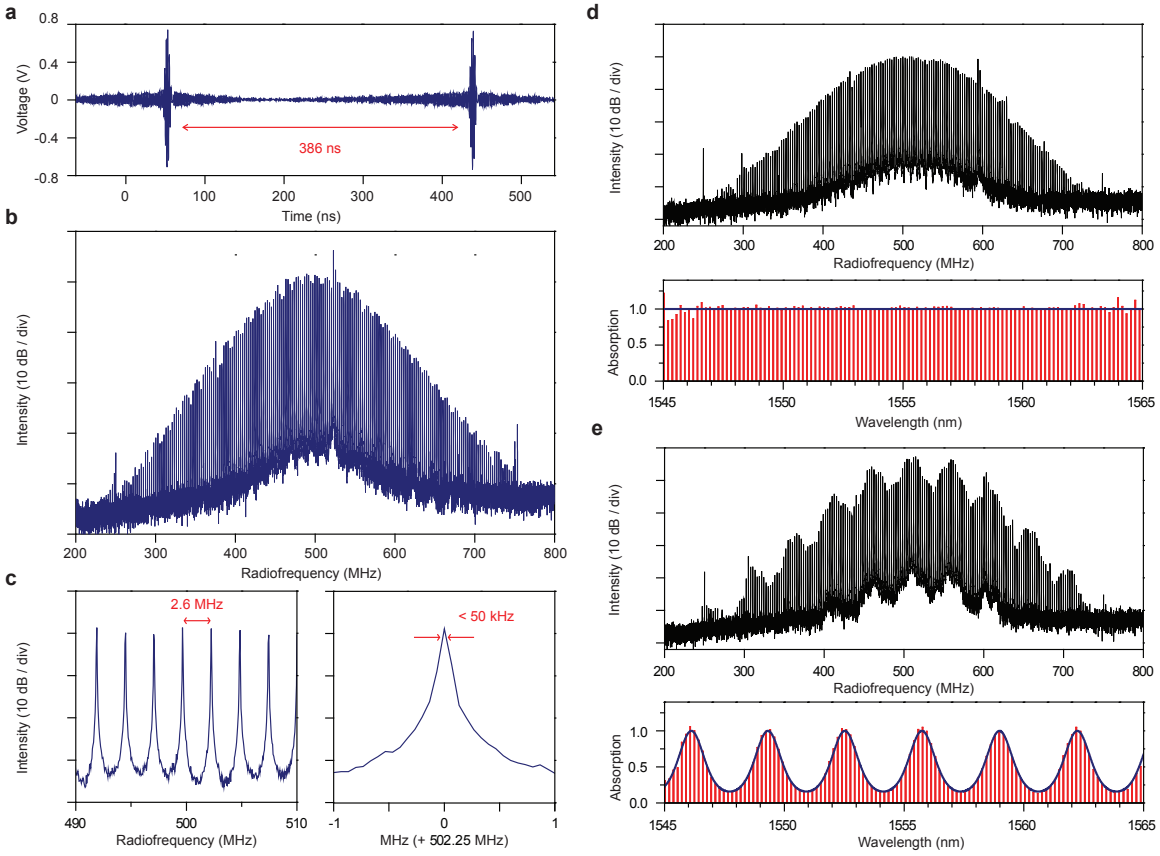

Figure 3.4: **Measured electrical interferogram and spectra.** (**a**) The detected interferogram of the reference soliton pulse train. (**b**) Typical electrical spectrum obtained by Fourier transform of the temporal interferogram in (a). To obtain the displayed spectra, ten spectra each are recorded over a time of 20 μs and averaged. (**c**) Resolved (multiple and individual) comb lines of the spectrum in B are equidistantly separated by 2.6 MHz, the difference in the soliton repetition rate of the two microresonators. The linewidth of each comb line is $<$ 50 kHz and set by the mutual coherence of the pumping lasers. (**d** and **e**) Fourier-transform (black) of the signal interferogram produced by coupling the dual-soliton pulse trains through the synthetic absorber (WaveShaper) with programmed absorption functions (spectrally flat and sine-wave). The obtained dual-comb absorption spectra (red) are compared with the programmed functions (blue curves) from 1545 nm to 1565 nm.

soliton repetition rate makes it possible to compress an optical span of 4 THz (1535 nm to 1567 nm) into 500 MHz of electrical spectrum. The measured wavelength span in the electrical spectrum is limited by the photodetector noise and narrower than the wavelength span of the original soliton pulse streams in optical spectra. The electrical spectrum has a signal-to-noise ratio (SNR) around 30 dB near the central lines. A zoom-in of the spectrum (multi- and single-line) is provided in figure 3.4(c). The electrical comb lines are equidistantly separated by 2.6 MHz and have a full-width-half-maximum linewidth less than 50 kHz, which is limited by the mutual coherence of the two independent pump lasers. The pump laser line in a dissipative Kerr soliton is also a comb tooth in the soliton optical spectrum. As a result, the frequency jitter in each pump is transferred as an overall shift on the resulting soliton comb. Externally locking the two combs should reduce the observed linewidth in the electrical spectrum.

In figure 3.4(b), it is interesting to note that the pump lines are placed toward the high frequency side (near 550 MHz) of the spectral maximum in the interferogram spectrum. In the optical spectra (figure 3.3(a-b)) the pump is blue detuned relative to the soliton spectral maximum (this occurs due to the Raman self-frequency-shift of the soliton[40]). This spectral marker shows that high optical frequencies of soliton combs are mapped to high rf frequencies. Avoided-mode-crossing induced Fano-like spurs[40] in the soliton optical spectra (figure 3.3(a-b)) occurring near 1535 nm are also mapped into a corresponding feature near 750 MHz in the electrical spectrum shown in figure 3.4(b).

As an initial test of the dual-comb source, synthetic absorption spectra were programmed in Finisar WaveShaper 1000S and then measured as dual-comb spectra. The WaveShaper required an erbium fiber amplifier to compensate its insertion loss. Fourier-transforms of the signal interferograms produced using the synthetic absorber are shown in figure 3.4(d-e). The two programmed functions are a spectrally flat 3 dB absorption and a sine-wave absorption having a 4 dB amplitude. The synthetic absorption spectra, obtained by normalizing the signal and reference electrical spectra, are compared with the programmed functions in figure 3.4(d-e). The ability to reconstruct these synthetic spectral profiles clearly demonstrates the reproducibility of solitonic spectral profile.

3.2.3 Detection of $H^{13}CN$ $2\nu_3$ Absorption Band

Using the microresonator soliton dual-comb source, the absorption spectrum of the $H^{13}CN$ $2\nu_3$ band is measured. In figure 3.5(a), the measured dual-comb absorption spectrum from 1538 nm to 1562 nm is shown in red and compared with a directly measured absorption spectrum shown in blue. Both absorption spectra are normalized.

The upper panel in figure 3.5(a) shows the directly measured $H^{13}CN$ absorption spectrum, which is obtained by coupling an external cavity diode laser (ECDL) into the $H^{13}CN$ gas cell and scanning the laser while monitoring the transmitted optical power. A separate signal is also tapped from the ECDL to function as a reference. The relative wavelength change of the ECDL during the scan is calibrated using a fiber Mach-Zehnder interferometer (MZI) and absolute wavelength calibration was possible using a reference laser (Wavelength References Clarity laser). The signal passing through the gas cell and the reference transmissions are recorded at the same time, and the absorption spectrum in figure 3.5(a) is obtained by dividing the signal transmission by the reference transmission.

The dual-comb spectrum (middle panel in figure 3.5(a)) is choppy because of the relatively coarse spectral resolution of the solitons in comparison to the spectral scale of the $H^{13}CN$ absorption lines. Nonetheless, the characteristic envelope of the $H^{13}CN$ $2\nu_3$ band is clearly resolved. In the bottom panel of 3.5(a), the residual difference between the two absorption spectra is shown in green and the calculated standard deviation is 0.0254. Furthermore, a line-by-line overlay of the measured optical and dual-comb spectra in figure 3.5(b) confirms the wavelength precision and absorption intensity accuracy of the dual-comb source.

In conclusion, two soliton microcombs having microwave repetition rates ($\sim$ 22 GHz) were used as a dual-comb source to measure the absorption spectrum of the $2\nu_3$ band of $H^{13}CN$. Simple micro-fabrication using hydrofluoric acid wet etching enabled precision control of the repetition rates so that multi-THz optical spectrum was compressed onto the electrical spectrum less than 1 GHz span. The repetition rate of this soliton comb can be further reduced for improved spectral sampling, which will be discussed in the next section. The dual-comb source has a high SNR and spans over 30 nm in optical C-band.

External broadening using highly nonlinear fiber(HNLF) or generating dispersive wave in the resonator[41], it is possible to extend this spectral span to an octave. Engineering the dispersion of microresonator [63] can also extend the comb bandwidth. Within the transmission window of silica, it is also possible to generate solitons at new pump wavelengths. More generally, a wide range of materials are available to generate microcombs at different wavelengths. Potentially, the dual-soliton source can be applied to realize chip-based dual-comb coherent anti-Stokes Raman spectroscopy (CARS). Integration with other on-chip devices will make soliton-based microcombs well suited for possible realization of a dual-comb spectroscopic system-on-a-chip.

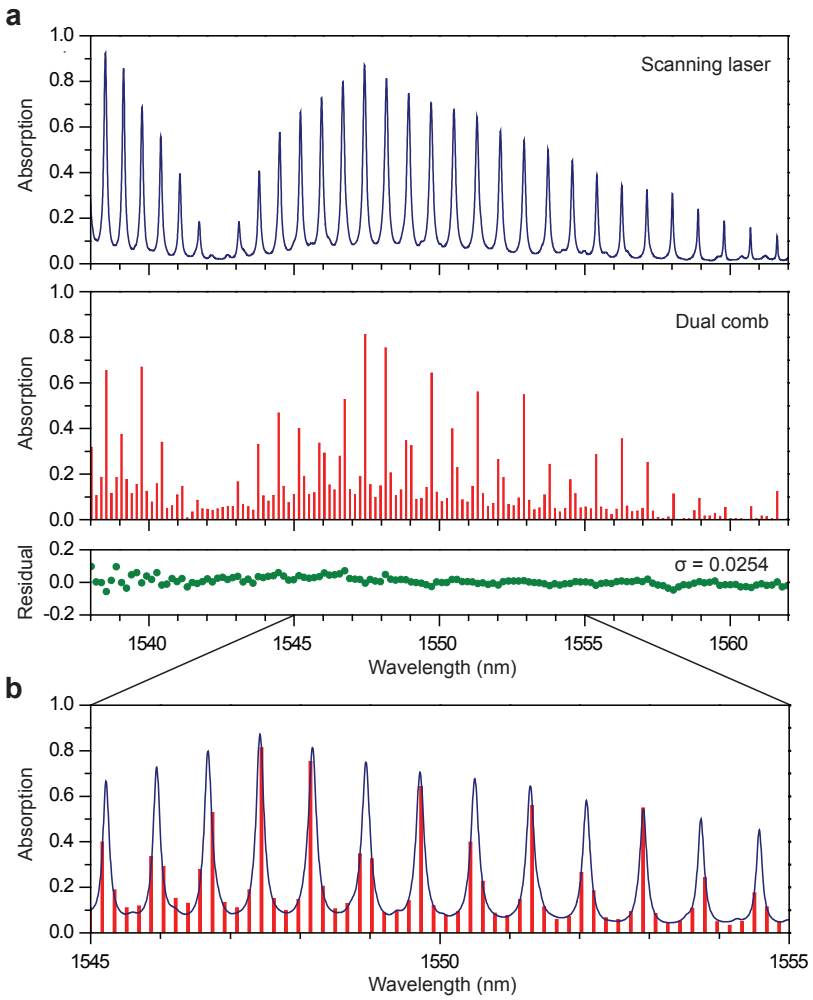

Figure 3.5: **Measured molecular absorption spectra.** (**a**) Absorption spectrum of $2\nu_3$ band of $H^{13}CN$ measured by direct power transmission using a wavelength-calibrated scanning laser and comparison to the microresonator-based dual-comb spectrum. The residual difference between the two spectra is shown in green. (**b**) Overlay of the directly measured optical spectrum and the dual-comb spectrum showing line-by-line matching. The vertical positions of the two spectra are adjusted to compensate insertion loss.

3.3 Higher Spectral Resolution : Lower Repetition Rate Solitons

In the previous section, $H^{13}CN$ gas cell is pressurized to have $\sim$ 25 GHz linewidth, which is larger than 22 GHz spectral spacing of soliton microcombs. Although the comb spacing is slightly narrower than the absorption linewidth, the measured absorption spectra shown in figure 3.5 is still choppy.

In practice, various gases typically have several-GHz absorption linewidth at atmospheric pressure. To resolve the absorption spectral lines better, microcombs with narrower spectral spacing (smaller FSR) are preferred. Figure 3.6 shows the simulated absorption spectra of $H^{13}CN$ with three different comb spacings (100 GHz, 22 GHz, and 1 GHz). With 100 GHz FSR, the 25 GHz absorption linewidth is hardly resolved and the characteristic

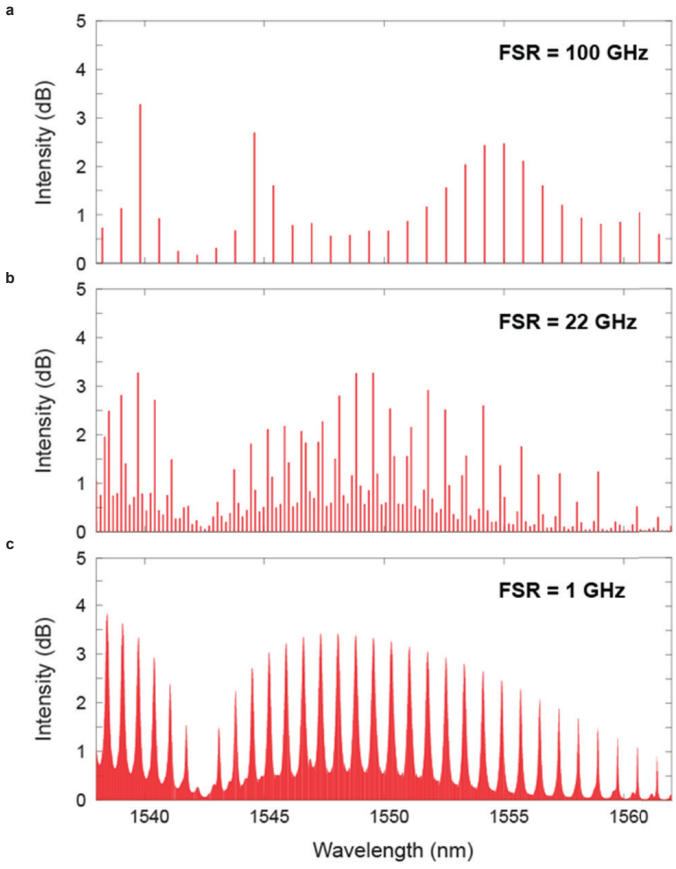

Figure 3.6: **Simulated absorption spectra with varying free spectral range (FSR).** (a) 100 GHz, (b) 22 GHz, and (c) 1 GHz.

spectral envelop of $H^{13}CN$ $2\nu_3$ band is also difficult to notice. When FSR is 22 GHz, the simulated result shows the absorption spectrum similar to the measured spectrum in figure 3.5. If FSR is further narrowed down to 1 GHz, all the absorption lines are clearly resolved in addition to the characteristic spectral envelop. By this simple simulation with varying FSR, we could confirm the sampling-induced choppiness can be removed by making dual-comb source with finer spectral spacing.

For higher spectral resolution, soliton microcombs having three different spectral spacings (15 GHz, 11 GHz, 9 GHz) are experimentally demonstrated. Figure 3.7(a-c) shows the optical spectra and the corresponding electrical spectra are also shown in figure 3.7(d-f). In principle, solitons having the repetition frequency smaller than 9 GHz is possible, although there are technical issues to improve Q-factor in larger devices. As an aside, a 2.4 GHz non-soliton microcomb has been reported[32].

For higher spectral resolution, we can also modulate the microcombs by an integer fraction of the repetition rate using an electro-optical modulator in addition to the development of larger devices.

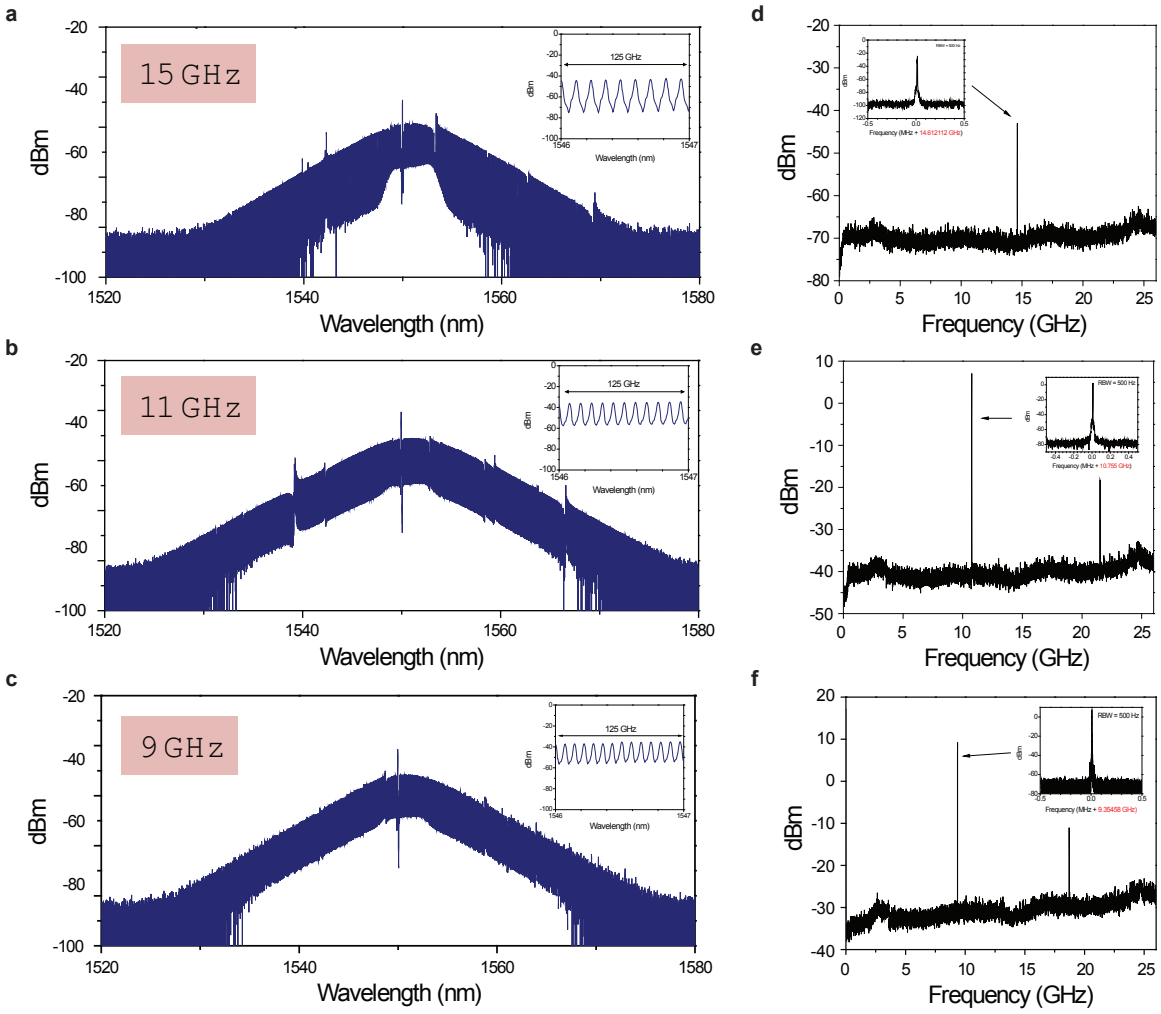

Figure 3.7: **Soliton microcombs with narrower FSR.** Optical spectra of solitons with lower repetition frequencies: (a) 14.6 GHz, (b) 10.7 GHz, and (c) 9.37 GHz. Electrical spectra are also shown in (d-f).

3.4 Higher Signal-to-Noise Ratio : Dual-Soliton Source from Single Microresonator.

In section 3.2, dual-soliton source is generated from two fiber lasers and two independent microresonators. Because the two soliton microcombs are not mutually locked, the linewidth of heterodyned signals is ∼50 kHz and signal to noise ratio is limited to 30 dB. To improve the signal-to-noise (SNR) ratio and the linewidth, phase-locking of the two microcombs is necessary. External phase-locking is one straightforward way. In this section, dual-soliton source is generated from single laser and single microresonator. By this method, SNR can be improved and the dual-soliton generation system can be simplified.

Figure 3.8(a) shows the dual-soliton source generation setup. Single fiber laser at 1550 nm is amplified by erbium-doped fiber amplifier (EDFA) and splitted by 50/50 coupler to pump the resonator in two directions. In each path, acousto-optic modulator (AOM) is used to modulate the pump power and to tune the pump frequency. Pump laser is coupled into the microresonator by evanescent coupling via fiber taper, and the polarization of the pump laser is adjusted by polarization controller (PC) to maximize pump-resonator coupling. The microresonator used in this work is shown in figure 3.8(a). It is a silica wedge disk fabricated on a silicon wafer[1], having the unloaded quality factor of approximately 300 $\sim$ 500 million and 7 mm diameter corresponding to 9.36 GHz free spectral range (FSR).

Inside the microresonator, the two pump lasers are circulating in clockwise (CW) and counter-clockwise (CCW) directions, guided by the common whispering-gallery mode near silica wedge. With the high circulating power, the combs are initiated by way of parametric oscillation [37, 38] and are broadened by cascaded four-wave mixing[27, 28]. When the CW / CCW solitons are simultaneously triggered via power-kick method[cite], the laser frequency is locked to the soliton existing detuning range by using the soliton comb power as a servo error signal.

Figure 3.8(b) shows the typical oscilloscope traces to monitor during the dual-soliton generation (not shown in figure 3.8(b) for simplicity). The generated CW / CCW soliton streams in a fiber are separated by circulators. In each soliton stream, the transmitted pump power is attenuated by fiber bragg grating (FBG) filter. To check the characteristics

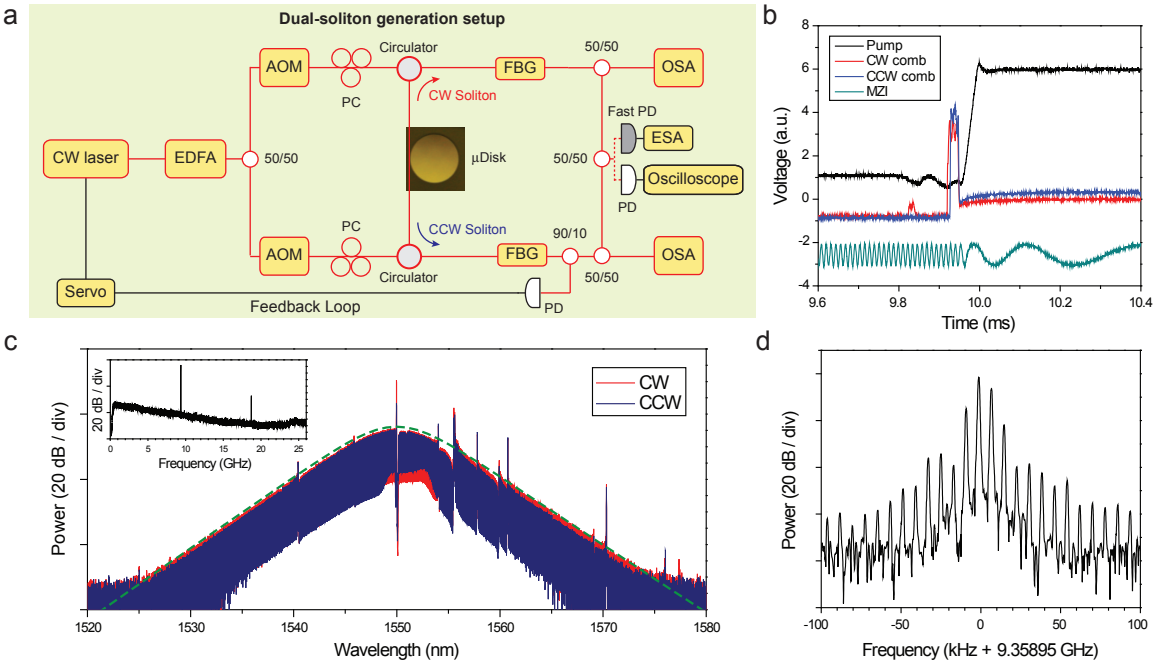

Figure 3.8: **Dual-soliton generation from single microresonator.** (a) Experimental setup for dual-soliton generation. Continuous-wave (CW) fiber laser is amplified by erbium-doped fiber amplifier (EDFA) and splitted by 50/50 coupler to pump the resonator in two directions, clockwise(CW) and counter-clockwise(CCW). In each path, acousto-optic modulator (AOM) is used to modulate the pump power and to tune the pump frequency. Pump laser is coupled into the resonator via fiber taper and polarization of the pump laser is tuned by polarization controller (PC). Solitons are triggered in both CW and CCW direction, and stabilized by a servo feedback loop using the soliton power detected at a photodetector (PD) as an error signal. The generated CW/CCW soliton streams in a fiber are separated by using circulators. In each soliton stream, the fiber bragg grating (FBG) filter is used to attenuate the transmitted pump power. Optical spectrum analyzer (OSA), electrical spectrum analyzer (ESA), and oscilloscope are used to analyze the dual-soliton source. (b) Typical signal traces observed in oscilloscope (not shown in figure 1a) for dual-soliton generation. The transmitted optical intensity(black) is reduced and brought up rapidly while suddenly stopping the laser frequency scan. MachZehnder Interferometer signal is shown in green as an indicator of the relative laser frequency. The comb powers of CW (red) and CCW (blue) soliton are monitored at the same time. (c) Typical optical spectra of CW (red) and CCW (blue) soliton. Hyperbolic-secant-square fit (green dotted curve) using the soliton pulse width of 200 fs as a fitting paramter is overlaid onto the spectra. Inset : Typical electrical spectrum. (d) Zoomed-in plot of the electrical spectrum near the repetition frequency 9.36 GHz.

of the dual-soliton source, the two soliton streams are combined and detected by 1 GHz photodetector and 50 GHz fast photodetector. The electrical spectrum and interferogram are recorded by an electrical spectrum analyzer and an oscilloscope.

Figure 3.8(c) shows the optical spectra of CW / CCW solitons within 60 nm span. The characteristic hyperbolic-secant-square function (green dotted curve) is fitted to the spectral envelop. The soliton pulse width of 200 fs is used as a fitting parameter. Figure 3.8(d) shows the electrical spectrum near the repetition frequency (f_{rep}) 9.36 GHz. Not only the two repetition frequencies of CW/CCW solitons, but also the multiple-heterodyned comblines, are also shown.

Figure 3.9(a) shows the Fourier transformed interferogram at baseband. Approximately 2.5 THz optical span is down-converted to the baseband below 5 MHz. The measured power spectral density spectrum shows the signal-to-noise (SNR) ratio $\sim$ 40 dB. The pump laser peak and mode-crossing spurs are clearly seen and corresponds to the optical spectrum shown in figure 3.8(c).

If the rf spectra below 200 kHz is zoomed-in, electrical peaks equally-spaced by $\sim$ 18 kHz can be seen (Figure 3.9(b)). It's interesting to note that the first peak starts at 0 Hz, which means that two comblines apart from the pump laser lines are overlapping in optical domain. More interestingly, the linewidth of electrical comblines become broader as the heterodyned frequency increases (Figure 3.9(c)). Near the heterodyned pump laser peak at 2.53 MHz (figure 3.9(d)), the linewidth is approximately 20 Hz. This 20 Hz linewidth is originated from AOM driver noise. This linewidth measurement clearly shows the phase-locking of the overlapping two optical comblines. If the technical noise from AOM driver is removed, the linewidth should be much narrower.

The repetition frequency difference (Δf_{rep}) between CW and CCW solitons are adjusted by tuning the frequency difference of two pump lasers (Δf_{pump}) using AOM. Typically, Δf_{rep} increases as Δf_{pump} increases within the dual-soliton coexistance pump frequency detuning range of several MHz and maximum $\Delta f_{rep} \sim$ 20 kHz is achieved when $\Delta f_{pump} \sim$ 3 MHz as shown in figure 3.9(e). It's worth noting that the current Δf_{pump} of dual-soliton coexistance is limited by the 3dB frequency shift range of AOM.

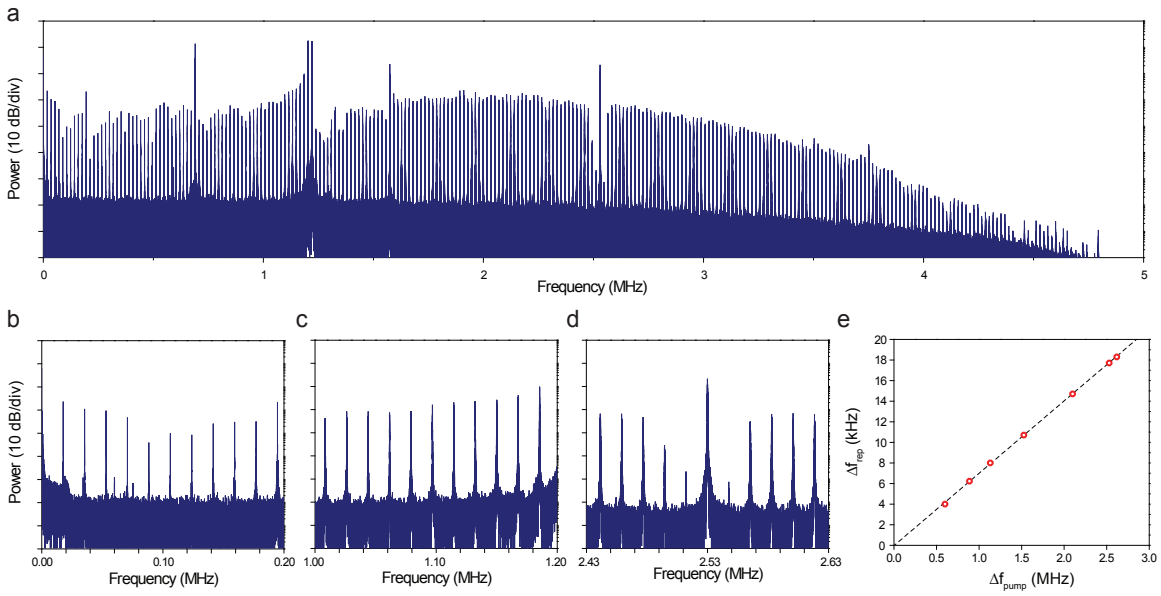

Figure 3.9: **Characteristics of dual-soliton source.** (a) Typical rf spectrum of the dual-soliton source. (b) Rf spectrum at baseband ($<$ 200 kHz). (c) Rf spectrum between 1 MHz and 1.2 MHz. (d) Rf spectrum near the pump beatnote at 2.53 MHz. (e) Repetition frequency difference (Δf_{rep}) versus pump frequency difference (Δf_{pump}).

3.5 Expanding Spectral Coverage : Stokes Soliton and Methane (CH_4) Detection

Because the molecular fingerprints of various chemicals exist over a wide wavelength range[59], expanding the spectral coverage of soliton microcombs has immense spectroscopic importance. In previous sections, soliton microcombs are generated within 1.5 μm - 1.6 μm band by pumping the silica microresonator using a continuous-wave laser with 1.55 μm wavelength. Basically, pumping the microresonator using lasers at different wavelengths can generate solitons centered at the new wavelengths if several important conditions are met: First, the microresonator must feature anomalous dispersion at the new wavelength, which can be achieved by the combination of choosing a proper material and designing the microresonator geometry. Second, the microresonator must feature low optical loss (high Q-factor) and high enough Kerr nonlinearity at the wavelength to excite the parametric oscillation and cascaded four-wave-mixing. Third, there must be optical components (laser, optical amplifier, AOM, optical filter, photodetector, etc.) at the wavelength, which can generate and manage high optical power.

In addition to pumping at different wavelenths, there are other ways to expand the spectral coverage of soliton microcombs. Dispersion of the microresonator can be engineered to generate coherent dispersive waves that broaden the soliton spectrum within the microresonator[41]. Stokes soliton can be also generated at Raman-shifted wavelenths through Raman amplification and Kerr-nonlinearity-induced trapping in the presence of a primary soliton at the pump wavelength[64]. In this section, Stokes soliton will be discussed as a method to expand the spectral coverage for methane detection.

Methane (CH_4) is the primary component of natural gas, which is a promising clean energy source due to the lower CO_2 emission during the burning process [65]. However, the leakage from the natural gas production sites and transport pipes is an important environmental issue, because methane itself is a green-house-has (GHG) having higher energy trapping efficiency than CO_2 [66, 67]. For this reason, it is highly important to develop a methane detector which is fast, sensitive, and widely field-deployable. Furthermore, methane detection is of great interest to fundamental science. For example, analyzing the

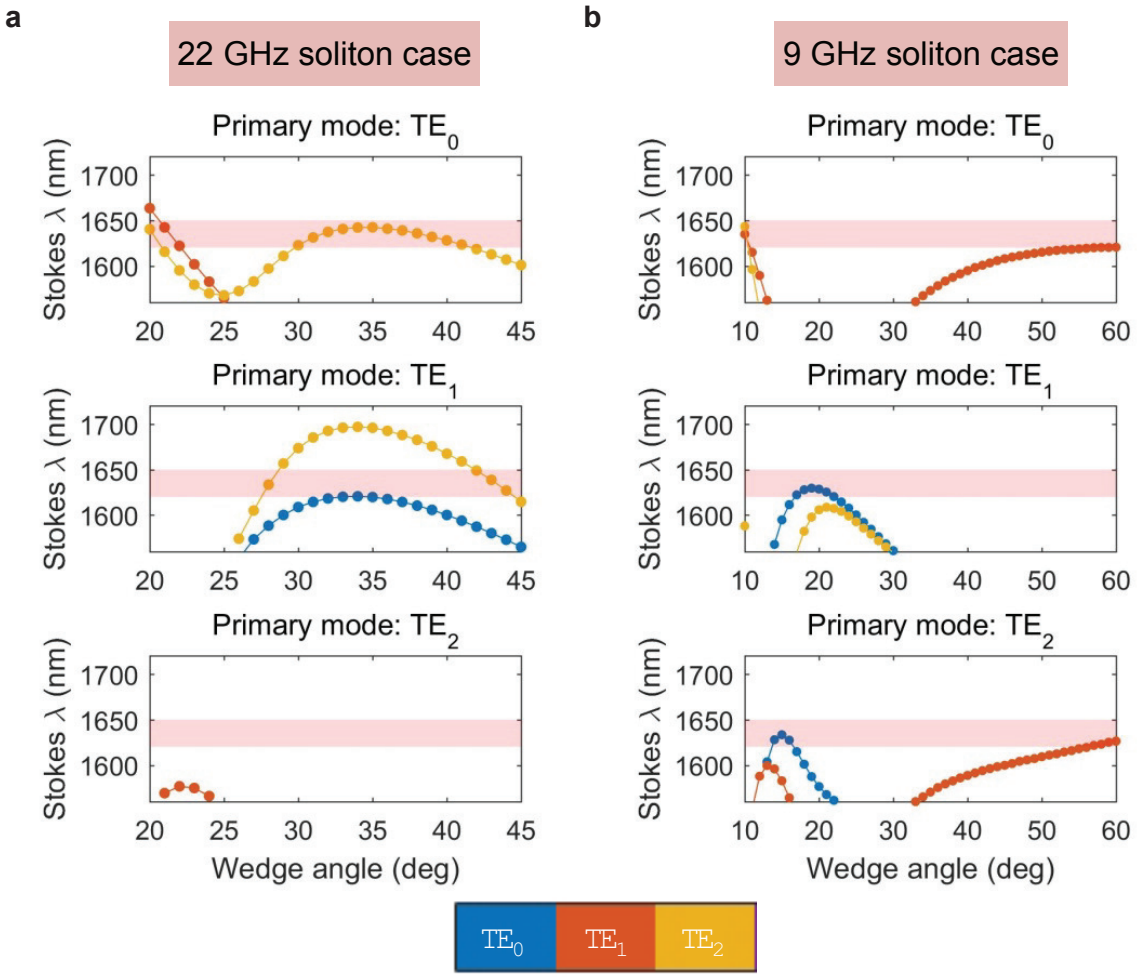

Figure 3.10: **Primary-Stokes mode pair analysis using COMSOL** From the FSR matching condition, the optical mode pairs of the primary mode at 1550 nm and the Stokes mode at the wavelength range of Methane absorption spectrumn are found. Three lowest TE modes are used as the primary modes (Top panel : TE_0, middle panel : TE_1, bottom panel : TE_2) The mode indices of Stokes modes are indicated by the legend colors. The pink area is the target wavelength range for Methane R-branch detection. (a) 22 GHz device case (resonator diameter $\sim$ 3 mm) (b) 9 GHz device case (resonator diameter $\sim$ 7 mm)

biological contribution to the methane formation can help find the evidence of life on planets like Mars [68, 69, 70, 71].

There are commercially available methane detectors, e.g., electrochemical sensors [72, 73] and semiconductor gas sensors [74], which measure physical changes induced by chemical reaction when in contact with certain gases. These gas sensors are typically small and low-cost. Some of them can provide ppm level sensitivity [72]. However, they require direct contact with gases, making it difficult for remote sensing. More importantly, these sensors are sensitive to more than one chemical species [72] and this makes it challenging to identify the leakage of a certain chemical species. On the other hand, traditional analytical instruments such as chromatography and mass spectrometry [75, 76] can also be used, but these instruments are relatively bulky and expensive. Optical detection methods, such as scanning laser spectroscopy, are also possible and enables remote sensing and identification of chemical species.

Here, methane detection by using Stokes soliton at the wavelength around 1.66 μm will be discussed. The generation of Stokes solitons from primary soliton at the pump wavelength requires certain conditions. The primary soliton creates a spatial variation of

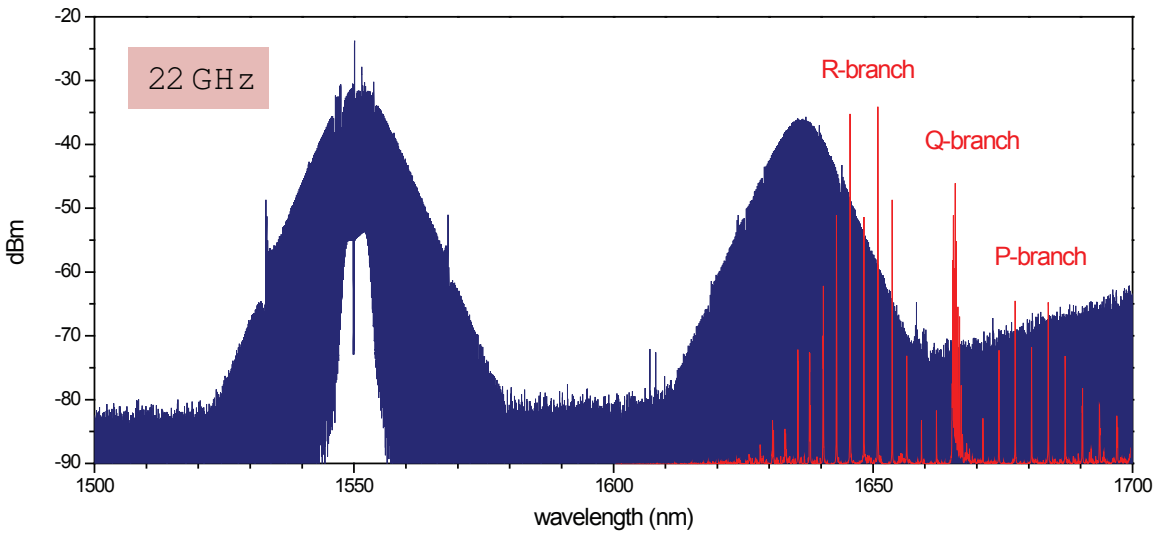

Figure 3.11: **Stokes soliton for Methane R-branch detection.** Primary soliton near 1550 nm and Stokes soliton near 1635 nm generated from 22 GHz microresonator. The red spectrum is the simulated absorption spectrum of Methane at 1 atm.

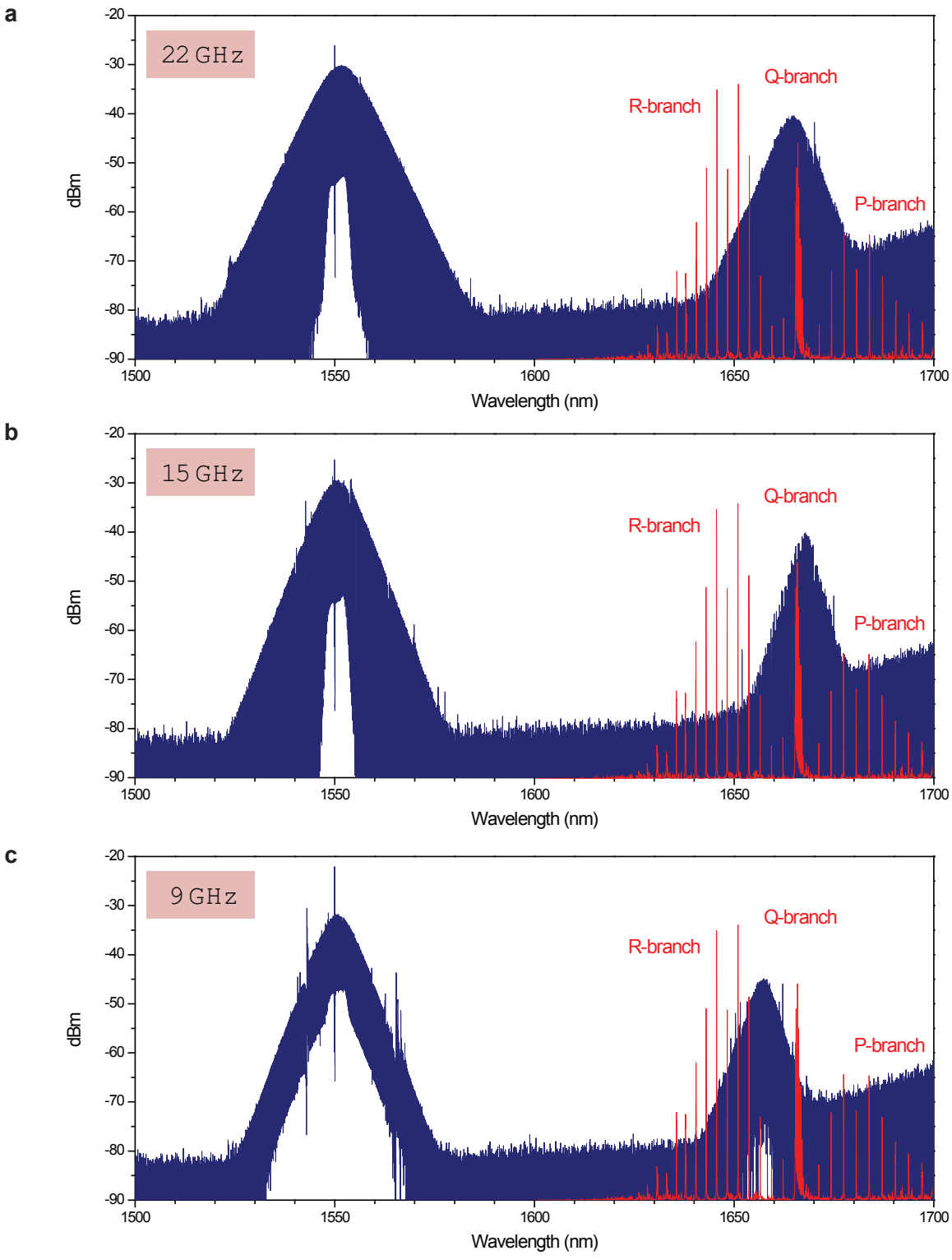

Figure 3.12: **Stokes solitons for Methane Q-branch detection.** Primary soliton near 1550 nm and Stokes soliton near 1665 nm are generated from microresonators of different repetition frequencies. (a) 22 GHz. (b) 15 GHz. (c) 9 GHz.

refractive index via the Kerr nonlinearity, which serves as an effective potential well to trap the Stokes soliton. Also, the primary soliton creates spatial Raman gain profile. The effective potential well and Raman gain propagate together with the primary soliton at the same group velocity. Actually, the group velocities, i.e. the repetition frequencies, of the primary and Stokes solitons are locked due to Kerr-mediated cross-phase modulation. Therefore, to generate the Stokes soliton, there must exist two optical modes having close free-spectral-range (FSR) values: primary mode at pump wavelength and Stokes mode at the Raman-shifted wavelength having a good mode overlap with the primary mode and high enough Raman gain.

To design the microresonator structure for Methane detection, optical mode spectrum analysis is performed using COMSOL. Silica wedge angle is used as a single variable that changes the resonator dispersion. At different wedge angles within the fabricable range from 10 degree to 50 degree, the primary mode at 1550 nm is determined first. Then, the Stokes modes with the same FSR are found at the wavelength range of Methane absorption spectrum. Figure 3.10 shows the example of this primary-Stokes mode pair analysis in 22 GHz and 9 GHz device cases.

Figure 3.11 is the optical spectrum of 22 GHz Stokes soliton generated for Methane R-branch detection. Absorption spectra of Methane at 1 atm is simulated using HITRAN Application Programming Interface (HAPI) and overlaid as red spectrum in the figure 3.11. Because the 22 GHz spectral spacing relatively large compared to the linewidth of Methane absorption peaks ($<$ 15 GHz near 1550 nm at 1 atm), it's better to measure the characteristic envelop of Methane absorption spectrum in addition to resolving each absorption peak. The methane Q-branch, where many absorption peaks are densely located within a narrow wavelength range, is targeted to measure for this reason. 22 GHz device is further optimized to generate Stokes soliton at the Methane Q-branch wavelength. Experimentally, this optimization was made possible by increasing the HF etching time, which results in a larger wedge angle.

Figure 3.12(a) shows the 22 GHz Stokes soilton spectrum, which is centered at Methane Q-branch wavelength near 1665 nm. To improve the spectral resolution, the same optimization process is performed for 15 GHz and 9 GHz devices and successful generation

of Stokes solitons near 1665 nm was possible. Figure 3.12(b-c) are the measured optical spectra showing 15 GHz and 9 GHz Stokes solitons. In figure 3.12(c), the center frequency of Stokes soliton is not well aligned to the Q-branch and efforts are being made for further optimization.

After developing devices that can generate 9 GHz Stokes soliton at Methane Q-branch wavelength, dual-comb spectroscopy measurement will be performed. To improve the signal-to-noise of the dual Stokes soliton source, counter-propagating Stokes solitons are also demonstrated, as shown in figure 3.13.

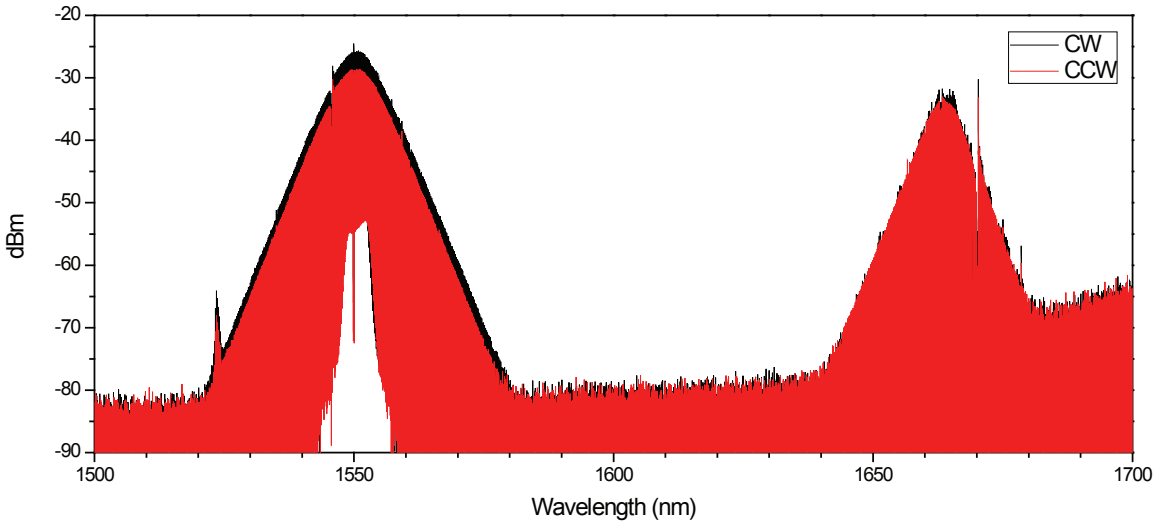

Figure 3.13: **Counter-Propagating Stokes soliton for Methane Q-branch detection.** Primary soliton near 1550 nm and Stokes soliton near 1665 nm generated from 22 GHz microresonator. Both clockwise (CW ; black) and counter-clockwise (CCW ; red) Stokes solitons are generated to improve the signal-to-noise of dual Stokes soliton source.

Chapter 4

Microresonator Soliton LIDAR

Distant detection is important in wide range of areas including autonomous vehicles, robotics, large scale manufacturing, formation-flying satellite, and basic science like gravitational wave detection. With the advent of optical frequency comb technology, coherent laser ranging systems using frequency combs enabled unprecedented absolute distance measurements with larger ambiguity range and faster update rate, which were not possible in conventional ranging technology. However, optical frequency combs are typically bulky and expensive systems which hinder the widespread use of many comb-based technologies. As compact, inexpensive, and potentially integrable comb sources, miniature frequency combs (or microcombs) have been developed and soliton mode-locking become possible for better utilization of microcombs. In this work, distance detection is demonstrated using a dual-soliton microcomb source generated from single pump laser and single microresonator. From the time-of-flight measurement, 200 nm precision at 500 ms averaging time is achieved.

4.1 Introduction

Typical interferometric distance measurement with a single wavelength provide sub-nanometer precision, but the ambiguity range is limited to half of the optical wavelength[77]. On the other hand, pulsed or frequency-modulated laser distance measurement systems offer ambiguity ranges larger than meter, but with limited precision [78, 79].

Since the invention of optical frequency comb, various comb-based distance measure-

ments have been demonstrated, including multi-heterodyne interferometry[80], comb-calibrated multi-wavelength interferometry[81], comb-calibrated frequency modulated continuous wave (FMCW) laser interferometry[82], and time-of-flight measurement[83]. Because frequency comb is a highly coherent multi-wavelength laser source, these comb-based laser radar (LIDAR) systems provide more precise and longer-range distance measurement. Ultimate precision of these comb-based LIDAR systems is derived from the fractional frequency instability of rf timebase and optical frequency which are used to stabilize the frequency comb. Combined with an optical clock having the state-of-art fractional frequency instability of $< 10^{-17}$, an absolute distance measurement with nm-precision is possible at long range $\sim 10^5$ km, which is the order of the distance from Earth to Moon.

The challenge for the widespread use of comb-based LIDAR system lies in the coherent dual-comb source, which is typically bulky and expensive. There have been continued efforts to develop a smaller, cheaper, and environmentally robust dual-comb source. Besides conventional comb technologies such as fiber-based mode-locked lasers, miniature optical frequency comb or microcomb[27, 28] using naturally-compact microresonators have been demonstrated in several material systems[27, 29, 30, 31, 32, 33]. Some are monolithic on silicon chip and integrable with other silicon photonic components[34, 35, 36], which allows significant cost reduction by a mass production. A major advancement in microcombs has been the realization of soliton mode-locking[39, 40, 41, 42, 43], which naturally provides phase-locked femtosecond pulses with repetition rates ranging from several GHz to THz. Microresonator-based soliton microcombs are used to demonstrate the existing frequency comb applications, such as an optical frequency synthesizer[84], and dual-soliton sources are also demonstrated[85, 86, 87] and applied to dual-comb spectroscopy[85, 86]. In this work, we demonstrate time-of-flight distance measurement using chip-based dual-soliton source. To make the system simpler and improve mutual coherence between the two combs, a single pump laser and single resonator are used.

4.2 Distance Measurement using Microresonator Dual-Soliton Source

Figure 4.1 shows the experimental setup, which can be largely divided into two parts: dual-soliton source generation setup (left green panel) and LIDAR setup (right blue panel). Single fiber laser at 1550 nm is amplified by erbium-doped fiber amplifier (EDFA) and splitted by 50/50 coupler to pump the resonator in two directions. In each path, an acousto-optic modulator (AOM) is used to modulate the pump power and to tune the pump frequency. The pump laser is coupled into the microresonator by evanescent coupling via fiber taper, and the polarization of the pump laser is adjusted by polarization controller (PC) to maximize pump-resonator coupling. The microresonator used in this work is shown in figure 1a. It's a silica wedge disk fabricated on a silicon wafer[1], having the unloaded quality factor of approximately 300 $\sim$ 500 million and 7 mm diameter corresponding to 9.36 GHz free spectral range (FSR).

Inside the microresonator, the two pump lasers are circulating in clockwise (CW) and counter-clockwise (CCW) directions, guided by the common whispering-gallery mode near silica wedge. With the high circulating power, the combs are initiated by way of parametric oscillation [37, 38] and are broadened by cascaded four-wave mixing[27, 28]. Solitons are triggered in both CW and CCW directions and stabilized using a feedback loop[48]. Figure 4.2(a) shows the typical oscilloscope traces to monitor during the dual-soliton generation (not shown in figure 4.1 for simplicity). The generated CW / CCW soliton streams in a fiber are separated by using circulators. In each soliton stream, the transmitted pump power is attenuated by fiber bragg grating (FBG) filter. Figure 4.2(b) shows the optical spectra of both solitons within 60 nm span. The characteristic hyperbolic-secant-square function (green dotted curve) is fitted to the spectral envelop, showing the soliton pulse width of 200 fs.

To check the characteristics of the dual-soliton source, the two soliton streams are combined and photodetected (red dotted path in figure 4.1). Figure 4.2c shows the rf power spectral density within 26 GHz bandwidth of electrical spectrum analyzer (ESA). The measured repetition frequency (f_{rep}) is 9.36 GHz and the multiple heterodyne signal near f_{rep}

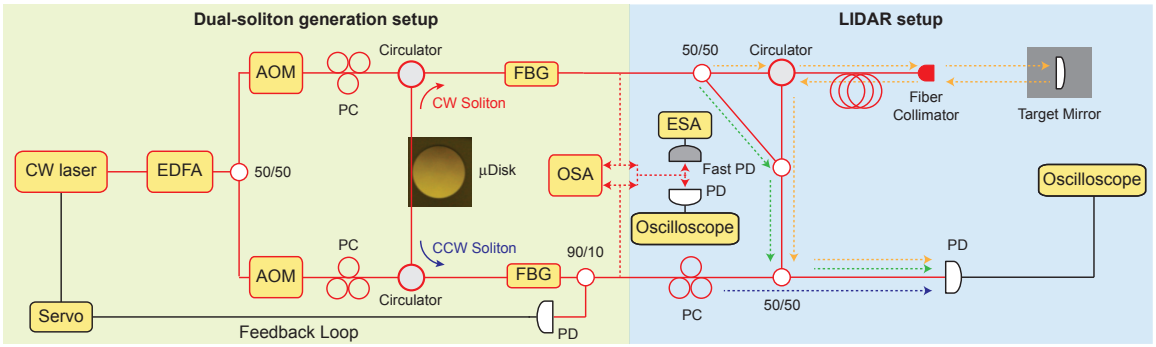

Figure 4.1: **Experimental setup.** The experimental setup consists of dual-soliton generation setup and LIDAR setup. Continuous-wave (CW) fiber laser is amplified by erbium-doped fiber amplifier (EDFA) and splitted by 50/50 coupler to pump the resonator in two directions, clockwise(CW) and counter-clockwise(CCW). In each path, acousto-optic modulator (AOM) is used to modulate the pump power and to tune the pump frequency. Pump laser is coupled into the resonator via fiber taper and polarization of the pump laser is tuned by polarization controller (PC). Solitons are triggered in both CW and CCW direction, and stabilized by a servo feedback loop using the soliton power detected at a photodetector (PD) as an error signal. The generated CW/CCW soliton streams in a fiber are separated by using circulators. In each soliton stream, fiber bragg grating (FBG) filter is used to attenuate the transmitted pump power. Optical spectrum analyzer (OSA) and electrical spectrum analyzer (ESA) are used to analyze the dual-soliton source. For distance detection, CW soliton stream is splitted in two paths: reference path (green dotted line) and target path (yellow dotted line). The target path includes a circulator to redirect reflected signal, fiber patch cord, fiber collimator, and mirror. CW Soliton streams of both paths are combined with CCW soliton stream (blue dotted line) and photodetected.

is shown in figure 4.2d. The linewidth of each electrical combline is approximately 20 Hz, which is limited by AOM driver noise. The repetition frequency difference (Δf_{rep}) between CW and CCW solitons are adjusted by tuning the frequency difference of two pump lasers (Δf_{pump}) using AOM. Typically, Δf_{rep} increases as Δf_{pump} increases within the dual-soliton coexistance pump frequency detuning range of several MHz and maximum $\Delta f_{rep} \sim 20$ kHz is achieved when $\Delta f_{pump} \sim 3$ MHz. The current Δf_{pump} of dual-soliton coexistance is limited by the 3dB frequency shift range of AOM. The time-domain voltage signal, or interferogram, from the photodetector is also recorded by an oscilloscope (Figure 1(f)). It's worth noting that the linewidths of electrical comblines near the pump laser beatnote at Δf_{pump} is approximately 20 Hz, which is limited by AOM driver noise. The linewidths of the electrical comblines become continuously narrower as the frequency of comblines decrease from Δf_{pump} to 0 Hz, which indicates the phase locking of the CW and CCW solitons through the spectrally overlapping optical comb teeth[88].

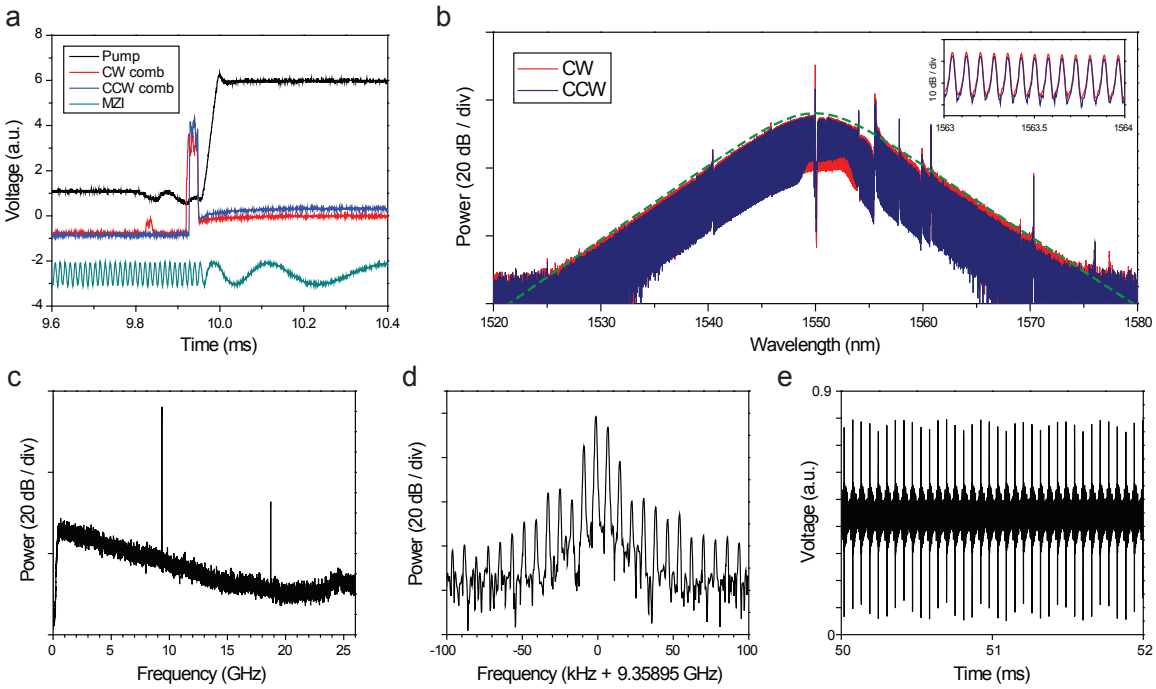

Figure 4.2: **Characteristics of microresonator dual-soliton source**. (a) Typical signal traces observed in oscilloscope (not shown in figure 1a) for dual-soliton generation. The transmitted optical intensity(black) is reduced and brought up rapidly while suddenly stopping the laser frequency scan. MachZehnder Interferometer signal is shown in green as an indicator of the relative laser frequency. The comb powers of CW (red) and CCW (blue) soliton are monitored at the same time. (b) Typical optical spectra of CW (red) and CCW (blue) soliton. Hyperbolic-secant-square fit (green dotted curve) using the soliton pulse width of 200 fs as a fitting paramter is overlaid onto the spectra. (c) Typical electrical spectrum of the microresonator dual-soliton source with 9.36 GHz repetition frequency. (d) Zoomed-in plot of the electrical spectrum near the repetition frequency. Repetition frequency difference is typically $0 \sim 20$ kHz. (e) Typical interferogram of dual-soliton source.

4.2.1 Time-Of-Flight Distance Measurement

The two soliton streams are plugged into the LIDAR setup shown in figure 4.1 (right blue panel). CW soliton stream is used to acquire the distance information. It is split into reference path and target path via 50/50 coupler and the CW soliton stream in the target path passes through optical components such as a circulator, fiber patch cords, and a gradient-index (GRIN) collimator, and reflected back at a target mirror. The reflected target CW soliton stream is separated by the circulator and combined with the reference CW soliton stream. The measured distance is the distance difference between the reference path and target path. One-way fiber pathlength difference is approximately 18 m and the air gap between the fiber collimator and target mirror is approximately 0.02 m. Finally, the CW soliton stream having distance information is combined with a CCW soliton stream to generate interferogram. The polarization of CCW soliton stream is adjusted to maximize the target reflection peaks in the interferogram.

Figure 4.3(a) shows the measured interferogram with ranging information which is measured by the oscilloscope. Voltage signal from the photodetector is recorded for 2 seconds with 250 ns sampling time and only 5 ms span is shown. Figure 4.3(b) is the zoomed-in interferogram showing reference peaks and target peaks within two time periods. Time period is 176 μs, which corresponds to $\Delta f_{rep} \sim 5.685$ kHz. The intensity peaks of the electrical pulse stream are detected by Hilbert transforming the interferogram and the time interval between a reference peak and a target peak is calculated at each period. After removing the time period uncertainty induced by the drift of Δf_{rep}, the time interval is converted to the distance scale and plotted with a time increment of 176 μs period. Figure 4.3(c) left panel shows the measured distance over 2 seconds. The zero distance plane and red circle trace represent the reference peak and the target peak, respectively. The average distance is 4.637429 mm with 16 mm range ambiguity, which is derived from 9.36 GHz soliton pulse repetition frequency. One time period of the Hilbert transformed interferogram near 1 s (the dotted line in left panel) is also shown in the right panel. In the inset of the right panel, the target intensity peak is zoomed-in, which shows the full-width half-maximum pulse width ~ 1.45 μs.

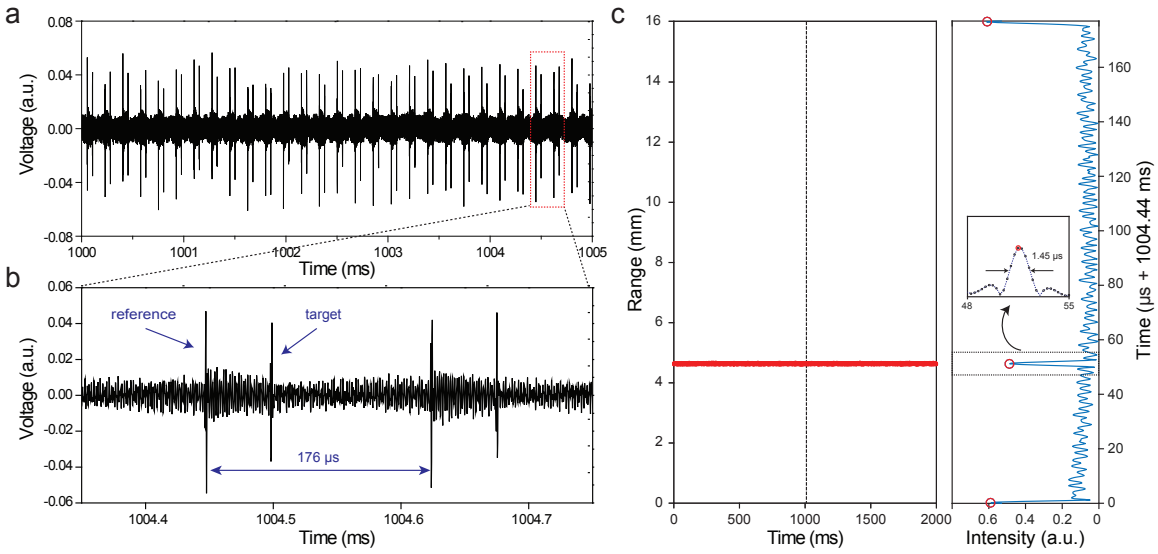

Figure 4.3: **Distance measurement.** (a) The interferogram having range information. Voltage out of the photodetector is measured for 2 seconds using the oscilloscope and only 5 ms time span is shown. (b) Zoom-in of the interferogram showing two time periods. The reference peaks and target peaks are shown and the time period is approximately 176 μs (c) The measured distance between the reference peak and target peak is shown with 16 mm range ambiguity (left panel). Intensity peaks are found from the Hilbert transformed interferogram and the distance calculated from the time interval is plotted at every time period. The corresponding electrical intensity trace (blue) and peaks (red circle) near 1 s is also shown (right panel). Inset : Zoom-in of the target intensity peak showing the electrical pulse width of 1.45 μs.

4.2.2 Precision of Distance Measurement and Resolving Ambiguity Range

Figure 4.4 shows the precision of the time-of-flight distance measurement. Allan deviations of the time-series distance are calculated at the averaging time ranging from 352 μs to 667 ms. The measured precision is σ = 10 μm $(T_{update}/T)^{1/2}$, where $T_{update} \sim$ 176 μs is the update time and T is the averaging time. This scatter results from $\sim$ 35 fs residual timing jitter between the two solitons, which is originated from AOM driver noise. Near 500 ms averaging time, 200 nm precision is achieved and this level of precision is close to $\sim 10^{-7}$ uncertainty from the environmental fluctuation [77].

The distance measurement shown in figure 4.3(c) has the range ambiguity of 16 mm. To resolve the ambiguity, similar distance measurement is performed after swapping the role of two soliton streams and Vernier effect[80] is used. Figure 4.5 shows the two distance measurements, where R_{CW} (red circle) and R_2 (blue cross) are the measured distances when CW soliton and CCW soliton are used respectively for ranging. The average distance difference (ΔR = Mean(R_{CW}) - Mean(R_{CCW})) between the two measurements is 16.02 μm. Considering Vernier effect, the ambiguity-resolved distance is $R' = \Delta R(f_{rep}^{CCW}/\Delta f_{rep}) + R_{CW} \approx$ 26.3729 m $\pm$ 0.466 m with a new ambiguity range of $\sim$ 26 km. The measured distance is in good agreement with the one-way optical path length difference of 26.815 m, which is measured by optical time-domain reflectometer (Luna OBR 4400).

In current work, the update time of $\sim$ 176 μs and the new ambiguity range of $\sim$ 26 km are determined by Δf_{rep} = 5.685 kHz, which can be tuned by Δf_{pump} change. For the applications requiring faster update rate, increasing Δf_{rep} to 1 MHz can improve the update time to 1 μs with the reduced ambiguity range of 150 m. The precision can be improved by reducing the residual noise of dual-soliton source which is currently limited by the technical noise from AOM. Complementary interferometric measurement in addition to the time-of-flight can also improve the precision[80].

Microresonator-based dual-soliton source generated from single pump laser and single resonator can miniaturize and simplify the conventional dual-soliton system with the im-

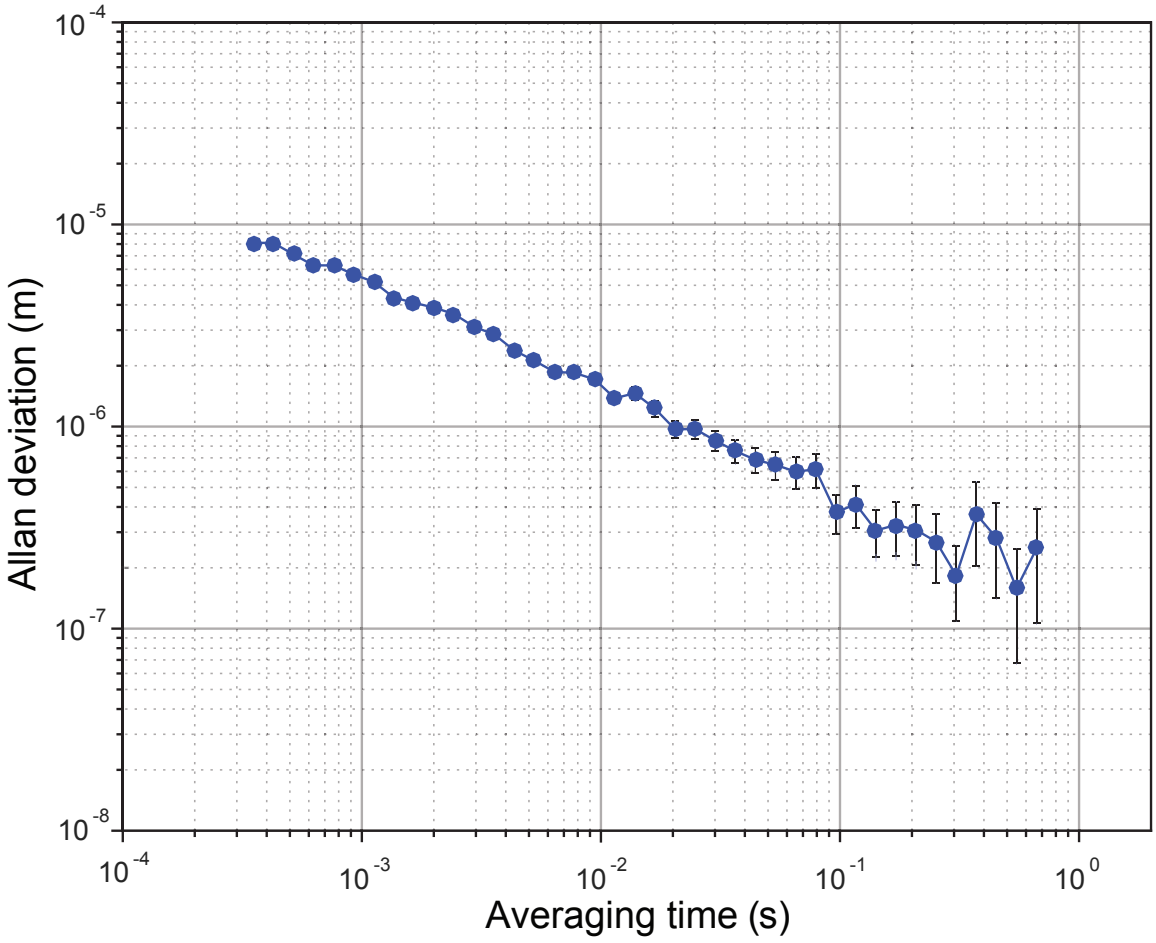

Figure 4.4: **Precision of distance measurement versus averaging time.** Allan deviation is calculated from the 2 s time series of measured distance from the reference peak to signal peak. 200 nm precision is achieved near 500 ms averaging time. Error range is calculated from the Allan deviation divided by square root of sample size.

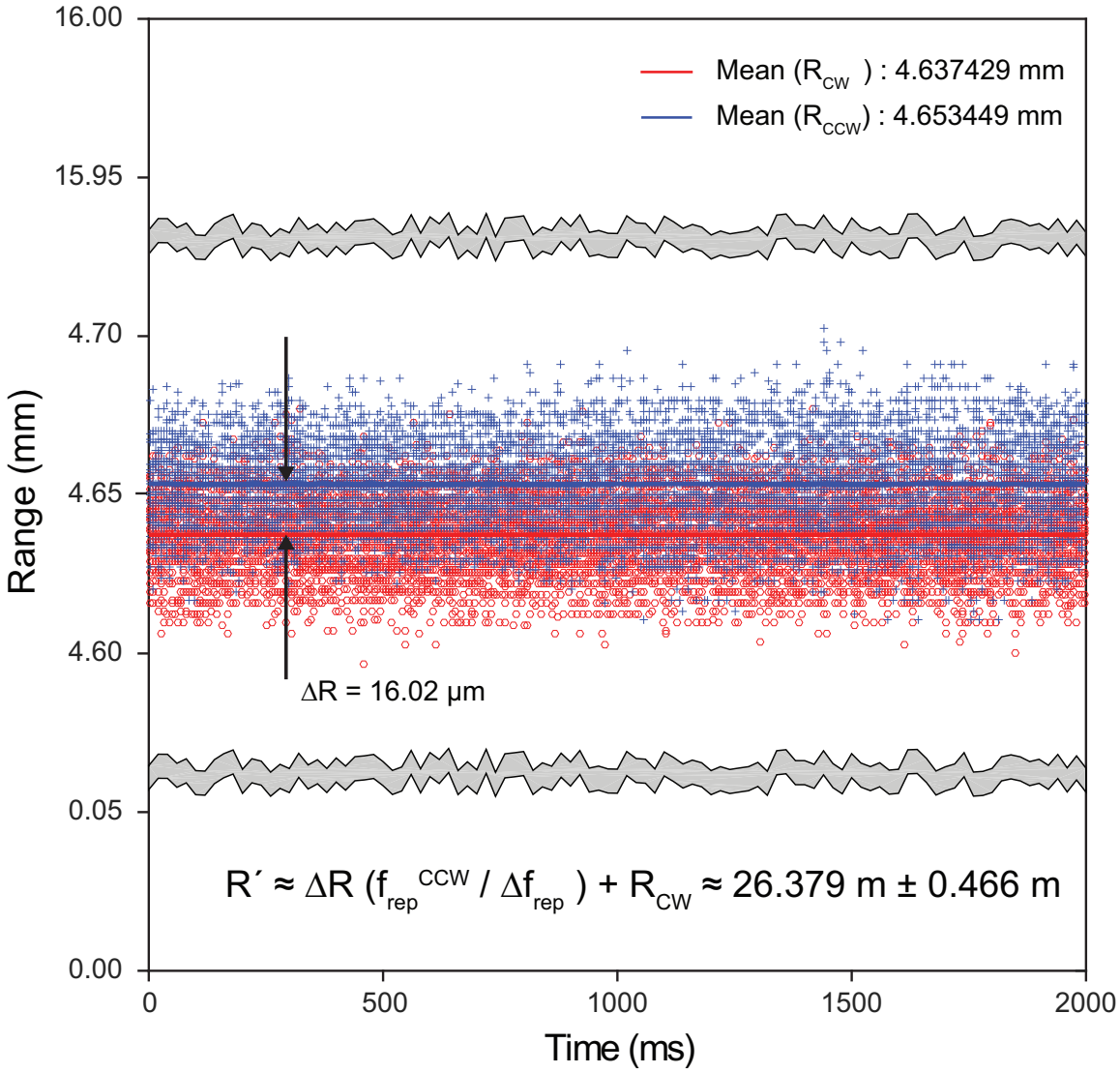

Figure 4.5: **Resolving range ambiguity.** Two distance measurements are performed by swapping the function of two solitons. R_{CW} (red circle) is when CW soliton with the repetition rate of f_{rep}^{CW} is used for ranging and R_{CCW} (blue cross) is when CCW soliton with the repetition rate of f_{rep}^{CCW} is used for ranging. The distance difference (ΔR = Mean(R_{CW}) - Mean(R_{CCW})) between the two measurements is 16.02 μm. Considering Vernier effect, this indicates the ambiguity resolved distance (R') is 26.3729 m $\pm$ 0.466 m. Δf_{rep} is the repetition rate difference between CW soliton and CCW soliton.

proved mutual coherence. Using waveguide-integrated structure[89], the chip-based dual-soliton source can be integrated with other on-chip optical components, such as optical phased array, for LIDAR system. Our work shows the potential of chip-based dual-soliton sources toward compact coherent-LIDAR systems, which features high precision, fast update rate, and large-range ambiguity.

Chapter 5

On-Chip Spiral Reference Cavity : Frequency Stabilization and Low-Noise Microwave Generation

Frequency references are indispensable to many applications requiring the precision measurement of time and frequency, including navigation, communication, remote sensing, and basic science. Over the past decades, laser-based optical technologies have been applied to the time-keeping systems that can potentially revolutionize all of these areas. Currently, the most precise clocks are based on a frequency-stabilized laser with short-term stability that is derived from an optical reference cavity and long-term stability derived from an atomic transition. In addition, the lowest noise microwave signals are now generated from a cavity-stabilized laser by dividing the stable optical frequency down to microwave rates using an optical frequency comb. Despite the improvement in the precision, these optical systems remain bulk and complex laboratory systems. Thus, there are significant interests and a lot of efforts are being made in the prospect of miniaturization of these systems, even towards integrated systems on a chip. While progress in microcombs, as discussed in chapters 2-4, provides the possibility of a chip-scale frequency divider and synthesizer, a miniature stable frequency reference is still a missing component for the compact optical systems in the precise timing applications. In this chapter, a chip-based optical reference cavity having a spiral design is described and its properties are studied. This new kind of optical reference cavity enhances the fundamental frequency stability by spatially averaging the thermorefractive noise of the resonator. The ultimate performance of the devices is also

studied theoretically. The spiral reference cavity is also applied to generate the low-noise microwave signal via an optical frequency division method.

5.1 Introduction

Stable optical frequency reference has been studied for decades [90, 91] and has revolutionized many application areas such as communication, time keeping, low noise microwave generation, and basic science[26, 92, 93]. Such optical frequency references benefit from high optical Q factor or equivalently long optical storage time. Fabry-Perot cavities [94, 95, 96], absorption spectral-hole burning in cryogenically cooled crystals [97, 98], and long-delay-line interferometers [99, 100] are examples of such stable optical reference systems. Allan deviation (i.e. fractional frequency instability, which is a standard measure of frequency stability) of $1\text{x}10^{-16}$ at 1 s averaging [95] has been attained from the state-of-the-art Fabry-Perot optical cavities. In these systems, a narrow resonator line for laser locking is created by high-finesse-mirrors and the resonance frequency is immune to thermal fluctuations by using low-thermal-expansion housings and low-thermal-noise mirror coating [95, 94, 96, 101, 102]. However, these optical frequency reference systems remain as laboratory systems, because they are rather bulky and sometimes use cryogenic systems.

While pursuing the ultimate stabiltiy, there has been a continuing need for portable optical frequency references. Bench-top or rack-mount optical frequency systems with Hz-level linewidth is developed by miniaturizing Fabry-Perot optical cavity[103, 104]. Besides miniaturization of conventional Fabry-Perot optical cavity, attention has naturally turned towards miniature devices such as ultra-high optical-Q, solid-state resonator systems based on silica [105, 106, 107] and crystalline fluoride materials [108, 109, 110]. Besides the compact size of these devices, their reduced mass can offer improved performance with respect to shock and acceleration. Some systems are chip-based and there is the possibility of integration with other components. These compact solid-state microresonators are also demonstrated as optical reference cavities [111, 112, 113].

In solid-state microresonators, instability of resonance frequency arises from thermal fluctuations such as thermorefractive, thermomechanical, and photothermal noise [114,

115]. The former two are fundamental noise related to the material and structure of the microresonators, while the latter is determined by the laser power fluctuation which is transferred into thermal changes of the cavity refractive index and size. Typically, thermorefractive noise is the major source of the frequency fluctuation. For this reason, materials with low thermal coefficient (dependence of refractive index on temperature), dn/dT are advantageous to reduce the thermorefractive noise and the frequency noise of the system. Along these lines, locking of a laser to a MgF_2 resonator, which has low thermal coefficient in comparison to silica [115], has attained stabilization to 6x10^{-14} at 0.1 s averaging time [116]. While selecting materials and designing resonator geometry to reduce the dependence of resonance frequency on temperature, stabilizing temperature of microresonator has also been demonstrated by the dual-mode feedback control based on the measured modal temperatures of two, orthogonally-polarized modes [117, 118, 119].

In this chapter, we study a chip-based, high-Q resonator having a spiral design to reduce the thermal fluctuation induced instability of the resonance frequency. Besides being the first chip-based reference cavities, the spiral design makes the spiral reference cavity immune to thermorefractive noise, as well as thermomechanical and photothermal noise. This chip-based spiral reference cavity is applied to stabilize laser (i.e. optical) frequency and used to generate stable microwave signal via optical frequency division.

5.2 Optical Characteristics of Spiral Reference Cavity

When the laser is locked to a cavity linecenter, the rms frequency difference of the locked laser relative to a cavity line center depends upon the optical Q and signal-to-noise ratio (SNR) (the SNR depends upon integration time or servo-control bandwidth). This relationship can be written in the following expression [120].

$$\frac{\Delta\nu_{rms}}{\nu_0} \approx \frac{1}{Q \cdot SNR} \tag{5.1}$$

If the resonator has a high enough Q factor and the feedback loop provides a large enough SNR, "tight lock" can be achieved and the rms frequency difference of the locked

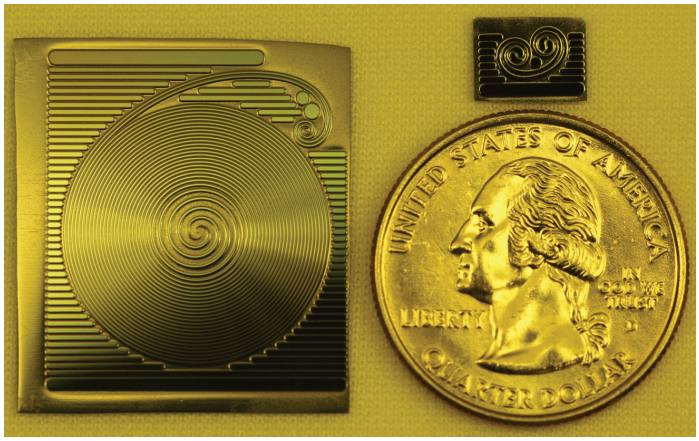

Figure 5.1: **Photograph of spiral waveguide resonators.** Left: 1.2-meter spiral resonator. Upper right: 4.5 cm spiral resonator used for studies of Q scaling. Lower right: quarter shown to provide scale.

laser relative to a cavity linecenter becomes negligible compared to the fluctuation of the cavity line center. In this case, the stability of the laser locked to the cavity becomes determined by fluctuations in the cavity line center [121], which is mainly originated from the thermorefractive noise [114, 115]. This source of noise can be reduced by increasing the optical mode volume. For this reason, long fiber delays are used in optical fiber reference cavity systems[100]. Intuitively, if there are randomly dispersed fluctuators (density ρ) in an optical mode of volume V, the combined frequency fluctuation of the mode will scale like $\sqrt{\rho V}$ assuming the fluctuators are uncorrelated. At the same time, the coupling of each fluctuator to the optical mode will vary like $\frac{1}{V}$. Therefore, the overall rms frequency fluctuation will scale like $\frac{1}{\sqrt{V}}$ or equivalently $\frac{1}{\sqrt{length}}$ in optical fibers. This scaling law can be applied to all thermal-related fluctuations in resonators [114, 115].

To apply this scaling law (increased mode volume reduces frequency fluctuation) on a silicon chip, a spiral design is adopted to the resonator geometry as shown in figure 5.1. Previously, this spiral design have been used to create narrow free-spectral-range resonators on a chip [122]. In our work, a special ultra-low-loss waveguide which feature the optical waveguide loss as low as 0.037 dB/m [107, 123] is used to achieve both high Q and large mode volume. The spiral resonators are shown in figure 5.1 and contain two interleaved spiral waveguides with S-turn adiabatic couplers at the spiral center. Details on the process used to create the waveguides are described in chapter 1. To measure the dependence of

Q factor on resonator path length, Q-factors are measured from the spiral resonators with different path lengths (4.5, 8.7, 14, 21, 40, 62, 120 cm). Two spiral resonators, longest path length and shortest path length, are shown in figure 5.1. Optical coupling to the resonators was possible using a fiber taper [124, 125] at the upper-right corner of the chip. The lower right inset of figure 5.2 shows a typical oscilloscope trace for the measurement Q-factor of the longest spiral resonator having a round-trip physical path length of 120 cm. The measured FSR of the device agrees with the FSR expected from the round trip length. It is worth noting that the observable mode spectral density is greatly reduced by the S-turn adiabatic couplers at the center of each spiral, which tend to strip high-order modes and increase optical loss for higher-order spatial modes [126]. The main panel of figure 5.2 shows the pathlength dependence on the Q-factor along with a theoretical estimate of the Q factor based upon an adiabatic coupler loss of 0.02 dB per coupler and a waveguide loss of 0.15 dB/m. The waveguide loss used for the fitting is higher than reported in earlier work on account of using a contact aligner as opposed to a projection (stepper) lithography system for the micro-fabrication of the devices [107, 123]. Nonetheless, resonators that are over 1 meter in length with Q factors in excess of 100 million (a maximum Q factor of 140 million) are demonstrated on a footprint smaller than 5.4 cm^2.

In addition to the immunity to the thermorefractive noise, these devices also provide immunity to photo-thermal noise. As a result, it is possible to obtain high SNR by increasing coupled optical power without degradation in resonator stability (see eqn. (5.1)). Thermo-mechanical noise, which scales inverse-quadratically with resonator length [127], is also greatly suppressed.

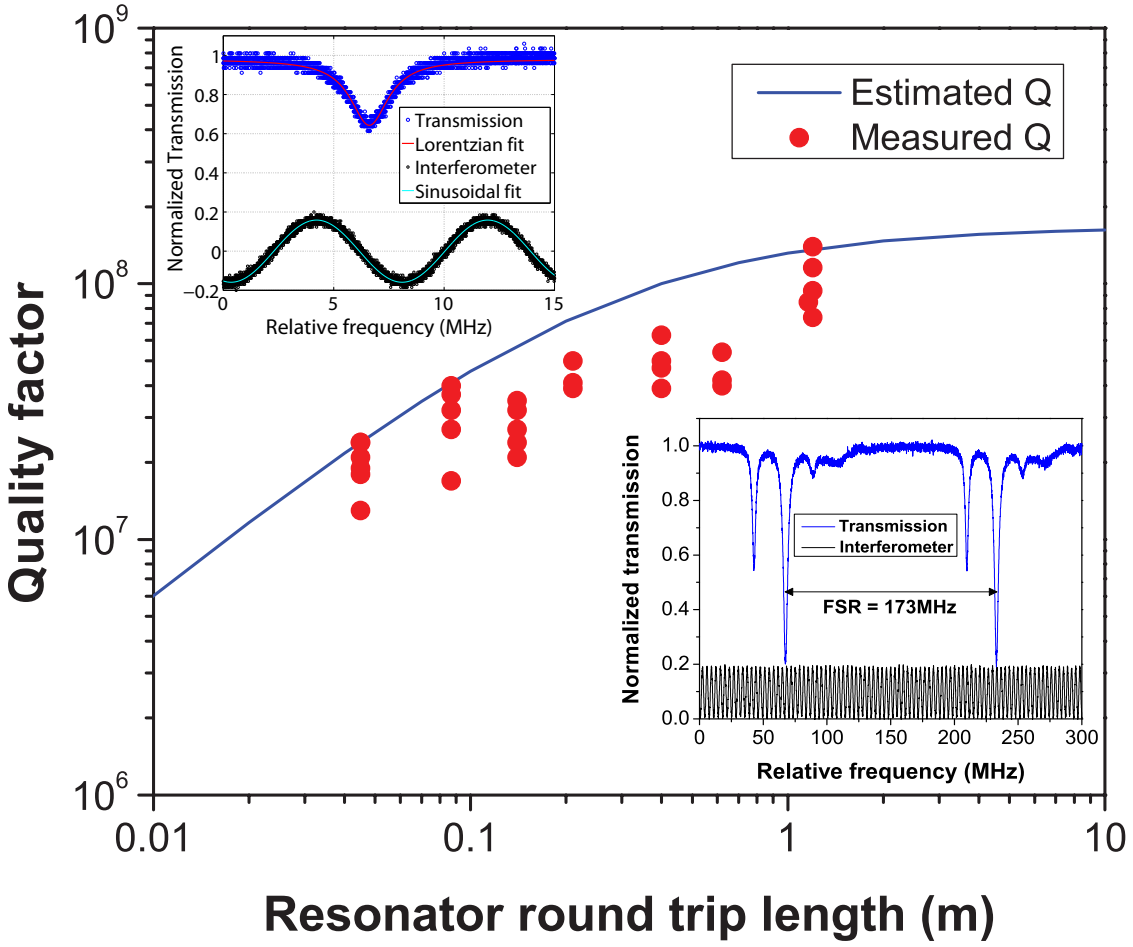

Figure 5.2: **Measured Q factor versus resonator length in meters.** The maximum Q factor obtained was 140 million at a length of 1.2 meters. The blue curve is a theoretical prediction for the Q versus length that assumes a waveguide loss of 0.15 dB/m. Upper left: a typical optical spectrum in blue. The sinusoidal curve is an interferometer scan that is used to calibrate the linewidth. Lower right: Spectral scan in excess of one free spectral range for the TE polarization. The black curve is the interferometer calibration trace.

5.3 Frequency Stabilization using Spiral Reference Cavity

The experimental setup to measure the frequency stability of the spiral resonators is shown in figure 5.3. Two fiber lasers (Orbits Lightwave, 193.43 THz) are locked to two spiral resonators with independent Pound-Drever-Hall systems [120]. The locked fiber lasers are heterodyned to generate a beat signal near 350 MHz. The instability of this beat note represents the combined instability of the two stabilized lasers and it is analyzed using an electrical spectrum analyzer, a phase noise analyzer (Rohde & Schwarz FSUP26), and a frequency counter (Tektronix FCA3120 and Pendulum CNT 91). Acoustic shielding is placed around the entire measurement setup to attenuate environmental sound noise, and most of the noisy equipment (pumps and instrumentation in adjoining rooms) are turned-off during measurements. Measurements were performed for several cases: free-running fiber lasers , lasers locked to the 1.2 m spiral reference cavities, and lasers locked to the disk resonators of varying diameters (3 mm, 7.5 mm, 15 mm) [107] for comparison with the spiral resonators.

Figure 5.4(a) shows the phase noise spectral density for the heterodyned signals in three cases : the free-running lasers, 3 mm disk resonators, and the 1.2 m spiral cases. In each case, data is shown both with and without the locking systems engaged The spectra are measured at the offset frequencies ranging from 1 Hz to 10 MHz. To show the trend clearly, the measured values are smoothed by limiting fluctuations to 1% of the original values. When the fiber lasers are locked to the 1.2-meter spirals, phase noise is reduced by 26 dB on average. In comparison, only 10 dB suppression was measured at 1 kHz offset frequency in the case of the 3mm diameter disks. Below 1 kHz offset frequency, the 1.2 m spiral case shows even better suppression than the 3 mm disk resonator case. This might be due to the better immunity of the spiral resonators to photo-thermal noise. In the inset of figure 5.4(a), the phase noise noise suppression relative to the free-running fiber laser case is plotted for each resonator case at 1 kHz and 100 Hz offset frequencies. The data indicate that the spiral resonator provides improved suppression of phase noise at lower offset frequency.

Figure 5.4(b) shows the measured electrical spectra of the two fiber laser beatnote in

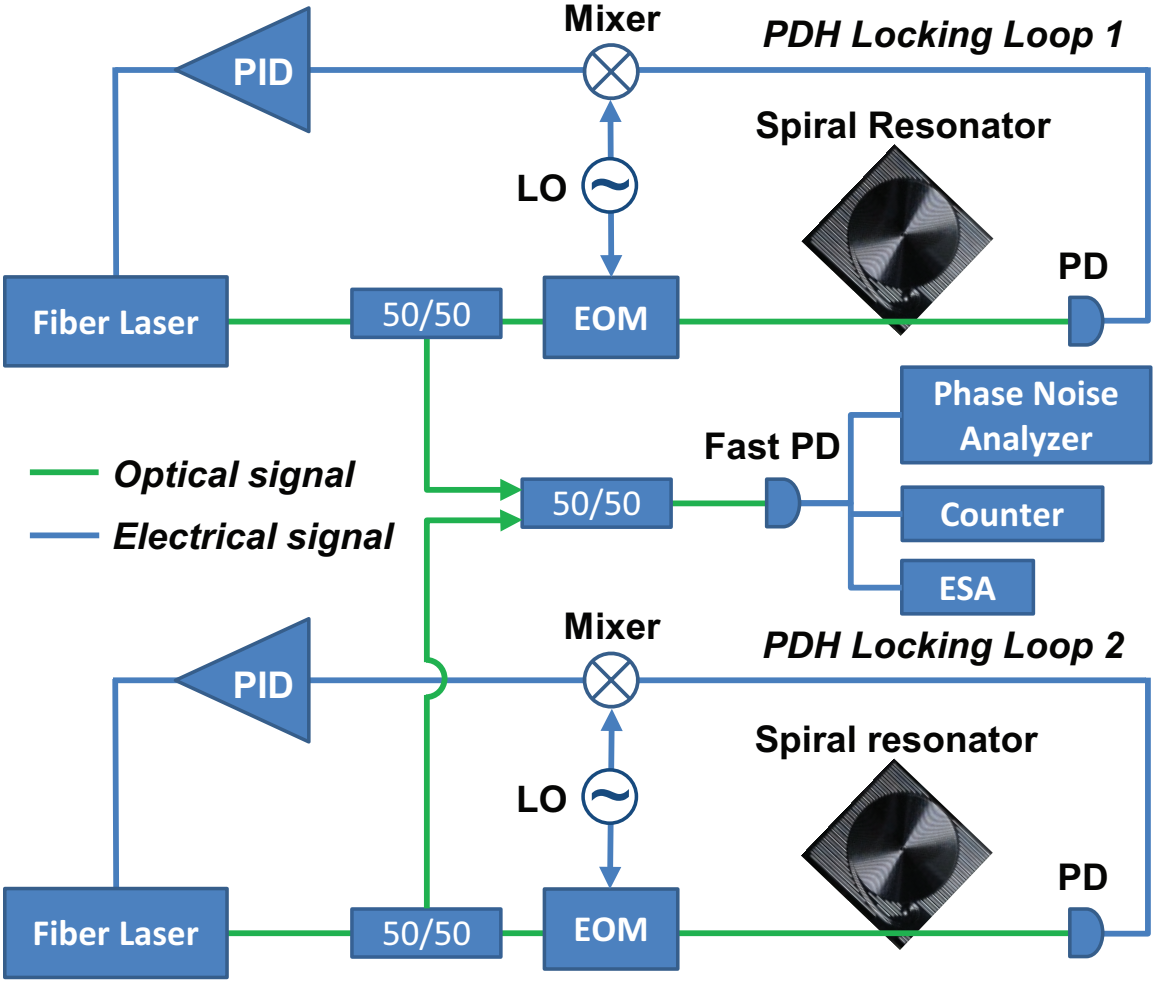

Figure 5.3: **Experimental setup.** Two, fiber lasers independently locked to high-Q spiral reference cavities using a Pound-Drever-Hall locking systems. The outputs of the separately locked lasers were combined on a photodetector and the resulting photocurrent was analyzed using an electrical spectrum analyzer, a frequency counter, and a phase-noise analyzer. All components are on the same optical table.

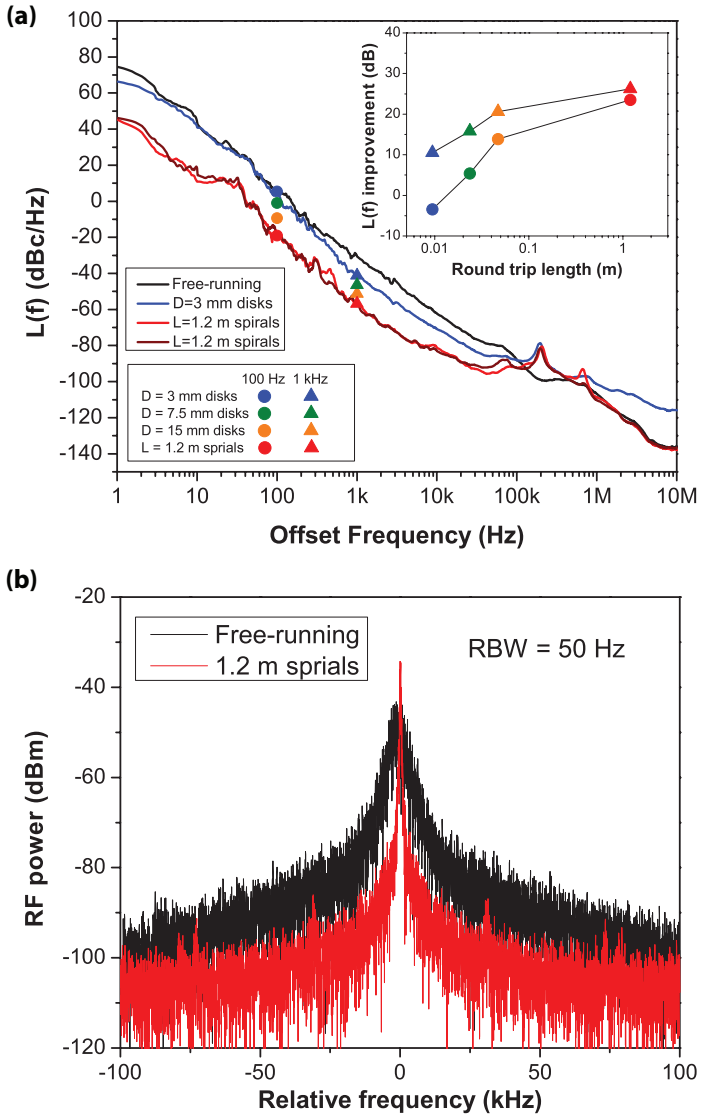

Figure 5.4: **Phase noise spectra and linewidth measurement. a,** Phase noise spectra measured for two, free-running 193 THz fiber lasers (black), fiber lasers independently locked to two, 3-mm disk resonators (blue), and fiber lasers independently locked to two, 1.2-meter long spiral resonators (red and dark red spectra were measured on separate dates). The data for the spiral resonator show an average suppression by 26 dB of the fiber laser noise when locked to the spiral resonators. Moreover, at least 16 dB of noise suppression is observed for the 1.2-meter spirals relative to the 3 mm device. The inset is a plot of the noise suppression at 100 Hz and 1 kHz offset frequencies plotted versus resonator length for each of the resonators tested. **b,** The electrical spectrum of the fiber lasers' beat note for both free running and locked configurations. Spectral narrowing and noise suppression are apparent in the locked spectrum.

the two cases: when the two fiber lasers are free-running and when the lasers are independently locked to the 1.2 m long resonators. The comparison clearly shows the frequency noise suppression and linewidth narrowing with the 1.2 m spiral resonator. The resolution bandwidth (RBW) was set to 50 Hz, resulting 80 ms sweeptime over 200 kHz span. As an additional comparison, the effective linewidth (Δf_L), which is defined as

$$\int_{\Delta f_L}^{\infty} 2L(f)df = 1 \tag{5.2}$$

[128], is calculated for each case from the phase noise spectra of the two laser beatnotes. The calculated linewidths are 900 Hz (free running lasers), 400 Hz (locked to 3 mm disks), and 100 Hz (locked to 1.2 m spiral resonators). Because the phase noise spectra are measured from the beatnote of two lasers, the individual laser linewidths will be narrower than these values.

In order to further confirm the frequency stabilization by the spiral resonators, Zero dead-time Allan deviation measurements [129] are performed using a Tektronix FCA3120 frequency counter and a Pendulum CNT-91 frequency counter. As shown in figure 5.5, Allan deviations of the spiral-locking case are improved over the range of gate times from 5 μs to 3 s, compared to the free-running (unlocked) case. At 400 μs gate time, a minimum relative Allan deviation of 5.5x10^{-13} was measured, and is 10 times lower than that of the free-running case. Assuming the two lasers are independent and have identical frequency fluctuation level, the fractional frequency instability of a single laser is 3.9x10^{-13}, or equivalently 75 Hz.

This level of instability is consistent with the effective linewidth calculated from the phase noise shown in Fig. 5.4(a). The relatively flat profile of the Allan deviation from 0.1-100 ms is also consistent with the $1/f^3$ nature of the phase noise. The small bump in the Allan deviation near 10 ms gate time corresponds to the increased phase noise at 10-100 Hz offset frequency, which is believed to be the environmental noise around the measurement setup. The stability improvement of locked signal at longer gate times is consistent with the phase noise suppression at low offset frequency ($<$10 Hz).

Thermomechanical noises in both the disk and spiral resonators are also measured. The

optomechanical coupling parameter is expected to scale inversely with cavity length so that the phase noise exhibits an inverse quadratic dependence on length [127]. This dependence is observed over a range of cavity lengths by using the Hänsch Couillard technique [130, 131]. Spectral features believed to be thermally-excited mechanical resonances are observed at $>$ 1 MHz offset frequencies, but the amplitude of the noise peaks steadily diminished to levels below the sensitivity limit of the system for 1.2 m spiral resonator case. In the measured phase noise spectra, there is no evidence of mechanical noise.

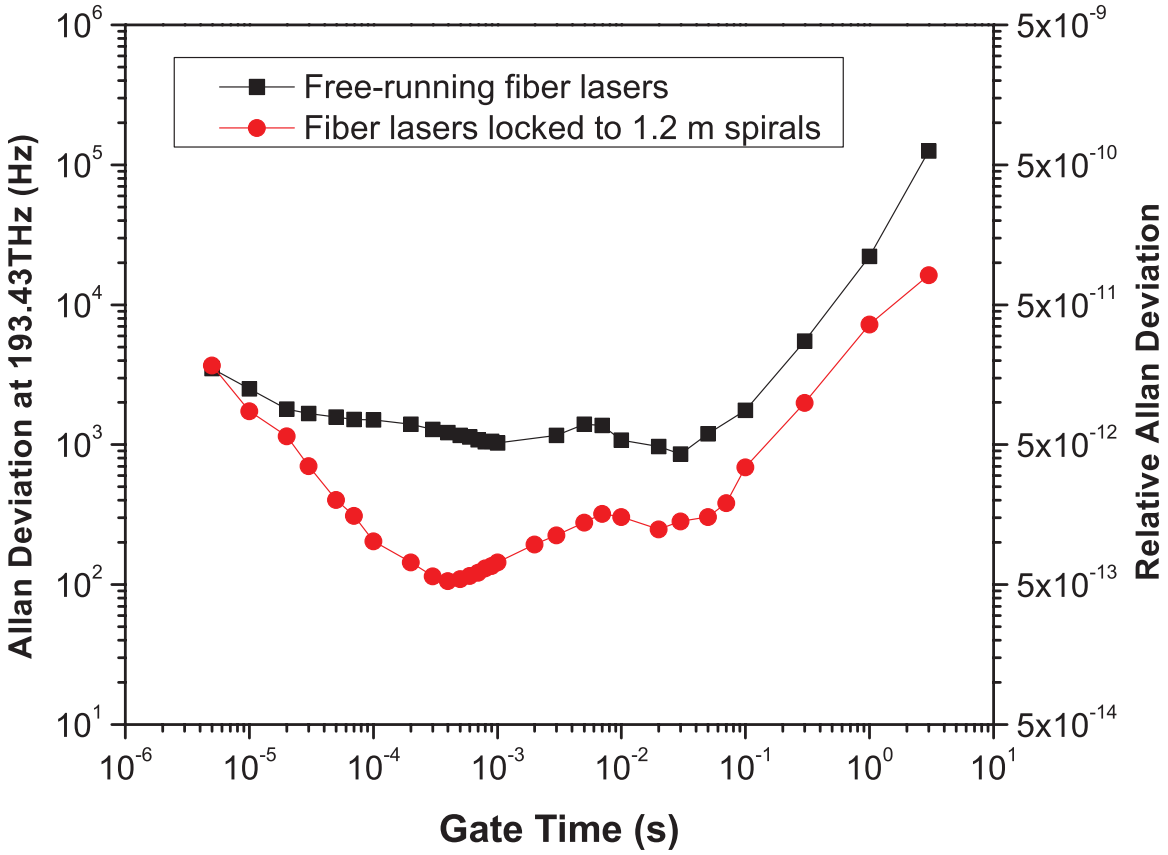

Figure 5.5: **Allan deviation measurement result.** Allan deviation of the beat frequency between the two, free-running fiber lasers (black squares), and for the lasers independently locked to two, 1.2-meter long spiral resonators (red circles) is shown. A minimum Allan deviation of 100 Hz at an optical frequency of 193 THz, corresponding to a relative Allan deviation of 5.5 x 10^{-13}, was measured at a gate time of 400 μs. 10 dB improvement in the minimum Allan deviation compared to the free-running case is achieved. Assuming the fiber lasers are independent and equivalent, an Allan deviation of 75 Hz is expected for each laser.

5.4 Theoretical Noise Limit of Spiral Reference Cavity

In this section, the theoretical thermorefractive noise of the spiral reference cavity is studied and the fiber lasers are stabilized to the theoretical limit through further technical noise reduction. The improved stability shows the relative Allan deviation of 2.85×10^{-13} at 500 μs averaging time and the linewidth of 55 Hz.

Figure 5.6(a) shows a silica spiral resonator used in this work. The free-spectral range(FSR) is $\sim$ 167 MHz and the optical quality factor is typically $\sim$ 100 million. Laser light is coupled into the resonator at the upper corner of the chip via evanescent coupling method using fiber taper[2, 3] . To make the optical coupling stable and reduce the acoustic noise, the taper-fiber-coupled spiral resonators are fixed on a metallic sample mount using UV-curable epoxy and packaged into portable brass boxes with FC/APC connectors. (Figure 5.6(b))

Frequency stability of the spiral resonators is measured using the experimental setup shown in Fig. 5.6(c). Two fiber lasers (Orbits Lightwave, 193.43 THz) are independently locked to two high-Q silica spiral resonators with Pound-Drever-Hall systems [91]. Optical power coupled to the spiral resonators is about 1 mW. The entire setup sits on the active vibration cancellation system and acoustic shielding was placed around the entire setup to attenuate environmental sound. No active temperature stabilization or vacuum isolation is used here. The locked fiber lasers are heterodyned to produce a beat signal near 60 MHz and this beat note directly reveals the combined frequency instability of the two stabilized lasers. The beat note is analyzed using an electrical spectrum analyzer, a phase noise analyzer (Rohde & Schwarz FSUP26), and a frequency counter (Tektronix FCA3120). Measurements were performed for two cases: free-running fiber lasers and stabilized fiber lasers locked to the 1.2 m spiral resonators. Figure 5.7(a) shows the electrical spectra of the two cases with 200 kHz span and 50 Hz resolution bandwidth(RBW). The linewidth of laser beatnote has narrowed significantly when the lasers are locked to the spiral resonators.

Figure 5.7(b) shows the phase noise spectra of the heterodyned signals both free-running and stabilized lasers. The spectra were measured over the offset frequencies ranging from 1 Hz to 10 MHz. When locked to the spiral resonators, the phase noise is improved within the

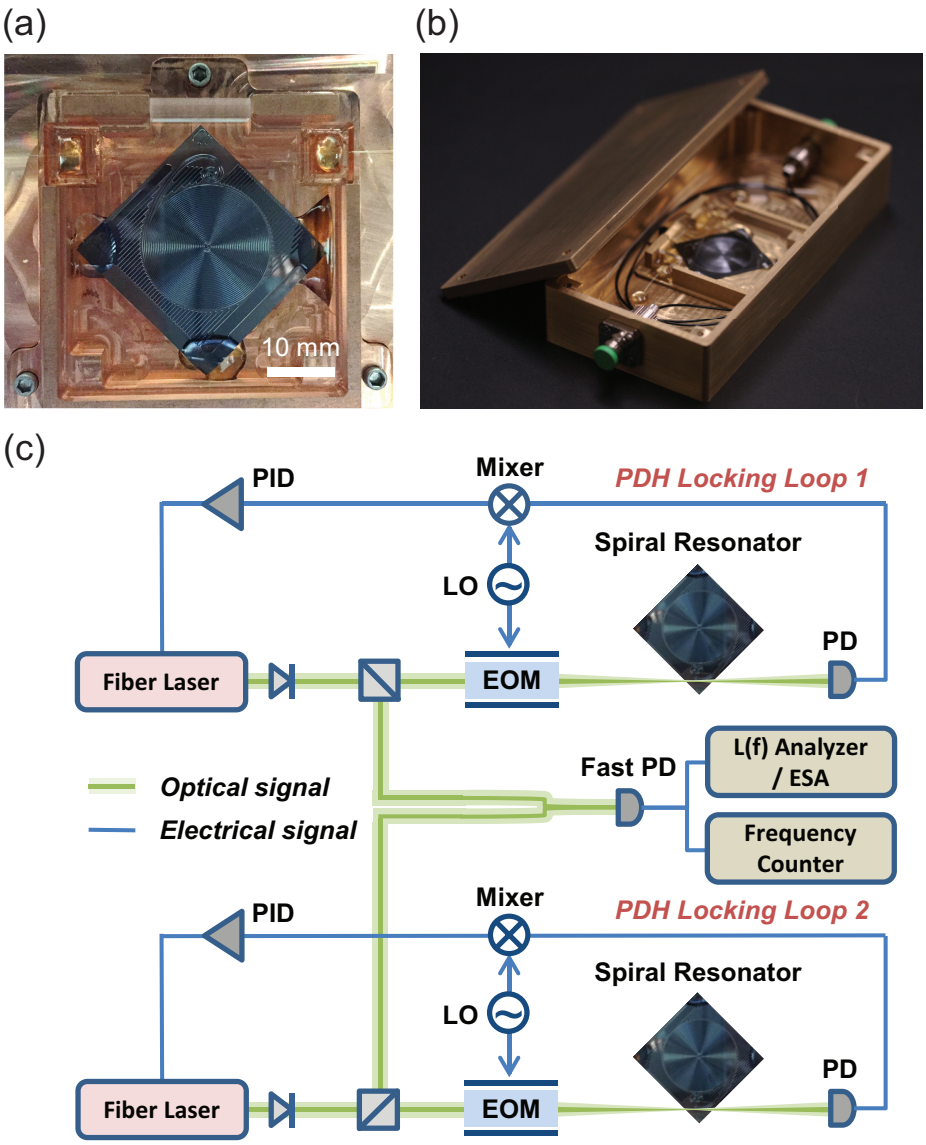

Figure 5.6: **Packaged silica spiral resonator and experimental setup for laser frequency stabilization.** (a) Silica spiral resonator on silicon chip with an optical roundtrip length 1.2 meter and footprint less than 1 inch x 1 inch. Using UV-curable epoxy, the silicon chip and fiber taper are fixed on a metallic sample mount, maintaining the optical coupling. (b) Packaged spiral resonator with fiber-pigtailed FC/APC connectors. (c) Measurement setup : two fiber lasers independently locked to high-Q spiral resonators using Pound-Drever-Hall(PDH) locking systems. The outputs of the stabilized lasers were combined on a photodetector(PD) and the resulting photocurrent was analyzed using an electrical spectrum analyzer(ESA), a phase-noise(L(f)) analyzer, and a frequency counter. All components are on the same optical table with active vibration cancellation, and acoustic shielding is placed around the measurement setup. PID : Proportional-Integral-Derivative servo controller, EOM : Electro-Optic Modulator, LO : Local Oscillator.

200 kHz bandwidth of the servo-control loop. Specifically below 1 kHz offset frequency, an average suppression by 30 dB of the fiber laser noise is measured. From the phase noise spectra, the effective linewidth(Δf_L), which is defined in eq. (5.2), is calculated for each case. The beatnote of the two stabilized fiber lasers using 1.2 meter spiral resonators shows the effective linewidth of $\sim$ 80Hz, which is an order of magnitude improved value from $\sim$ 890 Hz of the free-running case.

To analyze the measured phase noise theoretically, the power spectral density of thermal fluctuations in rotationally symmetric structures[132, 133], such as microspheres and microdisks, is revisited. Specifically, the one-sided thermorefractive frequency noise $S_{\delta f}(f)$ in a thin microdisk with radius R and thickness L at temperature T and offset frequency f has the form

$$\begin{aligned} S_{\delta f}^{disk}(R,f) =& f_0^2 \alpha_n^2 \frac{k_B T^2 \nu^{2/3}}{6\kappa L} \\ & \times \left[1 + \left(\frac{2\pi R^2 |f|}{9\sqrt{3} D} \right)^{3/2} + \frac{1}{6} \left(\frac{\pi R^2 |f|}{4\nu^{1/3} D} \right)^2 \right]^{-1}, \end{aligned} \tag{5.3}$$

where $D = \kappa/(\rho C)$, κ is the thermal conductivity coefficient, ρ is the material density of the microdisk, and C is the specific heat capacity. α_n is the thermorefractive coefficient of the material and f_0 is the laser frequency. The azimuthal quantum number of the optical mode $\nu \simeq 2\pi R n/\lambda$ [133], where n is the refractive index of silica and λ is the laser wavelength. For simplicity, the wedge angle of the microdisk is assumed to be 90 degree instead of 30 degree in the real structure.

In case of spiral resonators, there is no azimuthal symmetry and the radius, i.e. the distance from the spiral center, varies as the spiral turns. In lack of azimuthal symmetry, the heat conduction also has azimuthal components. The azimuthal heat transferring rate J_θ is approximately related to the radial heat transferring rate J_R by

$$J_\theta = \frac{1}{\rho} \frac{\partial \rho}{\partial \theta} J_R. \tag{5.4}$$

Because the radius of the spiral is slowly varying, satisfying the condition that $\frac{1}{R}\frac{\partial R}{\partial \theta} \ll 1$, the azimuthal heat transferring is a minor effect compared with the radial heat transferring.

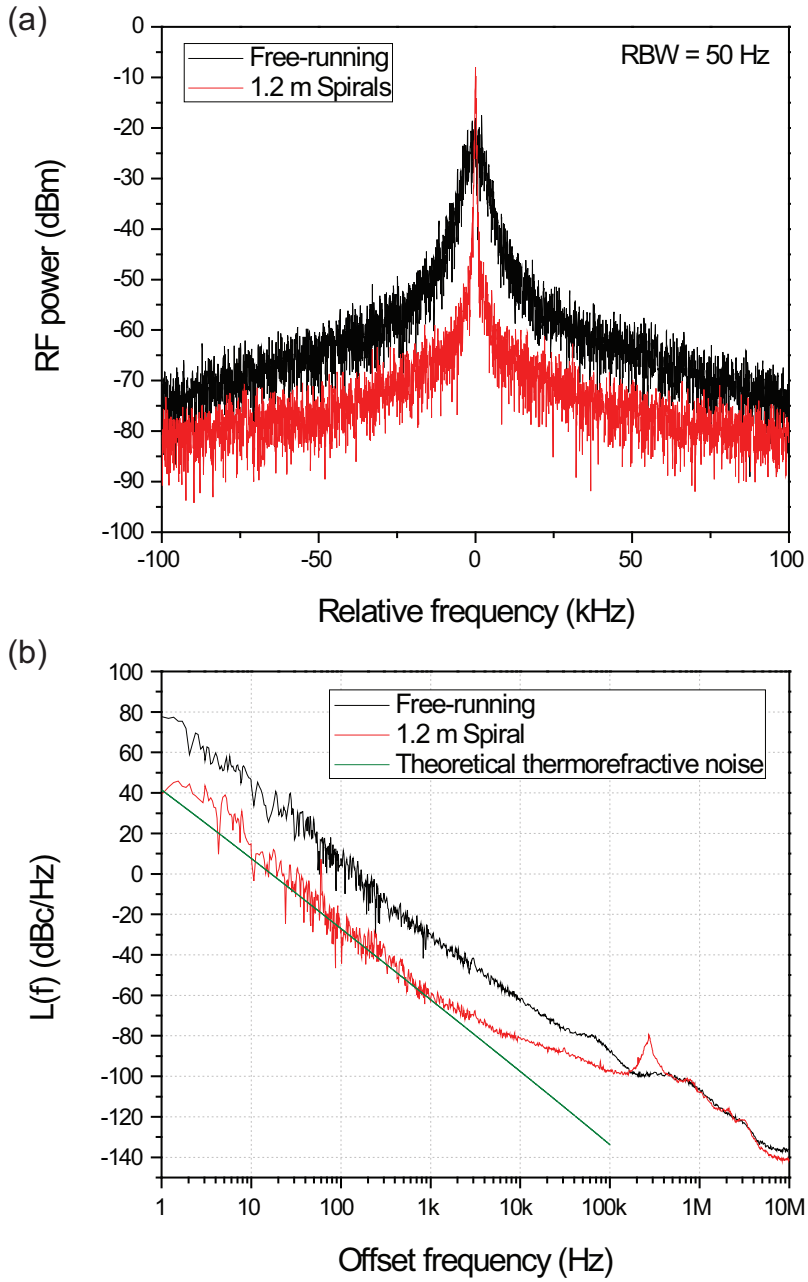

Figure 5.7: **Electrical spectra and phase noise spectra of the frequency-stabilized fiber lasers.** (a) The electrical spectrum of the fiber lasers' beat note for free-running(black) 193 THz fiber lasers and stabilized lasers(red) locked to 1.2-meter spiral resonators. Spectral narrowing and noise suppression are apparent in the stabilized spectrum. Resolution bandwidth(RBW) is 50 Hz. (b) Phase noise spectra measured for free-running lasers (black) and the stabilized lasers(red). The data show an average suppression by 30 dB of the fiber laser noise when locked to the spiral resonators. The theoretical thermorefractive noise (green) of the spiral resonator is also plotted and shows a good agreement with the measured phase noise.

This indicates that the spiral is azimuthally adiabatic. Thus $S_{\delta f}^{spiral}(f)$, the spectral density of thermorefractive frequency noise in the spiral, can be deduced from that of disk by

$$S_{\delta f}^{spiral}(f) = \int S_{\delta f}^{disk}(R(\theta), f)(\frac{R(\theta)}{\overline{R}})^2 \frac{\mathrm{d}\theta}{2\pi}, \tag{5.5}$$

where $\overline{R} = \int R(\theta)\mathrm{d}\theta/2\pi$. The theoretical thermorefractive noise of 1.2 m spiral resonator is calculated and $2L(f) = [1/f^2]S_{\delta f}^{spiral}(f)$ is plotted in green (Figure 5.7(b)). Here, the factor of two is multiplied to the theoretical noise to compare with the experimental noise which is measured from the beatnote of uncorrelated two signals. The theoretical thermorefractive noise shows good agreement with the measured phase noise. Here, we use L = 8 μm, $T = 300K$, $D = \kappa/(\rho C) = 9.5 \times 10^-7$. ρ = 2.65 g/cm^2 , $\kappa = 10 \times 10^5\ erg/(cm \cdot s \cdot K)$, $C = 7.41 \times 10^6\ erg/(g \cdot K)$, $\alpha_n = -6 \times 10^{-6} K^{-1}$, f_0 = 193.43 THz and n = 1.444. In the calculation, the smallest radius of the spiral is 800 μm and the gap between the successive turnings is 290 μm.

As an additional confirmation of the frequency stabilization by the spiral resonators, Allan deviations [134] were measured using a Tektronix FCA3120 frequency counter (Figure 5.8). Over the range of gate times from 5 μs to 3 s, Allan deviations of the spiral-locking case were improved compared to the free-running case. At a gate time of 500 μs, a minimum relative Allan deviation of 4.0×10^{-13} was measured, which is 10 times lower than that of the free-running case. If the two lasers are assumed to be independent, then the instability of a single laser is 2.85×10^{-13}, or equivalently 55 Hz. Moreover, the stability improvement of locked signal at longer gate times is consistent with the phase noise suppression at low offset frequency (< 10 Hz) and shows the enhanced immunity of the resonator to photo-thermal noise. Here, no linear drift correction was performed on the data.

By the ideal frequency division of the 193 THz optical carrier to 10 MHz, the demonstrated frequency instability level of 2.85×10^{-13} would provide a signal with close-to-carrier phase noise of approximately $-100/f^3$ dBc/Hz. This is a level that is already competitive with the state-of-the-art oven-controlled crystal oscillators (OCXO), and the basic architecture to accomplish this has been demonstrated with the combination of laboratory

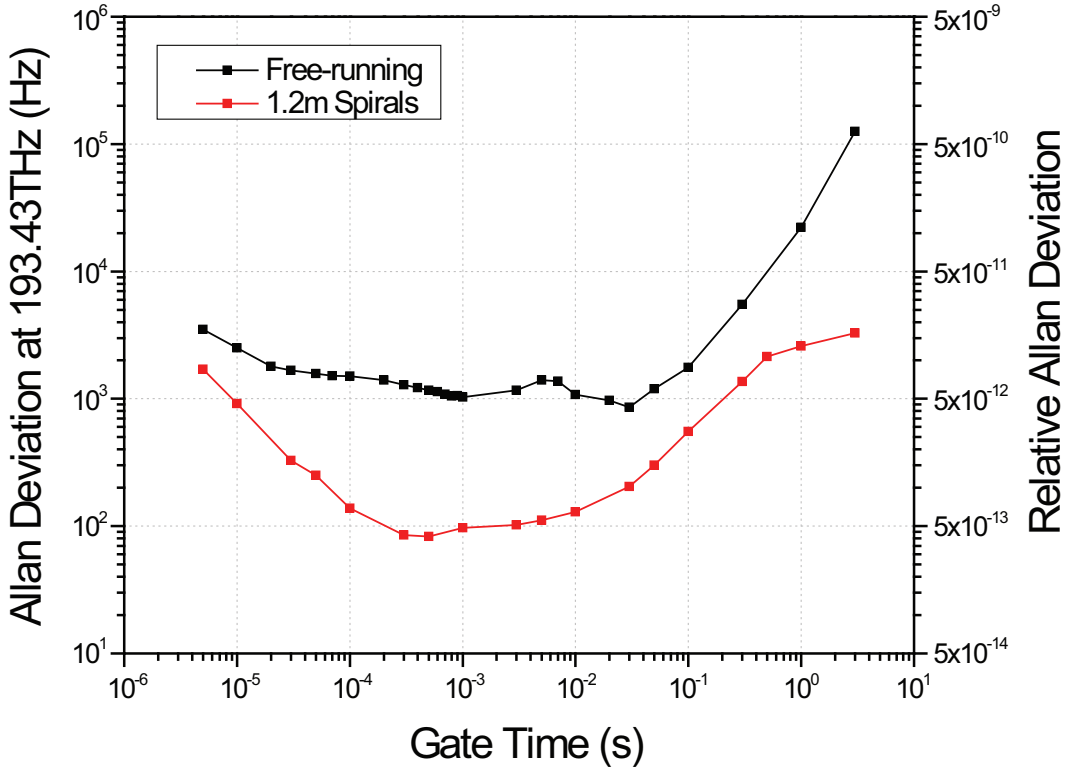

Figure 5.8: Allan deviations of the beat frequencies in two cases are shown: two free-running fiber lasers (black squares) and two stabilized lasers independently locked to two, 1.2-meter long spiral resonators (red circles). A minimum Allan deviation of 78 Hz at an optical frequency of 193.43 THz, corresponding to a relative Allan deviation of 4.0×10^{-13}, was measured at a gate time of 500 μs. 10 dB improvement in the minimum Allan deviation compared to the free-running case is achieved. Assuming the fiber lasers are independent and equivalent, an Allan deviation of 55 Hz is expected for each laser.

frequency combs and electronic division [135]. The current stability can be improved further by making the spiral resonator with longer optical roundtrip length and thicker silica layer, which will result larger optical mode volume. The density of device (roundtrip length per unit area) can be also enhanced by adopting silica ridge structure. SiN-waveguide integrated structure is also possible[89] and it allows the spiral resonator to be integrated with other chip-based optical components. Particularly, this on-chip frequency reference can be combined with microcomb technology[39, 40, 41] to provide broad-bandwidth synthesis of low-phase-noise signals from RF to optical domain. In addition, the high optical coherence from on-chip reference cavity can enhance the performance of many chip-based systems in the field of communication[136], remote sensing [137], atomic physics [94, 138], and spectroscopy[85]. Its scalable and integrable nature combined with the performance reported here makes the spiral resonator an appealing on-chip reference cavity for portable optical devices.

5.5 Low-Noise Microwave Generation via Optical Frequency Division

Low-noise microwave generation using optical signals has been studied for decades in systems including optical delay-line oscillators, dual-mode lasers[139, 140, 141, 142, 143, 144] and optical parametric oscillators. Among many microwave photonics technologies, optical frequency division (OFD) has revolutionized the generation of stable microwave signals[92, 145], which potentially benefit time keeping[146, 147, 148], communications[149], and radar[137, 150]. Using a self-referenced frequency comb as an optical divider, this approach is applied to transfer the fractional frequency instability of optical frequency reference down to microwave domain and generate the state-of-art low-noise microwave signal with the fractional frequency instability of $< 8 \times 10^{-16}$ at 1 s of averaging [92]. Alternatively, two optical frequencies with good relative stability are used as a stable THz frequency reference for low-noise microwave generation via OFD [145, 151, 152].

While the approach using two optical references (or 2-point lock OFD) provides the

same theoretical limit with the approach using one optical reference (or 1-point lock OFD), 2-point lock OFD is suitable for portable systems because the common noise cancellation gives immunity to external vibration/acoustic noise and it does not need the complex self-referencing of frequency comb[145]. An electro-optical method is also demonstrated for the 2-point lock OFD. In this method, optical frequency combs are generated through a cascade of direct phase modulation and self-phase modulation of the two optical frequencies by using a voltage controlled electrical oscillator[152]. This electro-optical frequency division (EOFD) method is simple relative to other comb generation methods. It is also tunable and scalable to higher division ratios within the tunable range of the voltage controlled oscillator and the phase modulator.

In this section, stable microwave is generated from two laser lines locked to the on-chip spiral reference cavity via EOFD method.

Figure 5.9(a-b) illustrates the measurement setup. Two fiber lasers with two different frequencies were combined by a bi-directional coupler and evanescently coupled to the spiral resonator via tapered fiber. The spiral resonator has the round-trip length of 1.2 meter, equivalent to the free-spectral-range of 167 MHz. The typical quality factor of the device is $50 \sim 100$ million. The coupled optical power is approximately 3 mW for each laser. The two fiber lasers are independently locked to the optical modes of the spiral resonator using Pound-Drever-Hall system (Figure 5.9(a)).

Then, the two frequency-stabilized lasers are tapped and combined through 50/50 fiber-coupler. The combined laser lights are introduced into the electro-optical frequency divider[153] as shown in figure 5.9(b), which generates frequency combs around the two stabilized laser frequencies with the spectral line spacing set by the voltage-controlled electrical oscillator(VCO). Optical spectra of the two frequency-stabilized laser lines and cascaded sidebands are recorded using Yokogawa AQ6370D optical spectrum analyzer (OSA). The overlapping comblines at the midpoint are optically filtered and photodetected. The detected beatnote signal is phase-locked to the ~ 10 MHz offset frequency from an oven-controlled crystal oscillator (OCXO) by a feedback control. The phase noise spectrum and electrical spectrum of the phase-locked VCO signal are measured using Rohde Schwartz FSUP26. Fractional frequency instability is also measured using the Tektronix FCA3120 frequency

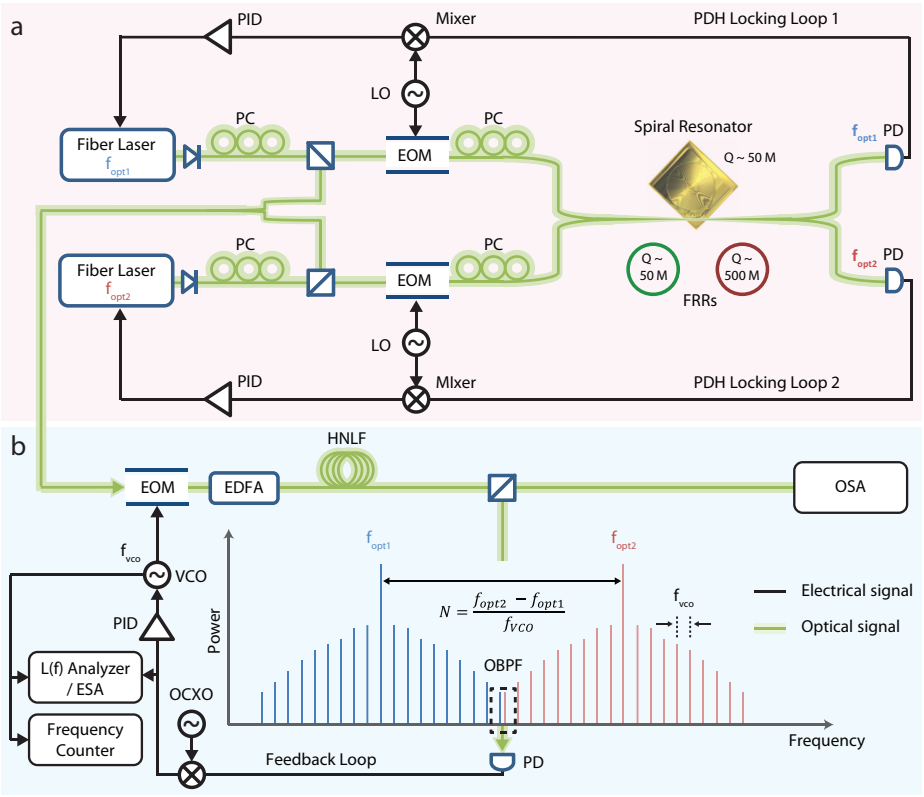

Figure 5.9: **Experimental setup for optical frequency division using a spiral reference cavity.** (a) Setup for generation of relatively stable two laser lines locked to the spiral resonator. Two fiber lasers with two different frequencies (f_{opt1} and f_{opt2}) were combined and evanescently coupled to the spiral resonator via tapered fiber. The polarization controllers (PC) are used to change the polarization of lasers. The two fiber lasers are independently phase-locked to the optical modes of the spiral resonator using Pound-Drever-Hall (PDH) feedback loop. Instead of the spiral resonator, two fiber ring resonators (FRRs) with different quality(Q)-factors (50 million and 500 million) are also used. Then, the two frequency-stabilized lasers are tapped and combined through a 50/50 fiber-coupler. (b) A schematic of the electro-optical frequency divider to generate a microwave signal. The combined two stabilized laser lines are introduced to the electro-optic modulator (EOM) and phase modulated to generate cascaded sidebands around each laser line. The frequency spacing between the sidebands are determined by the frequency of voltage controlled oscillator (VCO). The cascaded sidebands are spectrally broadened to generate two overlapping combs after passing erbium-doped fiber amplifier (EDFA) and highly nonlinear fiber (HNLF). The two overlapping combines at the mid point are optically filtered and photodetected to generate $\sim$ 10 MHz beat frequency. The beat frequency is phase-locked to the oven-controlled crystal oscillator (OCXO) via feedback loop. The phase noise spectra, L(f), and RF power spectra of the two combline beat frequency and the VCO frequency(f_{VCO}) are measured using phase noise analyzer / electrical spectrum analyzer (ESA). Fractional frequency instability of the VCO frequency is also measured using a frequency counter. The optical spectrum is measured using an optical spectrum analyzer (OSA). PD : Photo Detector, LO : Local Oscillator, PID : Proportional - Integral - Derivative controller.

counter.

As a first step, the reference phase noise before frequency division is studied by measuring the phase noise of 167 MHz beatnote from two stabilized fiber lasers near 1550 nm which are locked to two adjacent modes of same mode-family in the spiral resonator (Figure 5.10). Within the 200 kHz current modulation bandwidth of the fiber lasers, the phase noise (red curve) has improved significantly and 15 dBc/Hz is measured at 1 Hz offset frequency, which is more than 60 dB lower than the phase noise measured from the two free-running fiber lasers (black curve). The theoretical thermo-refractive noise of the 1.2-meter spiral resonator at 167 MHz carrier frequency,

$$L_{167\text{ MHz}}(f) = \left[\frac{167\text{ MHz}}{193.5\text{ THz}}\right]^2 \times L_{193.5\text{ THz}}(f), \tag{5.6}$$

is also plotted (cyan dashed line). Here, $L_{193.5\text{ THz}}(f)$ is the theoretical one-sided phase noise of the spiral resonator at 193.5 THz optical carrier frequency, which sets the fundamental noise limit of the spiral resonator and is already derived in section 5.4. The measured phase noise is much higher than the theoretical thermo-refractive noise limit and this discrepancy originates from low signal-to-noise of frequency discriminator signal in the PDH feedback loop, which results in not enough servo gain to suppress the intrinsic laser noise[154]. To confirm this, we repeated the same phase noise measurement using 2-meter-long fiber ring resonators (FRRs) with two different Q-factors, 50 million (green curve) and 500 million (blue curve), having the same free-spectral range (FSR) of 100 MHz. While the FRR with Q $\sim$ 50 million shows similar phase noise level with the spiral resonator, the FRR with Q $\sim$ 500 million shows $\sim$ 20 dB lower phase noise. This confirms that the measured phase noise of the spiral resonator is limited by the low signal-to-noise in the PDH feedback loop and can be further improved by increasing the Q-factor of the spiral resonator.

As a next step, two fiber lasers at 1549.9 nm and 1564.6 nm are phase-locked to the spiral resonator and two relatively stable optical frequencies having 1.817 THz difference frequency are generated. As shown in figure 5.11(a), frequency combs (cascaded sidebands of the two stable optical lines) are created through electro-optic modulation and spectrally

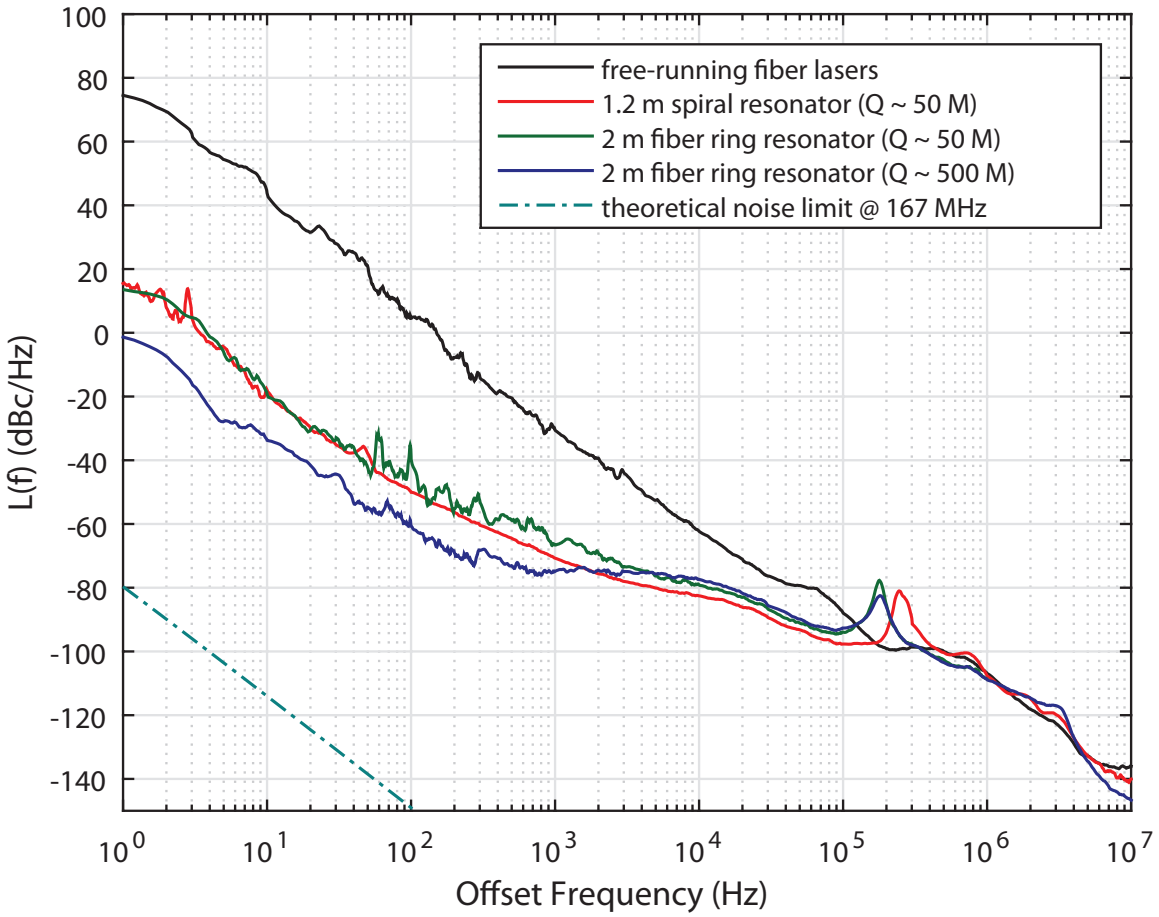

Figure 5.10: **Phase noise spectra of the heterodyned two fiber lasers near 1550 nm.** One-sided phase noise spectra of the beatnotes from two free-running fiber lasers (black curve) and two fiber lasers phase-locked to the 1.2 m spiral resonator (red curve). The beat frequency is 167 MHz, which is the free spectral range (FSR) of the spiral resonator, and the frequencies of two fiber lasers are around 1550 nm. The phase noise is reduced within the 200 kHz current modulation bandwidth of fiber lasers and the reduction factors are 60 dB below 100 Hz and 40 dB at 1 kHz offset frequency. The improved phase noise is 100 dB higher than the theoretical thermorefractive noise (cyan dashed line) at 167 MHz carrier frequency and limited by the low signal-to-noise in the Pound-Drever-Hall (PDH) feedback loop. The phase noise spectra measured from two fiber ring resonators with different quality factors, 50 million (green curve) and 500 million (blue curve), show that the phase noise can be further reduced by improving the quality factor of the spiral resonator.

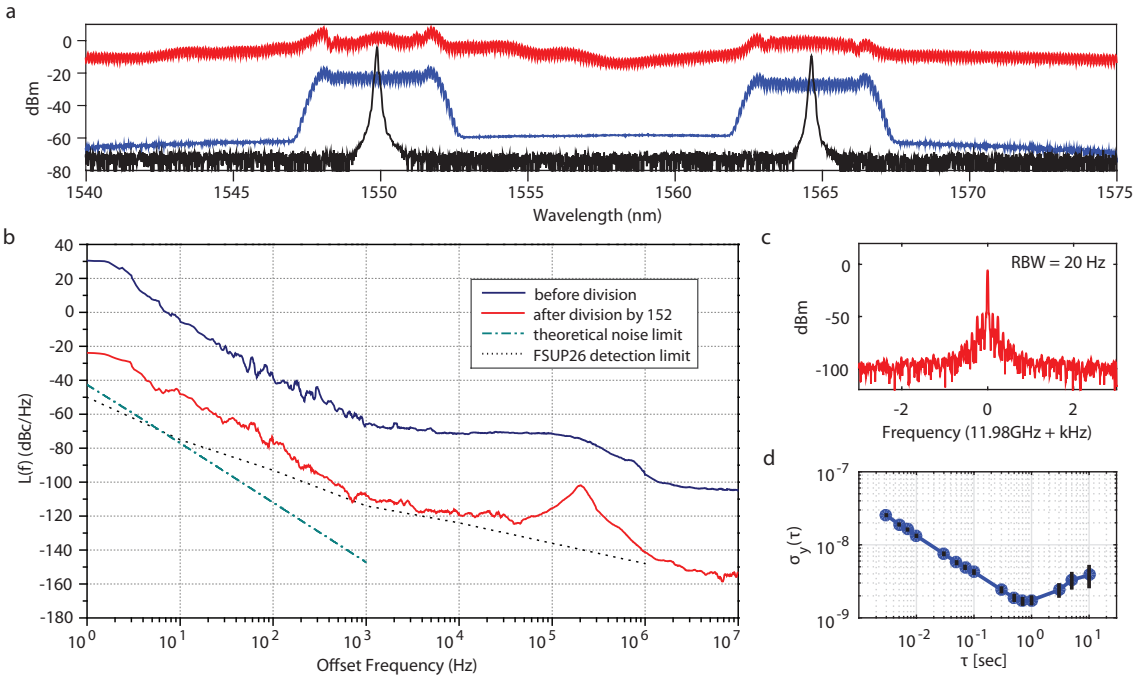

Figure 5.11: **Stable microwave generation via optical frequency division.** (a) Optical spectra of two pump lasers (black), narrow combs around pump lasers after the cascaded phase modulation (blue) and overlapped combs after spectral broadening (red). The two pump laser lines are 1.817 THz apart and the frequency of the voltage controlled oscillator (VCO) is 11.97 GHz. (b) One-sided phase noise spectra measured before and after optical frequency division (OFD) are shown. Before frequency division, phase noise is measured from 9.5 MHz beat frequency of the optically filtered comblines at the overlapped region (blue curve). After frequency division, phase noise is measured from the phase-locked VCO signal at 11.97 GHz (red curve). Average phase noise reduction is $\sim$44dB which is the division factor (1.817 THz / 11.97 GHz = 152) squared . The theoretical thermorefractive noise at 11.97 GHz carrier frequency (cyan dashed line) and the detection limit of the phase noise analyzer, Rohde Schwarz FSUP26,(black dotted line) are also shown. (c) Electrical power spectrum of the phase-locked VCO signal within 6 kHz span. Resolution bandwidth (RBW) is 20 Hz. (d) Fractional frequency instability, $\sigma_y(\tau)$, over the averaging time (τ) from 3 ms to 10 s.

broadened to overlap at the mid point. The overlapping comblines are filtered by using a fiber-bragg-grating optical filter and the phase noise spectrum of $\sim$ 10 MHz beat frequency is measured as a reference phase noise level before frequency division (blue curve in figure 5.11(b)). The reference phase noise spectrum includes the phase noise of VCO (Agilent PSG microwave synthesizer) magnified by optical division factor (1.817 THz / 11.97 GHz = 152) in addition to the phase noise of 1.817 THz beatnote. Above 1 kHz offset frequency, the phase noise is limited by the magnified VCO noise.

After electro-optical frequency division by phase-locking the two combline beat frequency to OCXO offset frequency ($\sim$ 10 MHz), the phase noise spectrum of the phase-locked VCO frequency ($\sim$ 11.97 GHz) is measured (red curve in figure 5.11(b)). On average, it has improved from the reference level by 44 dB, which is the division factor squared ($152 \times 152 = 23104 \sim 44$ dB). However, it is $>$ 30dB higher than the theoretical thermorefractive noise (cyan dashed line in figure 5.11(b)). Again, it is limited by the unsuppressed intrinsic laser noise due to the low signal-to-noise in the PDH feedback loop. The servo-conrol bump is also shown near 200 kHz, limiting the phase noise around the offset frequency.

Figure 5.11(c) shows the electrical power spectrum of the stabilized 11.97 GHz VCO signal within 6 kHz span. The resolution bandwidth is 20 Hz. Fractional frequency instabilities are also measured at the averaging times from 3 ms to 10 s, and minimum of 1.68×10^{-9} is measured at 0.7 s (Figure 5.11(d)). It's worth noting that there's no vacuum system or temperature stabilization to achieve this value. Although the measured stability is limited by the technical noise of the PDH feedback loop, the theoretical noise limit can be reached by enhancing the Q-factor of the spiral resonator. Current Q-factor is limited by the surface scattering loss of the spiral resonator and can be improved by the optimization of device fabrication process. Alternative way to achieve the theoretical limit is increasing the division factor using two laser lines with a larger frequency difference. Ideally, 30-fold improvement of the quality factor (from 50 million to 1.5 billion) or the division factor (from 1.817 THz to 60 THz) will be needed to reach the theoretical limit and this will reduce the fractional frequency instability by 15 dB.

Furthermore, we can also reduce the theoretical thermorefractive noise limit by making

the spiral resonator with larger optical mode volume, which can be made possible by longer optical roundtrip length and thicker silica layer. This will improve the fractional frequency stability further. Potentially, silica ridge structure can increase the mode volume per unit silicon chip area an order of magnitude larger and also enable the integration with other chip-based optical components[89]. Combined with emerging microcomb technology[39, 40, 41], our work shows the potential of an optical frequency division system on a chip for the next generation of portable microwave sources.

Chapter 6

Stimulated Brillouin Laser from Optical Microresonator

Stimulated Brillouin scattering (SBS) in high-Q microresonators enables the generation of narrow-linewidth laser and low-phase-noise microwave. The linewidth of the stimulated Brillouin laser(SBL) is known to be Schawlow-Townes-like, limited by the thermal phonon occupancy(n_T). In this chapter, we study the n_T-limited nature of the SBL linewidth at cryogenic temperatures. Our work confirms the SBL linewidth theory prediction and provides support for the unusual quantum limit of linewidth in these laser systems. In addition, a microresonator SBL-based gyroscope is demonstrated as one of the SBL applications.

6.1 Introduction

As briefly introduced in chapter 1, stimulated Brillouin Scattering (SBS) is a third-order (χ^3) optical nonlinearity that results from the interaction between photons and acoustic phonons in a medium [4, 5, 6, 7]. Recently, the SBS process has attracted considerable interest in micro and nanoscale devices [11]. Brillouin laser action has been demonstrated in several microcavity systems including silica resonators [12, 1, 13, 14] and CaF_2 resonators [15]. Brillouin amplification has also been observed in integrated Chalcogenide waveguides [16], and confinement-enhanced amplification has been realized in silicon waveguides [17]. SBS also provides a powerful tool for integrated photonics signal processing [18, 19, 20], and it has been applied to realize a chip-based optical gyroscope [155]. Moreover, at radio-frequency rates, the SBS damping rate is low enough in certain systems

to enable cavity optomechanical effects [21] including optomechanical cooling [22] and optomechanical-induced transparency [23].

Laser linewidth is of central importance in spectroscopy, frequency metrology and all applications of lasers requiring high coherence. It is also of fundamental importance, because the Schalow-Townes laser linewidth limit is of quantum origin. Recently, a theory of stimulated Brillouin laser (SBL) linewidth has been reported. While the SBL linewidth formula exhibits power and optical Q factor dependences that are identical to the Schawlow-Townes formula, a source of noise not present in two-level lasers, phonon occupancy of the Brillouin mechanical mode, is predicted to be the dominant SBL linewidth contribution. Moreover, the quantum-limit of the SBL linewidth is predicted to contain a contribution from the zero-point motion of the phonons. The formula for SBL linewidth in Hertz (full-width half maximum) [13] and the conventional laser Schawlow-Townes linewidth (2-level laser system) [156] are given below,

$$\Delta\nu_{SBS} = \frac{\hbar\omega^3}{4\pi P Q_T Q_E}(n_T + N_T + 1), \tag{6.1}$$

$$\Delta\nu_{2-Level} = \frac{\hbar\omega^3}{4\pi P Q_T Q_E}(N_T + \frac{1}{2}), \tag{6.2}$$

where n_T is the number of thermal quanta in the mechanical field at the Brillouin shift frequency, N_T is the number of thermal quanta in the Stokes optical field (negligible at optical frequencies and henceforth ignored), P is the SBL output power, Q_T (Q_E) is the total (external) Q-factor, and ω is the laser frequency. Eq. (6.1) is valid when the Brillouin gain bandwidth is much broader than the optical cavity linewidth. Besides the appearance of n_T, eq. (6.1) contains a "1" versus "1/2", resulting from zero-point contributions to the SBL linewidth of both photons and phonons (i.e, "1 = 1/2 + 1/2"). Of greater significance at finite temperatures is n_T, which for microwave-rate phonons (10.8 GHz in the current work) provides the dominant contribution to the SBL linewidth [13]. In the next section, the phonon contribution to eq. (6.1) is verified by determination of n_T over a wide range of temperatures using eq. (6.1) followed by comparison to the Bose-Einstein phonon occupancy at these temperatures.

6.2 The Phonon-Limited-Linewidth of Brillouin Lasers at Cryogenic Temperatures

To confirm the theory of SBL fundamental linewidth, SBL linewidth is measured at cryogenic temperatures in a silica microresonator. Its temperature dependence and the SBL linewidth theory are combined to predict the number of thermo-mechanical quanta at three temperatures: room temperature, liquid nitrogen temperature and liquid helium temperature.

Figure 6.1(a) shows the experimental setup. After passing through an optical circulator, the pump laser (Newport TBL 6700) passes into the cryostat via an optical fiber vacuum feedthrough. Inside the cryostat, the pump laser is evanescently coupled to a silica disk microresonator via a fiber taper that is positioned piezoelectrically using XYZ-attocube system (Figure 6.1(b)). Pumping power to the resonator was around 20 mW. The silica microresonator, shown in Figure 6.1(c), is a wedge design [1]. The resonator diameter was approximately 6 mm to match the Brillouin gain shift frequency and the free-spectral range (FSR) at cryogenic temperatures. Optimization of the diameter was needed to efficiently generate SBL within the pump laser tuning range (1520 nm - 1570 nm). The cryostat is an open-loop continuous-flow unit made by Janis and was cooled to 77 K using liquid nitrogen and to 8 K using liquid helium. Figure 6.2 shows the cryostat used in this work. In the inset, a silica disk microresonator having 6 mm diameter and tapered fiber are shown.

Brillouin laser action proceeds as shown in figure 6.1(d) where cascaded stimulated Brillouin lasing is illustrated. Pump laser coupled to a resonator mode induces Brillouin gain over a narrow band of frequencies shown in green (typically 20 - 60 MHz wide) that are down-shifted by the Brillouin gain shift frequency $\Omega/2\pi = 2nV_s/\lambda_P$ where V_s is the sound velocity, n is the refractive index and λ_P is the pumping wavelength [13]. When the cavity FSR approximately equals Ω, stimulated Brillouin lasing is possible and creates a 1^{st} Stokes laser wave. This 1^{st} Stokes wave propagates backward relative to the pump wave on account of the phase matching (momentum conservation) condition, and comes out of the cryostat at the fiber input (figure 6.1(a)). If the pump power is increased further, the 1^{st} Stokes laser wave will grow in power and ultimately induce laser action on a 2^{nd}

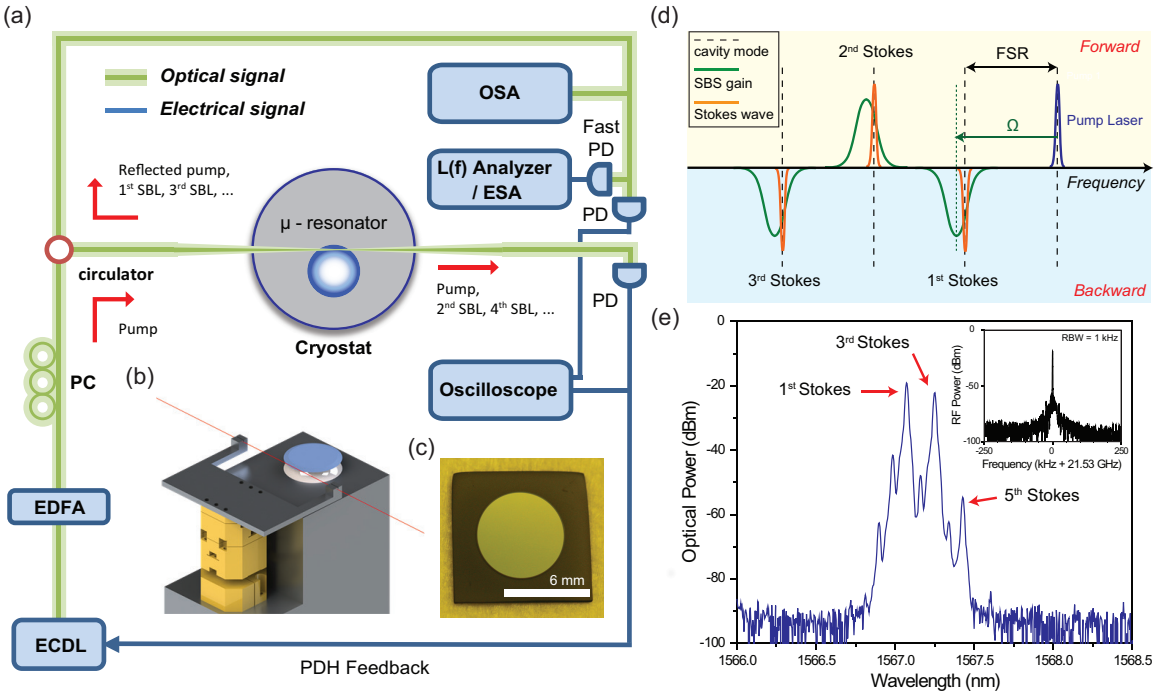

Figure 6.1: **Experimental setup and Brillouin laser action** (a) Experimental setup showing external cavity diode laser (ECDL) pump, erbium-doped fiber amplifier (EDFA), polarization control (PC) and ciculator coupling to the cryostat. Green lines indicate optical fiber. A fiber taper is used to couple to the microresonator. Pump and even-ordered stimulated Brillouin laser (SBL) waves propagate in the forward direction while odd-ordered SBL waves propagate in the backward direction and are coupled using the circulator. Photodetectors (PD) and an oscillopscope monitor the waves propagating in both directions. A fast photodetector measures the 1^{st}/ 3^{rd} beatnote which is measured using an electrical spectrum analyzer (ESA) and phase noise (L(f)) analyzer. An optical spectrum analyzer (OSA) also measures the backward propagating waves. The pump laser is locked to the microresonator optical resonance using a Pound-Drever-Hall (PDH) feedback loop. (b) Schematic of the optical fiber taper coupling setup inside the cryostat. Optical fiber (red) is glued to an aluminum holder which is fixed on a 3-axis piezoelectric stage. The microresonator is mounted on a copper plate. (c) Top view of the 6 mm wedge disk resonator. (d) Illustration of cascaded Brillouin laser action. Pump and even Stokes orders propagate in the forward direction while odd orders propagate in the backward direction. Green peaks represent the Brillouin gain spectrum. Brillouin shift frequency (Ω) and free-spectral-range (FSR) are indicated. (e) Optical spectrum measured using the OSA and showing cascaded Brillouin laser action to 5th order. Inset: typical electrical beatnote spectrum produced by the 1^{st} and 3^{rd} order Stokes laser signals.

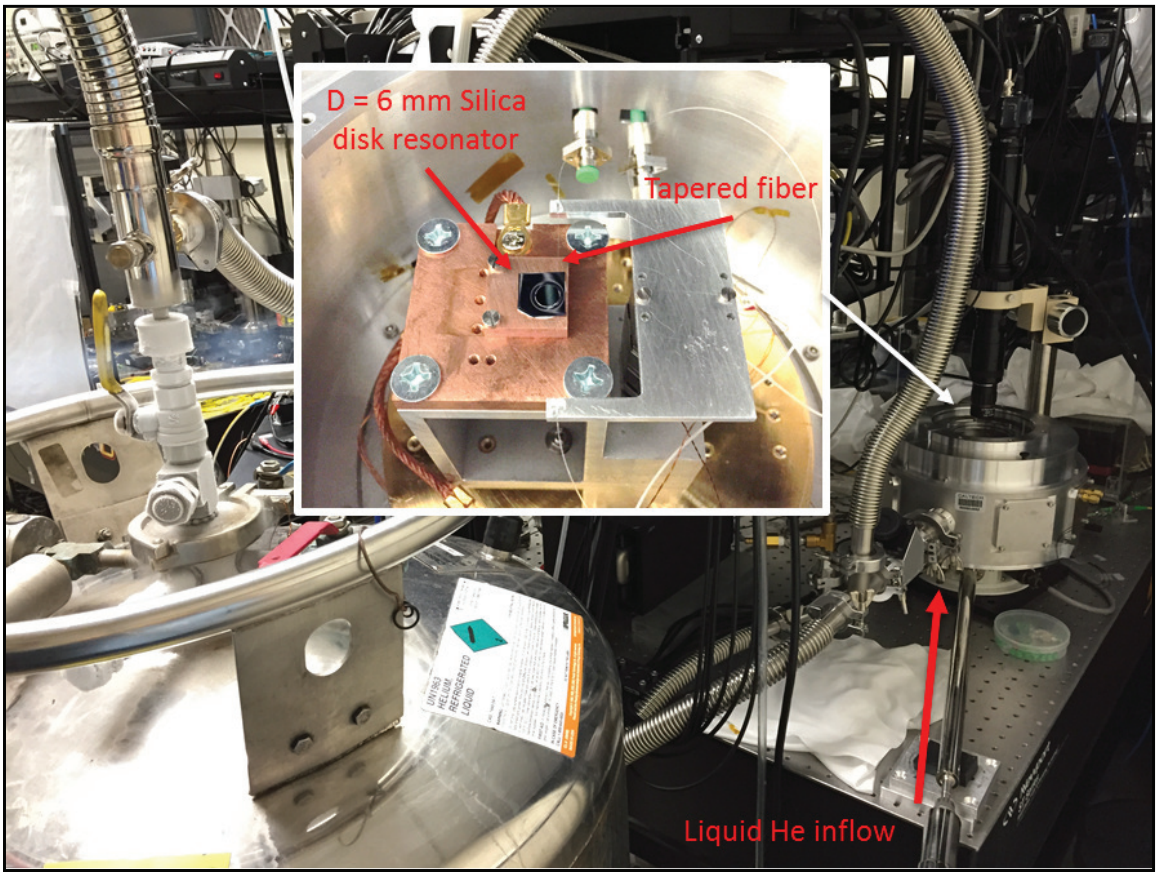

Figure 6.2: **Picture of the cryostat** The open-loop continuous-flow cryostat system used in this work. Liquid helium container, transfer line and inlet are also shown (for the measurement at 8 K). Liquid helium is replaced to liquid nitrogen for the measurement at 77 K. In the inset, a silica disk microresonator having 6 mm diameter and the tapered fiber coupling setup are shown.

Stokes laser wave, which propagates in the forward direction. This cascaded SBL process is illustrated in figure 6.1(d) to 3$^{\mathrm{rd}}$ order. Phase matching ensures that odd (even) orders propagate backward (forward), and follow fiber-optic paths in figure 6.1(a) to measurement instruments. Figure 6.1(e) is a spectrum of cascaded SBL to 5$^{\mathrm{th}}$ order measured using the OSA in figure 6.1(a). Odd orders appear stronger than the even orders (and the pump signal) because the OSA is arranged to detect odd orders. Weak even-order signals are also detected because of back-scattering in the optical system.

The SBL cascade obeys a system of rate equations relating the circulating photon number, p_n, of the nth Stokes laser wave to the circulating photon number, p_{n-1}, of its preceding (n-1)st pump wave [13].

$$\dot{p}_n = g_n p_{n-1} p_n - \frac{\omega_n}{Q_T} p_n, \tag{6.3}$$

where

$$g_n = \hbar \omega_n v_g^2 \Gamma \frac{g_B}{V_{eff}} \approx \hbar \omega_n v_g \Gamma \frac{\Omega}{2\pi} \left(\frac{g_B}{A_{eff}} \right) \tag{6.4}$$

is the Brillouin gain coefficient for the n$^{\mathrm{th}}$-Stokes laser wave in Hertz units. Here, ω_n is the optical frequency of the n$^{\mathrm{th}}$ Stokes wave, v_g is the group velocity of the the n$^{\mathrm{th}}$-Stokes laser wave, Γ is the phonon-photon mode overlap factor (defined as the optical mode area (A_{eff}) divided by the acousto-optic effective mode area [157]), g_B is the bulk Brillouin gain coefficient of silica, and V_{eff} is the effective optical mode volume of the n$^{\mathrm{th}}$-Stokes laser wave. g_B/A_{eff} is the normalized Brillouin gain coefficient in $W^{-1}m^{-1}$ unit that is typically measured in optical fibers.

The gain coefficient, g_n, has the spectral profile of the Brillouin gain spectrum (i.e., green curves in figure 6.1(d)). Steady state solution of eq. (6.3) shows that p_{n-1} is clamped when the nth Stokes wave starts to grow. This clamping is the typical gain clamping accompanying lasing threshold in many other laser systems. As the pump power increases, a Stokes wave will be initiated and increase in power until it clamps when the threshold condition for the next Stokes wave in the cascade is reached. This clamped power, P_{clamp},

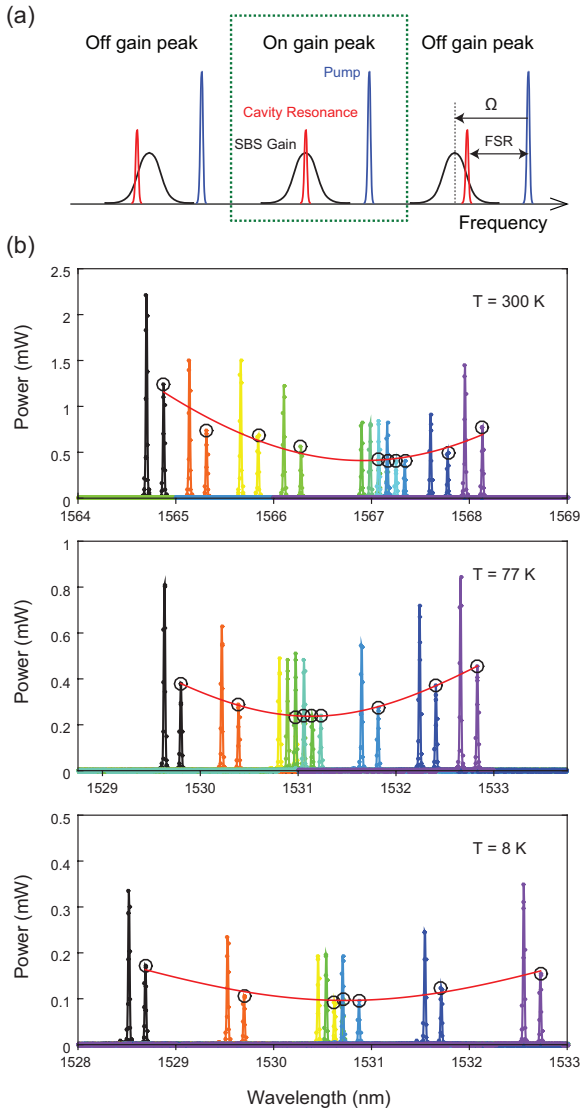

Figure 6.3: **Aligning the 3rd Stokes wave to the Brillouin gain spectrum maximum** (a) Illustration showing spectral placement of Stokes wave with respect to Brillouin gain spectrum maximum. Variation of the pumping wavelength causes the Brillouin shift frequency (Ω) to vary and thereby scans the Stokes wave across the Brillouin gain peak. (b) Measured spectra of P_{clamp}, the 3rd-order Stokes wave power (indicated by the black circle in the plots). The three panels show measurements performed at T = 300 K, 77 K and 8 K. Each color corresponds to a distinct pumping wavelength. The 1^{st}-order Stokes wave also appears in the spectral map as the stronger peak near the 3rd-order Stokes wave. The pump wave is not observable in the linear-scale spectrum as it propagates in the direction opposite to the 1^{st}-order and 3rd-order Stokes waves. $P_{\text{clamp}}^{\text{min}}$ is determined from the fitted red curve as the minimum power point (with corresponding pumping wavelength).

follows directly from the steady-state form of eq. (6.3),

$$P_{clamp} = \frac{\omega_{n-1}}{Q_E}\hbar\omega_{n-1}p_{n-1} \approx \frac{1}{g}\frac{\hbar\omega_n^3}{Q_T Q_E}, \tag{6.5}$$

where the approximation results from letting $\omega_{n-1} \approx \omega_n$ and where the index, n, of the Stokes order is suppressed. At this clamped power, the fundamental linewidth of the Stokes laser follows by substitution of eq. (6.5) into eq. (6.1),

$$\Delta\nu_{clamp} = \frac{g}{4\pi}(n_T + 1). \tag{6.6}$$

It is useful to note that the SBL linewidth in the clamped condition is independent of Q_T and Q_E. Moreover, eq. (6.6) is now applied with measurement of g and $\Delta\nu_{clamp}$ to determine n_T.

From eq. (6.5), measurement of P_{clamp}, Q_T and Q_E are sufficient to determine g. However, g also depends on the placement of the Stokes wave within the Brillouin gain spectrum (see green spectral curve in figure 6.1(d)). To eliminate this ambiguity, measurements were performed at the spectral maximum of g defined as g_0. Because operation at the spectral maximum of g causes P_{clamp} to be minimized (defined as P_{clamp}^{min}), it is possible to identify the spectral maximum of g by measuring P_{clamp} at several different pumping wavelengths. Tuning the pumping wavelength causes the Brillouin shift frequency Ω to also tune, and to vary the spectral location of the Stokes wave within the Brillouin gain band (see figure 6.3(a)). When the Stokes wave is spectrally aligned to the maximum value of g, P_{clamp} will be minimum and the maximum g can be obtained at the pumping wavelength.

In figure 6.3(b), optical spectra showing multiple measurements of clamped power for the 3$^{\mathrm{rd}}$ Stokes wave at different pumping wavelengths are presented. The three panels show spectra at T= 300, 77, and 8 K. The spectral peak of 3$^{\mathrm{rd}}$ Stokes wave at each pumping wavelength is identified by a black circle. Minimum clamped power and corresponding pumping wavelength is found at each temperature. At this pumping wavelength $g = g_0$ (center case in green box in figure 6.3(a)). As an aside, the power clamping condition for the 3$^{\mathrm{rd}}$ Stokes wave was determined by monitoring the onset of laser action in the 4$^{\mathrm{th}}$ Stokes

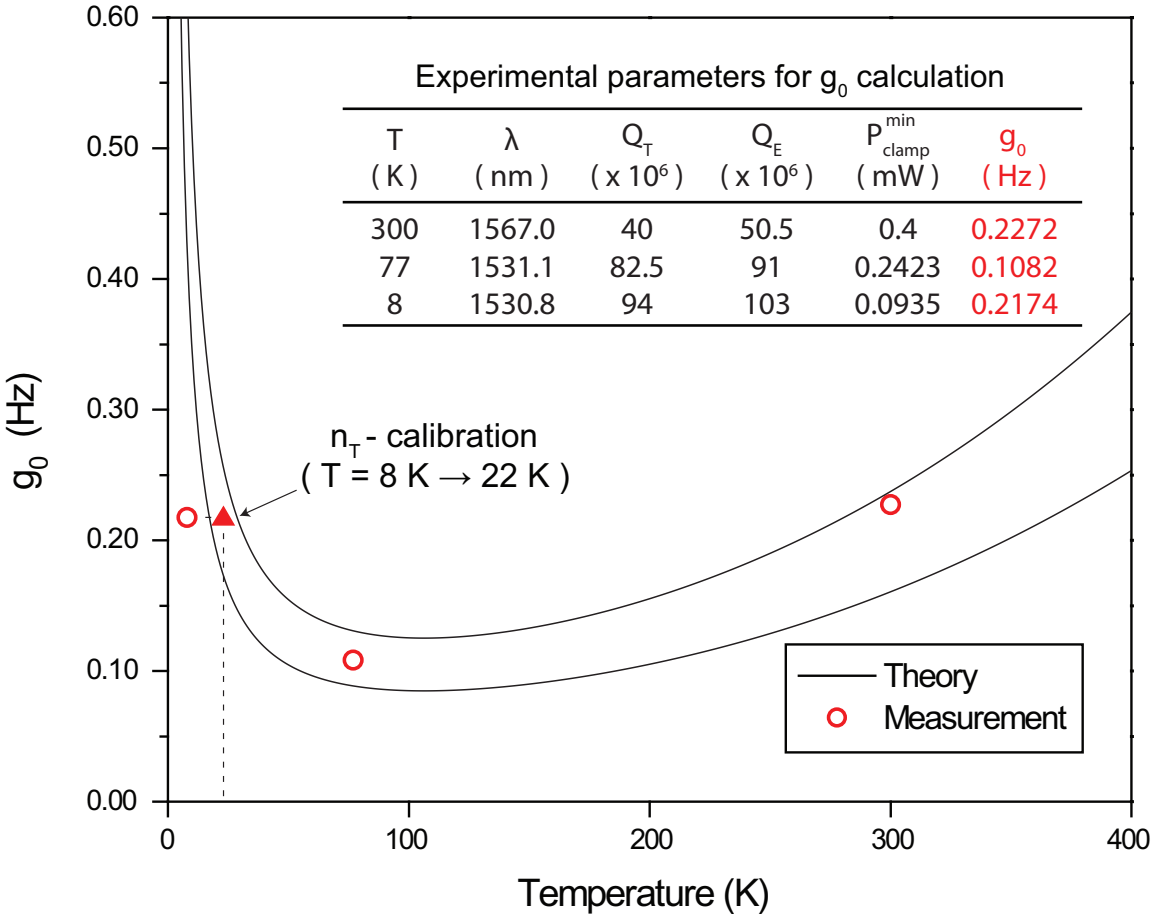

Figure 6.4: Brillouin gain coefficient (g_0) calculated from values in the table (red circle). The area between the two black solid curves is the theoretical g_0 range converted from the temperature-dependent theoretical Brillouin gain of the silica optical fiber [158]. Inset: table of the experimental parameters for g_0 calculation. Temperature (T), pumping wavelength (λ), total (Q_T) and external (Q_E) Q-factors, minimum clamped power (P^{min}_{clamp}), and the corresponding calculated Brillouin gain coefficient.

wave. Also, optical losses between the resonator and the OSA were calibrated to determine the clamped power. The table in figure 6.4 summarizes the measured minimum clamped powers, P_{clamp}^{min}, and their corresponding pumping wavelengths. Q_T and Q_E, determined by fitting both the linewidth and the transmission minimum of the Stokes mode, are also given. Finally, g_0, calculated using eq. (6.5), is compiled in the table. Brillouin gain bandwidth, $\Delta\nu_B$, can be also extracted from a quadratic fit of the curves in figure 6.3(b) [13], and is 20 MHz at 300 K, 25 MHz at 77 K, and 35 MHz at 8 K.

The experimentally determined g_0 is plotted versus temperature in figure 6.4. Two theory curves are given for comparison and were determined from a study of phonon damping in silica [158] in the following way. The measured $\Delta\nu_B$ at 300 K and 77 K are used to determine the material/geometry-induced error range of $\Delta\nu_B$ curve ($\Delta\nu_B$ at 8 K is not used because even a small error in measured temperature can result in a significant error in $\Delta\nu_B$). Assuming $g_B \times \Delta\nu_B$ = 1.67×10^{-3} Hz $\cdot$ m/W where the constant depends on the material properties of silica [158] and A_{eff} = 85 μm^2 in the silica optical fiber, the normalized Brillouin gain coefficient g_B/A_{eff} curve is obtained and converted in Hz unit using eq 6.4. In the calculation, $\hbar\omega = 1.27 \times 10^{-19}$ J, $v_g = 2.078 \times 10^8$ m/s, and Γ = 0.85 is used.

To measure the Stoke linewidth, the beatnote of 1$^{\text{st}}$ and 3$^{\text{rd}}$ Stokes lasers is detected using a fast photodetector and characterized using an electrical spectrum analyzer (inset in figure 6.1(e)) and a phase noise analyzer. The phase noise of this beatnote provides spectral components associated with the fundamental phase noise of the Stokes lasers. Moreover, fundamental phase noise in the beatnote is dominated by the 3$^{\text{rd}}$ Stokes laser because the 1$^{\text{st}}$ Stokes laser has higher power than the 3$^{\text{rd}}$ Stokes laser (see figure 6.3(b)) the fundamental linewidth of the 1$^{\text{st}}$ Stokes laser is narrower. Because the two Stokes lasers are generated within a same microresonator, common technical frequency noise was reduced in this measurement.

To measure the fundamental linewidth of the 3$^{\text{rd}}$ Stokes wave, the phase noise of 1$^{\text{st}}$/3$^{\text{rd}}$-order SBL beatnote is measured at the P_{clamp}^{min} wavelength determined in figure 6.3(b). A Rhode-Schwarz FSUP26 phase noise analyzer was used for the analysis. The phase noise spectra at 300 K, 77 K, and 8 K are measuring using the Rhode-Schwarz FSUP26 phase

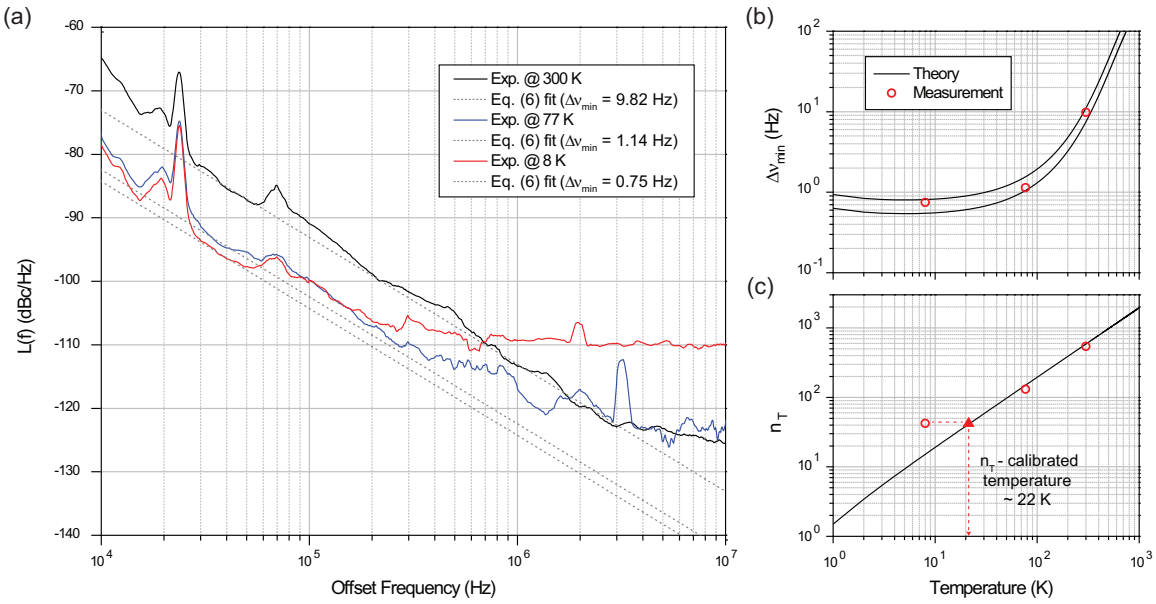

Figure 6.5: (a) Phase noise spectra of the 1st/3rd-order SBL beatnotes at three temperatures (300 K, 77 K, 8 K). The eq. (6.7) fit at each temperature is the black dotted line. (b) Red points: minimum SLB linewidth resulting from fitting in panel (a) using eq. (6.7). Theoretical prediction (area between two solid black curves) combines theory for g_0 with Bose-Einstein occupancy in eq. (6.7). (c) Thermal phonon occupancies (n_T) calculated from the measured phase noise and Brillouin gain density peak value (g_0) are shown as red circles. n_T from the Bose-Einstein occupancy is given as the black line. Triangular point: n_T-based temperature calibration to 22 K using Bose-Einstein.

noise analyzer and shown in figure 6.5(a). The theoretical phase noise spectrum for an SBL limited by fundamental noise is given by the expression,

$$L(\nu) = \frac{\Delta\nu_{min}}{2\nu^2} = \frac{g_0}{8\pi\nu^2}(n_T + 1), \tag{6.7}$$

where $\Delta\nu_{min}$ is the fundamental linewidth given by eq. (6.6) with $g = g_0$ and the second equality uses eq. (6.6). The black dashed lines in figure 6.5(a) give minimum fits to the measured phase noise spectra using eq. (6.7). The corresponding $\Delta\nu_{min}$ is plotted in figure 6.5(b). Even with the common-mode noise suppression noted above, there is considerable technical noise coupling to the spectrum from the cryogenic system and fitting is not possible over the entire spectral range. Nonetheless, using g_0 from the figure 6.4 table and $\Delta\nu_{min}$ from figure 6.5(b) in eq. (6.7) provides reasonable values for n_T at the three temperatures. In figure 6.5(c), these inferred n_T values are plotted versus temperature in comparison to the Bose Einstein thermal occupancy. The discrepancy between the lowest temperature n_T value and the Bose-Einstein value could result from parasitic optical heating due to high pump power or temperature difference between the temperature sensor and the resonator. If the value of n_T is assumed to provide an accurate indication of the mode volume temperature, then a corrected temperature is 22 K (triangular point). This temperature value is also the triangular point in figure 6.4 and provides improved agreement between theory and the measurement of g_0 versus temperature.

In conclusion, stimulated Brillouin lasers are peculiar in that their fundamental linewidth is predicted to be limited by thermo-mechanical quanta of the Brillouin mode. We have confirmed this theoretical prediction by determining the thermal phonon occupancy versus temperature using the SBL phase noise and Brillouin gain g_0. Measurements at 300 K, 77 K and 8 K are in good agreement with the expected Bose-Einstein occupancy. Our result shows a possible way to reduce the SBL linewidth for precision measurements and supports the theoretical prediction that the quantum-limited linewidth of an SBL laser is strongly influenced by the phonon zero-point motion.

6.3 Application of Chip-based Stimulated Brillouin Laser : Microresonator Brillouin Gyroscope

Rotation sensors (gyroscopes) are widely used in commercial and military systems and there has been intense interest in compact, lightweight sensors that can be integrated with electronics for many applications such as consumer electronics and miniature satellites. Among various rotation sensors, MEMS based sensors have compact / lightweight features and are widely used in consumer electronics. However, MEMS-based gyroscopes do not provide sensitivity and bias stability that compete with optics-based gyroscopes such as ring-laser gyros [159] and fiber-optic gyros [160]. Moreover, MEMS-based devices are typically vulnerable to shock and vibration [161] due to the suspended structure. Therefore, micro-fabricated optics-based gyroscopes are appealing in that they can be environmentally robust and perform better than MEMS-based gyroscopes.

In this section, micro-optical gyro is demonstrated using counter-propagating Brillouin lasers in a chip-based optical resonator. The microresonator Brillouin gyroscopes measure rotation as a Sagnac-induced frequency shift [155]. Previously, a Brillouin laser ring gyro (BLRG) has been studied in the 1990s using an optical fiber resonator [162]. In the BLRG system, a fiber ring resonator is bi-directionally pumped to generate two Brillouin lasers propagating in opposite direction [162]. If the fiber ring resonator rotates, these counter-propagating Brillouin lasers experience opposing frequency shifts caused by the Sagnac effect [163], and detection of the two laser beatnote allows one to measure the rotation rate. In contrast to BLRG, our work uses a high-Q chip-based disk microresonator that is 18mm in diameter to generate Brillouin lasers[1]. Also, instead of bi-directional pumping, cascaded stimulated Brillouin lasers excited from a single pump laser are used[13].

A detailed schematic of our experimental setup is shown in figure 6.6(b). The upper panel contains the gyro sensing unit, which at its core includes the high-Q disk microresonator and fast photodetector. The pump laser is evanescently coupled to the high-Q microresonator using a tapered-fiber and is locked to the cavity resonance using the Pound-Drever-Hall technique. The free-spectral-range (FSR) of the resonator is designed to precisely match an integer fraction of the Brillouin shift (1/3 in the present case) and the cavity

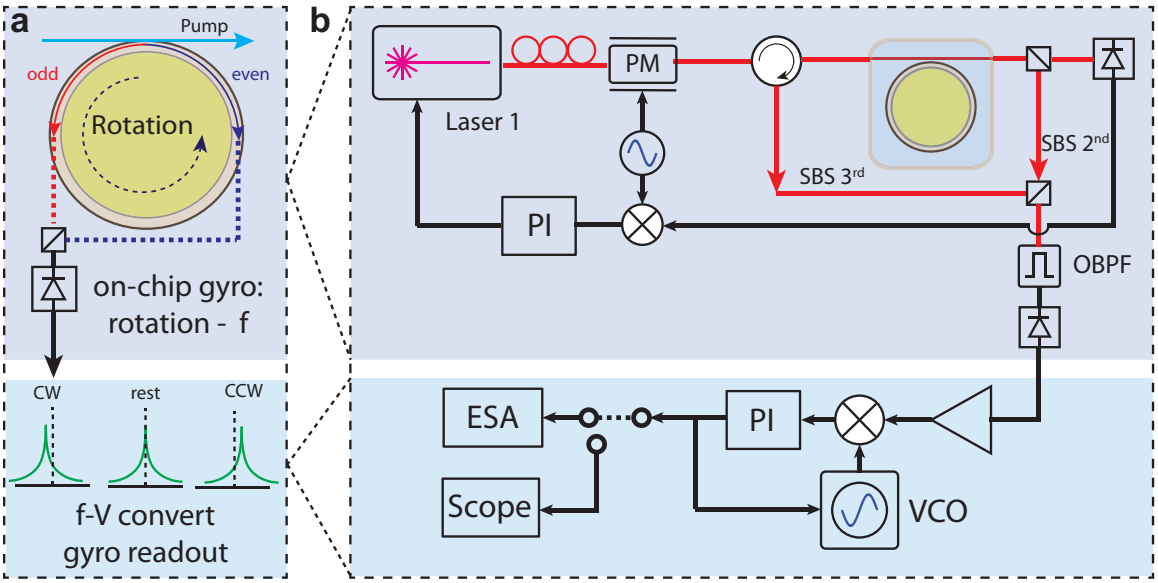

Figure 6.6: **Principle of Brillouin laser gyroscope operation and experimental setup.** (a) Simplified schematic illustrating principle of Brillouin laser gyroscope operation. Optical pumping (clockwise direction) induces Brillouin laser action which results in cascaded odd (counter-clockwise) and even (clockwise) order Stokes lasers. These lasing modes experience opposing Sagnac frequency shifts. Detection of the beat frequency of these co-lasing signals followed by a frequency-to-voltage readout (f-V) provides rotation sensing. Laser action on odd Stokes (red) and even Stokes (blue) lines is shown. Clockwise (CW), rest, and counter-clockwise (CCW) rotation induces beat frequency shifts as indicated. (b) Upper panel is a detailed experimental schematic for the gyroscope. The microcavity (yellow) is optically pumped. The laser pump is locked to a microcavity resonance using a Pound-Drever-Hall lock. Second-order and third-order Stokes co-lasing optical signals are coupled onto a photodetector using a circulator and bidirectional coupler. The laser lines are filtered using an optical band pass filter (OBPF) before detection. In the lower panel, the frequency-to-voltage readout system is shown. A voltage controlled oscillator (VCO) is phase locked to the detected beat frequency and the servo output provides a calibrated frequency readout. The readout is analyzed using an oscilloscope (scope) and an electrical spectrum analyzer (ESA). Also shown in the figure: PI, proportional integral servo; PM, phase modulator.

mode used for SBL generation has a loaded Q of 126 million. The pump threshold for the first Brillouin Stokes wave is about 250 W. Cascaded Brillouin Stokes laser action is generated to the third order when the pump power is increased to a few milliWatts. The second and the third Stokes waves are selected by an optical bandpass filter (OBPF) and the 10.872 GHz beatnote is detected. It is interesting to note that the lock-in effect commonly present in laser gyroscopes is not present in this case because the neighboring Stokes lasers are generated from distinct cavity modes separated by 10.872 GHz in frequency.

The lower panel in figure 6.6(b) shows how the gyro readout signal is created. Voltage-controlled-oscillator (VCO) is locked to the Brillouin beatnote using a proportional-integral (PI) servo loop. Because the servo output voltage is applied to the VCO tuning port with known tuning coefficient (10 kHz/V), the servo output voltage is proportional to the frequency change of the beatnote of Brillouin lasers and can be used as the gyro readout signal. The servo output voltage is analyzed on an electrical spectrum analyzer (ESA) or an oscilloscope.

To demonstrate the rotation sensing, the microresonator was packaged into a small copper box with FC/APC connectors as shown in figure 6.7(a) and a 7.5Hz sinusoidal rotation with angular amplitude of 0.14 degree is applied. The sinusoidal rotation was created by piezoelectrically pushing one side of the package while the opposite side was hinged. Figure 6.7(b-c) shows the gyro readout signal (servo output voltage) and the angular displacement signal. There is a π/2 phase shift between the gyro readout signal and the angular displacement signal because the SBL beatnote frequency change is proportional to the angular velocity (derivative of angular displacement). The sign of the gyro readout signal (Brillouin beat note change) indicates the direction of rotation.

The rotation sensitivity of the gyroscope is determined by the frequency noise of the Brillouin beat note within the VCO locking bandwidth, which can be measured from the servo output voltage using the electrical spectrum analyzer (ESA). According to the Sagnac effect, the rotation sensitivity ($\sqrt{S_{\delta\Omega}}$) of the gyroscope is related to the frequency noise ($\sqrt{S_{\delta\nu}}$) of the SBL beatnote : $\sqrt{S_{\delta\Omega}} = \frac{n\lambda}{D}\sqrt{S_{\delta\nu}}$, where n is the refractive index of the cavity medium (silica), λ is the vacuum wavelength of the laser, and D is the diameter of the microresonator. The blue noise spectrum in figure 6.8(a) shows the measured rotation

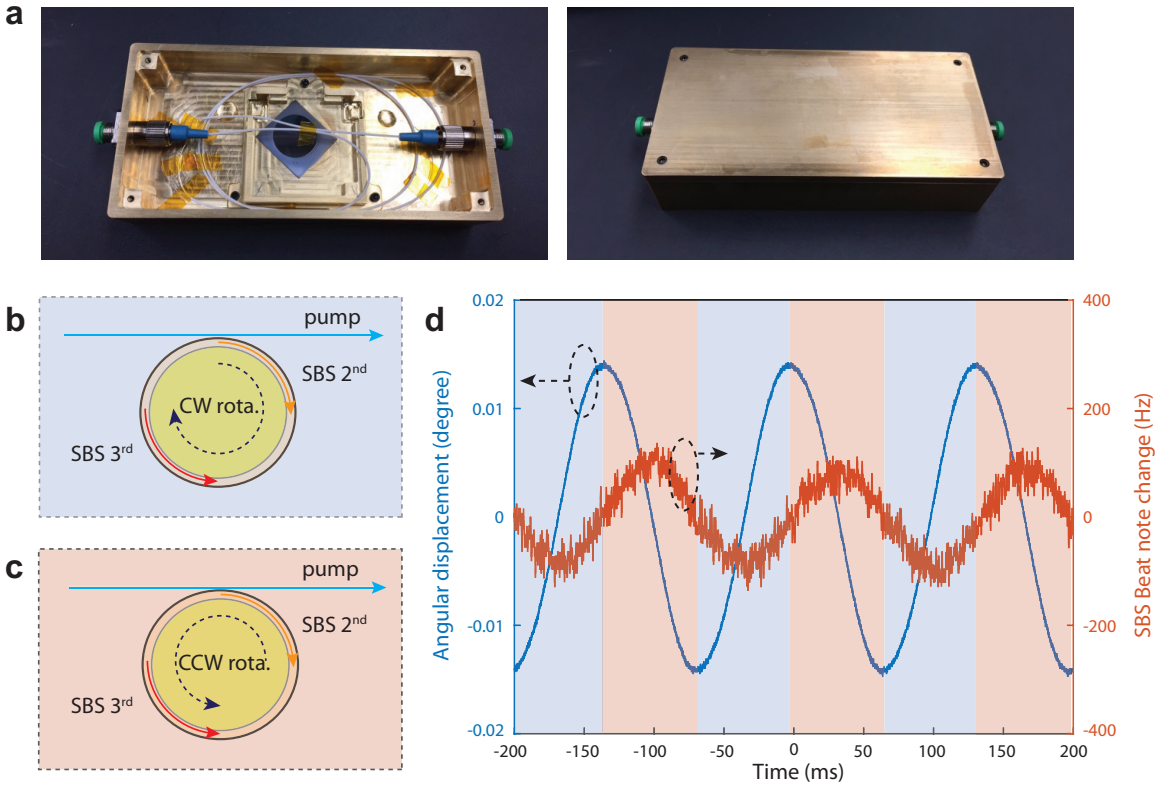

Figure 6.7: (a) The gyro resonator was packaged into a fiber-connectorized box for rotation measurement. Left panel shows the box with the lid removed and the 18mm diameter resonator visible as the grey silicon chip. (b-c) Clockwise (CW) rotation and counter-clockwise (CCW) rotation of the SBS gyroscope with second and third-order Stokes laser signals as indicated. Background coloring of the two rotation cases presented in (b) and (c) corresponds to the shaded regions in (d). (d) Time domain measurement of gyroscope output under sinusoidal rotation. Blue: angular displacement applied to the gyroscope; red: measured Sagnac frequency shift.

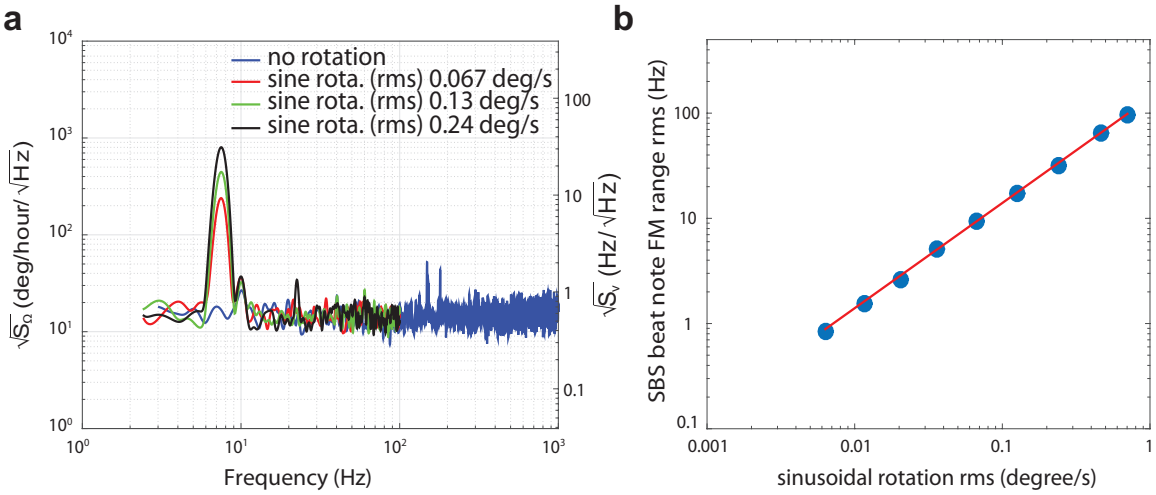

Figure 6.8: (a) Measurement of sinusoidal rotations using an electrical spectrum analyzer. (b) Measured rms Sagnac frequency shift versus rms angular rotation rate.

sensitivity of the gyroscope at rest. A white frequency noise of about 0.6 Hz/$\sqrt{Hz}$ (right axis) is measured from 3 Hz to 1 kHz offset, which corresponds to a rotation sensitivity of about 15 degree/hour/$\sqrt{Hz}$ (left axis).

When a sinusoidal rotation is applied to the gyroscope (as shown in figure 6.7(d), the servo output voltage also shows a sinusoidal modulation. Figure 6.8(a) shows the electrical spectrum of the gyroscope readout when the gyroscope rotates at 7.5 Hz with the following rms rotation rates: 0.24 deg/s (black curve), 0.13 deg/s (green curve), and 0.067 deg/s (red curve). The resolution bandwidth is 1 Hz. In figure 6.8(b), the blue circle markers represent the rms Sagnac frequencies plotted versus the rms angular rotation rate at the 7.5 Hz modulation frequency. The measurement shows a good agreement with the theoretical rms Sagnac frequency (red line) calculated from the Sagnac formula:

$$\delta\Omega = (n\lambda/D)\delta\nu, \tag{6.8}$$

where $\delta\Omega$ is the rotation rate and $\delta\nu$ is the frequency shift of the Brillouin beat note. Minimum rms rotation rate of 6.3 10^{-3} deg/s (or 22 deg/hour) is measured. Compared with the sensitivity of a passive micro-optical gyro (900 deg/hour, and gyro bandwidth of 9 Hz) [164], this value represents a 40-fold improvement in rotation sensitivity with $>$ 1 kHz

detection bandwidth.

In conclusion, a chip-based Brillouin gyroscope has been demonstrated with a sensitivity of 15 degree/hour/$\sqrt{Hz}$, a detection bandwidth of $>$1 kHz, and a minimum rotation rate of 22 deg/hour. Improvement of the SBL linewidth will proportionally improve the sensitivity of the gyroscope. In this work, the bias drift of the gyro readout signal remains large and efforts to reduce the bias drift should be made for practical application. With future improvements, this microresonator Brillouin gyroscope might compete with conventional bulk ring-laser gyros and fiber-optic gyros, while offering compact, lightweight, and low power consumption with improved immunity to shock and vibration.

Bibliography

[1] Hansuek Lee, Tong Chen, Jiang Li, Ki Youl Yang, Seokmin Jeon, Oskar Painter, and Kerry J Vahala. Chemically etched ultrahigh-q wedge-resonator on a silicon chip. *Nature Photonics*, 6(6):369–373, 2012.

[2] Ming Cai, Oskar Painter, and Kerry J Vahala. Observation of critical coupling in a fiber taper to a silica-microsphere whispering-gallery mode system. *Physical review letters*, 85(1):74, 2000.

[3] SM Spillane, TJ Kippenberg, OJ Painter, and KJ Vahala. Ideality in a fiber-taper-coupled microresonator system for application to cavity quantum electrodynamics. *Physical Review Letters*, 91(4):043902, 2003.

[4] Léon Brillouin. Diffusion de la lumière et des rayons x par un corps transparent homogène. influence de lagitation thermique. *Ann. Phys.(Paris)*, 17(88-122):21, 1922.

[5] Yo R Shen and N Bloembergen. Theory of stimulated brillouin and raman scattering. *Physical Review*, 137(6A):A1787, 1965.

[6] Robert W Boyd. *Nonlinear optics*. Academic press, 2003.

[7] Govind P Agrawal. *Nonlinear fiber optics*. Academic press, 2007.

[8] Andrew R Chraplyvy. Limitations on lightwave communications imposed by optical-fiber nonlinearities. *Journal of Lightwave Technology*, 8(10):1548–1557, 1990.

[9] LF Stokes, M Chodorow, and HJ Shaw. All-fiber stimulated brillouin ring laser with submilliwatt pump threshold. *Optics Letters*, 7(10):509–511, 1982.

[10] Yoshitomo Okawachi, Matthew S Bigelow, Jay E Sharping, Zhaoming Zhu, Aaron Schweinsberg, Daniel J Gauthier, Robert W Boyd, and Alexander L Gaeta. Tunable all-optical delays via brillouin slow light in an optical fiber. *Physical review letters*, 94(15):153902, 2005.

[11] Benjamin J Eggleton, Christopher G Poulton, and Ravi Pant. Inducing and harnessing stimulated brillouin scattering in photonic integrated circuits. *Advances in Optics and Photonics*, 5(4):536–587, 2013.

[12] M Tomes and T Carmon. Photonic micro-electromechanical systems vibrating at x-band (11-ghz) rates. *Physical Review Letters*, 102(11):113601, 2009.

[13] Jiang Li, Hansuek Lee, Tong Chen, and Kerry J Vahala. Characterization of a high coherence, brillouin microcavity laser on silicon. *Optics express*, 20(18):20170–20180, 2012.

[14] William Loh, Joe Becker, Daniel C Cole, Aurelien Coillet, Fred N Baynes, Scott B Papp, and Scott A Diddams. A microrod-resonator brillouin laser with 240 hz absolute linewidth. *New Journal of Physics*, 18(4):045001, 2016.

[15] Ivan S Grudinin, Andrey B Matsko, and Lute Maleki. Brillouin lasing with a caf 2 whispering gallery mode resonator. *Physical review letters*, 102(4):043902, 2009.

[16] Ravi Pant, Christopher G Poulton, Duk-Yong Choi, Hannah Mcfarlane, Samuel Hile, Enbang Li, Luc Thevenaz, Barry Luther-Davies, Stephen J Madden, and Benjamin J Eggleton. On-chip stimulated brillouin scattering. *Optics express*, 19(9):8285–8290, 2011.

[17] Eric A Kittlaus, Heedeuk Shin, and Peter T Rakich. Large brillouin amplification in silicon. *Nature Photonics*, 10:463–468, 2016.

[18] Moritz Merklein, Alvaro Casas-Bedoya, David Marpaung, Thomas F S Bu ttner, Mattia Pagani, Blair Morrison, Irina V Kabakova, and Benjamin J Eggleton. Stimulated brillouin scattering in photonic integrated circuits: Novel applications and devices. *IEEE Journal of Selected Topics in Quantum Electronics*, 22(2), 2016.

[19] Jiang Li, Hansuek Lee, and Kerry J Vahala. Microwave synthesizer using an on-chip brillouin oscillator. *Nature communications*, 4, 2013.

[20] Heedeuk Shin, Jonathan A Cox, Robert Jarecki, Andrew Starbuck, Zheng Wang, and Peter T Rakich. Control of coherent information via on-chip photonicphononic emitterreceivers. *Nature communications*, 6, 2015.

[21] Tobias J Kippenberg and Kerry J Vahala. Cavity optomechanics: back-action at the mesoscale. *Science*, 321(5893):1172–1176, 2008.

[22] Gaurav Bahl, Matthew Tomes, Florian Marquardt, and Tal Carmon. Observation of spontaneous brillouin cooling. *Nature Physics*, 8:203–207, 2012.

[23] JunHwan Kim, Mark C Kuzyk, Kewen Han, Hailin Wang, and Gaurav Bahl. Nonreciprocal brillouin scattering induced transparency. *Nature Physics*, 11(3):275–280, 2015.

[24] David J Jones, Scott A Diddams, Jinendra K Ranka, Andrew Stentz, Robert S Windeler, John L Hall, and Steven T Cundiff. Carrier-envelope phase control of femtosecond mode-locked lasers and direct optical frequency synthesis. *Science*, 288(5466):635–639, 2000.

[25] R Holzwarth, Th Udem, Th W Hänsch, JC Knight, WJ Wadsworth, and P St J Russell. Optical frequency synthesizer for precision spectroscopy. *Physical review letters*, 85(11):2264, 2000.

[26] Scott A Diddams, Th Udem, JC Bergquist, EA Curtis, RE Drullinger, L Hollberg, Wayne M Itano, WD Lee, CW Oates, KR Vogel, et al. An optical clock based on a single trapped 199hg+ ion. *Science*, 293(5531):825–828, 2001.

[27] P DelHaye, A Schliesser, O Arcizet, T Wilken, R Holzwarth, and TJ Kippenberg. Optical frequency comb generation from a monolithic microresonator. *Nature*, 450(7173):1214–1217, 2007.

[28] Tobias J Kippenberg, Ronald Holzwarth, and SA Diddams. Microresonator-based optical frequency combs. *Science*, 332(6029):555–559, 2011.

[29] Ivan S Grudinin, Nan Yu, and Lute Maleki. Generation of optical frequency combs with a caf 2 resonator. *Optics letters*, 34(7):878–880, 2009.

[30] Scott B Papp and Scott A Diddams. Spectral and temporal characterization of a fused-quartz-microresonator optical frequency comb. *Physical Review A*, 84(5):053833, 2011.

[31] Yoshitomo Okawachi, Kasturi Saha, Jacob S Levy, Y Henry Wen, Michal Lipson, and Alexander L Gaeta. Octave-spanning frequency comb generation in a silicon nitride chip. *Optics letters*, 36(17):3398–3400, 2011.

[32] Jiang Li, Hansuek Lee, Tong Chen, and Kerry J Vahala. Low-pump-power, low-phase-noise, and microwave to millimeter-wave repetition rate operation in microcombs. *Physical review letters*, 109(23):233901, 2012.

[33] BJM Hausmann, I Bulu, V Venkataraman, P Deotare, and M Lončar. Diamond nonlinear photonics. *Nature Photonics*, 8(5):369–374, 2014.

[34] L Razzari, D Duchesne, M Ferrera, R Morandotti, S Chu, BE Little, and DJ Moss. Cmos-compatible integrated optical hyper-parametric oscillator. *Nature Photonics*, 4(1):41–45, 2010.

[35] Fahmida Ferdous, Houxun Miao, Daniel E Leaird, Kartik Srinivasan, Jian Wang, Lei Chen, Leo Tom Varghese, and Andrew M Weiner. Spectral line-by-line pulse shaping of on-chip microresonator frequency combs. *Nature Photonics*, 5(12):770–776, 2011.

[36] Hojoong Jung, Chi Xiong, King Y Fong, Xufeng Zhang, and Hong X Tang. Optical frequency comb generation from aluminum nitride microring resonator. *Optics letters*, 38(15):2810–2813, 2013.

[37] TJ Kippenberg, SM Spillane, and KJ Vahala. Kerr-nonlinearity optical parametric oscillation in an ultrahigh-q toroid microcavity. *Physical review letters*, 93(8):083904, 2004.

[38] Anatoliy A Savchenkov, Andrey B Matsko, Dmitry Strekalov, Makan Mohageg, Vladimir S Ilchenko, and Lute Maleki. Low threshold optical oscillations in a whispering gallery mode c a f 2 resonator. *Physical review letters*, 93(24):243905, 2004.

[39] T Herr, V Brasch, JD Jost, CY Wang, NM Kondratiev, ML Gorodetsky, and TJ Kippenberg. Temporal solitons in optical microresonators. *Nature Photonics*, 8(2):145–152, 2014.

[40] Xu Yi, Qi-Fan Yang, Ki Youl Yang, Myoung-Gyun Suh, and Kerry Vahala. Soliton frequency comb at microwave rates in a high-q silica microresonator. *Optica*, 2(12):1078–1085, 2015.

[41] V Brasch, M Geiselmann, T Herr, G Lihachev, MHP Pfeiffer, ML Gorodetsky, and TJ Kippenberg. Photonic chip–based optical frequency comb using soliton cherenkov radiation. *Science*, 351(6271):357–360, 2016.

[42] Pei-Hsun Wang, Jose A Jaramillo-Villegas, Yi Xuan, Xiaoxiao Xue, Chengying Bao, Daniel E Leaird, Minghao Qi, and Andrew M Weiner. Intracavity characterization of micro-comb generation in the single-soliton regime. *Optics Express*, 24(10):10890–10897, 2016.

[43] Chaitanya Joshi, Jae K Jang, Kevin Luke, Xingchen Ji, Steven A Miller, Alexander Klenner, Yoshitomo Okawachi, Michal Lipson, and Alexander L Gaeta. Thermally controlled comb generation and soliton modelocking in microresonators. *Optics letters*, 41(11):2565–2568, 2016.

[44] JD Jost, T Herr, C Lecaplain, V Brasch, MHP Pfeiffer, and TJ Kippenberg. Counting the cycles of light using a self-referenced optical microresonator. *Optica*, 2(8):706–711, 2015.

[45] Pascal Del'Haye, Aurélien Coillet, Tara Fortier, Katja Beha, Daniel C Cole, Ki Youl Yang, Hansuek Lee, Kerry J Vahala, Scott B Papp, and Scott A Diddams. Phase-coherent microwave-to-optical link with a self-referenced microcomb. *Nature Photonics*, 10(8):516–520, 2016.

[46] Stefan Wabnitz. Suppression of interactions in a phase-locked soliton optical memory. *Optics letters*, 18(8):601–603, 1993.

[47] Andrey B Matsko and Lute Maleki. On timing jitter of mode locked kerr frequency combs. *Optics express*, 21(23):28862–28876, 2013.

[48] Xu Yi, Qi-Fan Yang, Ki Youl, and Kerry Vahala. Active capture and stabilization of temporal solitons in microresonators. *Optics letters*, 41(9):2037–2040, 2016.

[49] François Leo, Lendert Gelens, Philippe Emplit, Marc Haelterman, and Stéphane Coen. Dynamics of one-dimensional kerr cavity solitons. *Optics express*, 21(7):9180–9191, 2013.

[50] Mengjie Yu, Jae K Jang, Yoshitomo Okawachi, Austin G Griffith, Kevin Luke, Steven A Miller, Xingchen Ji, Michal Lipson, and Alexander L Gaeta. Breather soliton dynamics in microresonators. *Nature Communications*, 8, 2017.

[51] Chengying Bao, Jose Jaramillo-Villegas, Yi Xuan, Daniel E Leaird, Minghao Qi, and Andrew M Weiner. Observation of fermi-pasta-ulam recurrence in an on-chip optical microresonator. *arXiv preprint arXiv:1606.06788*, 2016.

[52] Erwan Lucas, Maxim Karpov, Hairun Guo, Michael Gorodetsky, and Tobias Kippenberg. Breathing dissipative solitons in optical microresonators. *arXiv preprint arXiv:1611.06567*, 2016.

[53] S Schiller. Spectrometry with frequency combs. *Optics letters*, 27(9):766–768, 2002.

[54] Fritz Keilmann, Christoph Gohle, and Ronald Holzwarth. Time-domain mid-infrared frequency-comb spectrometer. *Optics letters*, 29(13):1542–1544, 2004.

[55] Ian Coddington, William C Swann, and Nathan R Newbury. Coherent multiheterodyne spectroscopy using stabilized optical frequency combs. *Physical Review Letters*, 100(1):013902, 2008.

[56] Philippe Giaccari, Jean-Daniel Deschênes, Philippe Saucier, Jerome Genest, and Pierre Tremblay. Active fourier-transform spectroscopy combining the direct rf beating of two fiber-based mode-locked lasers with a novel referencing method. *Optics express*, 16(6):4347–4365, 2008.

[57] Birgitta Bernhardt, Akira Ozawa, Patrick Jacquet, Marion Jacquey, Yohei Kobayashi, Thomas Udem, Ronald Holzwarth, Guy Guelachvili, Theodor W Hänsch, and Nathalie Picqué. Cavity-enhanced dual-comb spectroscopy. *Nature Photonics*, 4(1):55–57, 2010.

[58] Takuro Ideguchi, Antonin Poisson, Guy Guelachvili, Nathalie Picqué, and Theodor W Hänsch. Adaptive real-time dual-comb spectroscopy. *Nature communications*, 5, 2014.

[59] Ian Coddington, Nathan Newbury, and William Swann. Dual-comb spectroscopy. *Optica*, 3(4):414–426, 2016.

[60] Andreas Hugi, Gustavo Villares, Stéphane Blaser, HC Liu, and Jérôme Faist. Mid-infrared frequency comb based on a quantum cascade laser. *Nature*, 492(7428):229–233, 2012.

[61] Gustavo Villares, Andreas Hugi, Stéphane Blaser, and Jérôme Faist. Dual-comb spectroscopy based on quantum-cascade-laser frequency combs. *Nature communications*, 5, 2014.

[62] Mengjie Yu, Yoshitomo Okawachi, Austin Griffith, Michal Lipson, and Alexander L Gaeta. Silicon-microresonator-based mid-infrared dual-comb source. In *CLEO: Science and Innovations*, pages JTh4B–5. Optical Society of America, 2016.

[63] Ki Youl Yang, Katja Beha, Daniel C Cole, Xu Yi, Pascal Del'Haye, Hansuek Lee, Jiang Li, Dong Yoon Oh, Scott A Diddams, Scott B Papp, et al. Broadband dispersion engineered microresonator on-a-chip. *Nature Photonics*, 10(10):316–320, 2016.

[64] Qi-Fan Yang, Xu Yi, Ki Youl Yang, and Kerry Vahala. Stokes solitons in optical microcavities. *Nature Physics*, 2016.

[65] https://www.eia.gov.

[66] https://www.epa.gov/ghgemissions/overview-greenhouse-gases.

[67] Drew T Shindell, Greg Faluvegi, Dorothy M Koch, Gavin A Schmidt, Nadine Unger, and Susanne E Bauer. Improved attribution of climate forcing to emissions. *Science*, 326(5953):716–718, 2009.

[68] Christopher R Webster, Paul R Mahaffy, Sushil K Atreya, Gregory J Flesch, Michael A Mischna, Pierre-Yves Meslin, Kenneth A Farley, Pamela G Conrad, Lance E Christensen, Alexander A Pavlov, et al. Mars methane detection and variability at gale crater. *Science*, 347(6220):415–417, 2015.

[69] Vladimir A Krasnopolsky, Jean Pierre Maillard, and Tobias C Owen. Detection of methane in the martian atmosphere: evidence for life? *Icarus*, 172(2):537–547, 2004.

[70] Vittorio Formisano, Sushil Atreya, Thérèse Encrenaz, Nikolai Ignatiev, and Marco Giuranna. Detection of methane in the atmosphere of mars. *Science*, 306(5702):1758–1761, 2004.

[71] Franck Lefevre and François Forget. Observed variations of methane on mars unexplained by known atmospheric chemistry and physics. *Nature*, 460(7256):720–723, 2009.

[72] S Capone, A Forleo, L Francioso, R Rella, P Siciliano, J Spadavecchia, DS Presicce, and AM Taurino. Solid state gas sensors: state of the art and future activities. *Journal of Optoelectronics and Advanced Materials*, 5(5):1335–1348, 2003.

[73] PK Basu, SK Jana, H Saha, and S Basu. Low temperature methane sensing by electrochemically grown and surface modified zno thin films. *Sensors and Actuators B: Chemical*, 135(1):81–88, 2008.

[74] A Biaggi-Labiosa, F Sola, M Lebrón-Colón, LJ Evans, JC Xu, GW Hunter, GM Berger, and JM Gonzalez. A novel methane sensor based on porous sno2 nanorods: room temperature to high temperature detection. *Nanotechnology*, 23(45):455501, 2012.

[75] Edmond De Hoffmann and Vincent Stroobant. *Mass spectrometry: principles and applications*. John Wiley & Sons, 2007.

[76] Robert P Adams et al. *Identification of essential oil components by gas chromatography/mass spectrometry.* Number Ed. 4. Allured publishing corporation, 2007.

[77] Norman Bobroff. Recent advances in displacement measuring interferometry. *Measurement Science and Technology*, 4(9):907, 1993.

[78] Kaoru Minoshima and Hirokazu Matsumoto. High-accuracy measurement of 240-m distance in an optical tunnel by use of a compact femtosecond laser. *Applied Optics*, 39(30):5512–5517, 2000.

[79] Steven M Beck, Joseph R Buck, Walter F Buell, Richard P Dickinson, David A Kozlowski, Nicholas J Marechal, and Timothy J Wright. Synthetic-aperture imaging laser radar: laboratory demonstration and signal processing. *Applied optics*, 44(35):7621–7629, 2005.

[80] I Coddington, WC Swann, L Nenadovic, and NR Newbury. Rapid and precise absolute distance measurements at long range. *Nature photonics*, 3(6):351–356, 2009.

[81] Yves Salvadé, Nicolas Schuhler, Samuel Lévêque, and Sébastien Le Floch. High-accuracy absolute distance measurement using frequency comb referenced multi-wavelength source. *Applied Optics*, 47(14):2715–2720, 2008.

[82] Esther Baumann, Fabrizio R Giorgetta, Ian Coddington, Laura C Sinclair, Kevin Knabe, William C Swann, and Nathan R Newbury. Comb-calibrated frequency-modulated continuous-wave ladar for absolute distance measurements. *Optics letters*, 38(12):2026–2028, 2013.

[83] Joohyung Lee, Young-Jin Kim, Keunwoo Lee, Sanghyun Lee, and Seung-Woo Kim. Time-of-flight measurement with femtosecond light pulses. *Nature photonics*, 4(10):716–720, 2010.

[84] Daryl T Spencer, Aaron Bluestone, John E Bowers, Travis C Briles, Scott Diddams, Tara Drake, Robert Ilic, Tobias Kippenberg, Seung H Lee, Qing Li, et al. Towards an integrated-photonics optical-frequency synthesizer with¡ 1 hz residual frequency noise. In *Optical Fiber Communication Conference*, pages M2J–2. Optical Society of America, 2017.

[85] Myoung-Gyun Suh, Qi-Fan Yang, Ki Youl Yang, Xu Yi, and Kerry J Vahala. Microresonator soliton dual-comb spectroscopy. *Science*, 354(6312):600–603, 2016.

[86] Avik Dutt, Chaitanya Joshi, Xingchen Ji, Jaime Cardenas, Yoshitomo Okawachi, Kevin Luke, Alexander L Gaeta, and Michal Lipson. On-chip dual comb source for spectroscopy. *arXiv preprint arXiv:1611.07673*, 2016.

[87] NG Pavlov, G Lihachev, S Koptyaev, E Lucas, M Karpov, NM Kondratiev, IA Bilenko, TJ Kippenberg, and ML Gorodetsky. Soliton dual frequency combs in crystalline microresonators. *Optics Letters*, 42(3):514–517, 2017.

[88] Qi-Fan Yang, Xu Yi, Kiyoul Yang, and Kerry Vahala. Counter-propagating solitons in microresonators. *arXiv preprint arXiv:1704.08409*, 2017.

[89] Ki Youl Yang, Dong Yoon Oh, Seung Hoon Lee, Qi-Fan Yang, Xu Yi, and Kerry Vahala. Integrated ultra-high-q optical resonator. *arXiv preprint arXiv:1702.05076*, 2017.

[90] TW Hansch and B Couillaud. Laser frequency stabilization by polarization spectroscopy of a reflecting reference cavity. *Optics communications*, 35(3):441–444, 1980.

[91] RWP Drever, John L Hall, FV Kowalski, J Hough, GM Ford, AJ Munley, and H Ward. Laser phase and frequency stabilization using an optical resonator. *Applied Physics B*, 31(2):97–105, 1983.

[92] Tara M Fortier, Matthew S Kirchner, F Quinlan, J Taylor, JC Bergquist, T Rosenband, N Lemke, A Ludlow, Y Jiang, CW Oates, et al. Generation of ultrastable microwaves via optical frequency division. *Nature Photonics*, 5(7):425–429, 2011.

[93] BP Abbott, R Abbott, R Adhikari, P Ajith, Bruce Allen, G Allen, RS Amin, SB Anderson, WG Anderson, MA Arain, et al. Ligo: the laser interferometer gravitational-wave observatory. *Reports on Progress in Physics*, 72(7):076901, 2009.

[94] B. C. Young, F. C. Cruz, W. M. Itano, and J. C. Bergquist. Visible lasers with subhertz linewidths. *Physical Reivew Letters*, 82:3799–3802, 1999.

[95] T. Kessler, C. Hagemann, C. Grebing, T. Legero, U. Sterr, F. Riehle, M. J. Martin, L. Chen, and J. Ye. A sub-40-mHz-linewidth laser based on a silicon single-crystal optical cavity. *Nature Photonics*, 6:687–692, 2012.

[96] Y. Y Jiang, A. D. Ludlow, N. D. Lemke, R. W. Fox, J. A. Sherman, L. S. Ma, and C. W. Oates. Making optical atomic clocks more stable with 10^{-16}-level laser stabilization. *Nature Photonics*, 5:158–161, 2011.

[97] P. B. Sellin, N. M. Strickland, J. L. Carlsten, and R. L. Cone. Programmable frequency reference for subkilohertz laser stabilization by use of persistent spectral hole burning. *Optics Letters*, 24:1038–1040, 1999.

[98] M. J. Thorpe, L. Rippe, T. M. Fortier, M. S. Kirchner, and T. Rosenband. Frequency stabilization to 6x10^{-16} via spectral-hole burning. *Nature Photonics*, 8:688–693, 2011.

[99] B. P. Abbott, R. Abbott, R. Adhikari, P. Ajith, B. Allen, G. Allen, R. S. Amin, S. B. Anderson, W. G. Anderson, M. A. Arain, M. Araya, and H. Armandula. LIGO: the

laser interferometer gravitational-wave observatory. *Reports on Progress in Physics*, 72:076901, 2009.

[100] F. Kefelian, H. Jiang, P. Lemonde, and G. Santarelli. Ultralow-frequency-noise stabilization of a laser by locking to an optical fiber-delay line. *Optics Letters*, 34:914–916, 2009.

[101] K. Numata, A. Kemery, and J. Camp. Thermal-noise limit in the frequency stabilization of lasers with rigid cavities. *Physical Review Letters*, 93:250602, 2004.

[102] et al Harry, G. M. Thermal noise in interferometric gravitational wave detectors due to dielectric optical coatings. *Class. Quantum Grav.*, 19:897–917, 2002.

[103] Mark Notcutt, Long-Sheng Ma, Jun Ye, and John L Hall. Simple and compact 1-hz laser system via an improved mounting configuration of a reference cavity. *Optics letters*, 30(14):1815–1817, 2005.

[104] David R Leibrandt, Michael J Thorpe, Mark Notcutt, Robert E Drullinger, Till Rosenband, and James C Bergquist. Spherical reference cavities for frequency stabilization of lasers in non-laboratory environments. *Optics express*, 19(4):3471–3482, 2011.

[105] D. K. Armani, T. J. Kippenberg, S. M. Spillane, and K. J Vahala. Ultra-high-Q toroid microcavity on a chip. *Nature*, 421:925–928, 2003.

[106] S. B. Papp and S. A. Diddams. Spectral and temporal characterization of a fused-quartz-microresonator optical frequency comb. *Physical Review A*, 84:053833, 2011.

[107] H. Lee, T. Chen, J. Li, K. Yang, S. Jeon, O. Painter, and K. Vahala. Chemically etched, ulta-high-Q resonator on a chip. *Nature Photonics*, 6:369–373, 2012.

[108] I. S. Grudinin, V. S. Ilchenko, and L. Maleki. Ultrahigh optical Q factors of crystalline resonators in the linear regime. *Physical Review A*, 74:063806, 2006.

[109] I. S. Grudinin, A. B. Matsko, and L. Maleki. On the fundamental limits of Q factor of crystalline dielectric resonators. *Optics Express*, 15:3390–3395, 2007.

[110] A. A. Savchenkov, A. B. Matsko, V. S. Ilchenko, and L. Maleki. Optical resonators with ten million finesse. *Optics Express*, 15:6768–6773, 2007.

[111] Janis Alnis, Albert Schliesser, Christine Y Wang, Johannes Hofer, Tobias J Kippenberg, and TW Hänsch. Thermal-noise-limited crystalline whispering-gallery-mode resonator for laser stabilization. *Physical Review A*, 84(1):011804, 2011.

[112] Hansuek Lee, Myoung-Gyun Suh, Tong Chen, Jiang Li, Scott A Diddams, and Kerry J Vahala. Spiral resonators for on-chip laser frequency stabilization. *Nature communications*, 4, 2013.

[113] W Liang, VS Ilchenko, D Eliyahu, AA Savchenkov, AB Matsko, D Seidel, and L Maleki. Ultralow noise miniature external cavity semiconductor laser. *Nature communications*, 6, 2015.

[114] M. L. Gorodetsky and I. S. Grudinin. Fundamental thermal fluctuations in microspheres. *J. Opt. Soc. Am. B*, 21:697–705, 2004.

[115] A. B. Matsko, A. A. Savchenkov, N. Yu, and L. Maleki. Whispering-gallery-mode resonators as frequency references. I. fundamental limitations. *J. Opt. Soc. Am. B*, 24:1324–1335, 2007.

[116] J. Alnis, A. Schliesser, C. Y. Wang, J. Hofer, T. J. Kippenberg, and T. W. Hnsch. Thermal-noise-limited crystalline whispering-gallery-mode resonator for laser stabilization. *Physical Review A*, 84:011804, 2011.

[117] A. A. Savchenkov, A. B. Matsko, V. S. Ilchenko, N. Yu, and L. Maleki. Whispering-gallery-mode resonators as frequency references. II. stabilization. *J. Opt. Soc. Am. B*, 24:2988–2997, 2007.

[118] D. V. Strekalov, R. J. Thompson, L. M. Baumgartel, I. S. Grudinin, and N. Yu. Temperature measurement and stabilization in a birefringent whispering gallery mode resonator. *Optics Express*, 19:14495–14501, 2011.

[119] I. Fescenko, J. Alnis, A. Schliesser, C. Y. Wang, T. J. Kippenberg, and T. W. Hansch. Dual-mode temperature compensation technique for laser stabilization to a crystalline whispering gallery mode resonator. *Optics Express*, 20:19185–19193, 2012.

[120] R. W. P. Drever, J. L. Hall, F. V. Kowalski, J. Hough, G. M. Ford, A. J. Munley, and H. Ward. Laser phase and frequency stabilization using an optical resonator. *Applied Physics B*, 31:97–105, 1983.

[121] D. R. Hjelme, A. R. Mickelson, and R. G. Beausoleil. Semiconductor laser stabilization by external optical feedback. *Journal of Quntum Electronics*, 27:352–372, 1991.

[122] D.-X. Xu, A. Delage, R. McKinnon, M. Vachon, R. Ma, J. Lapointe, A. Densmore, P. Cheben, S. Janz, and J. H. Schmid. Archimedean spiral cavity ring resonators in silicon as ultra-compact optical comb filters. *Optics Express*, 18:1937–1945, 2010.

[123] H. Lee, T. Chen, J. Li, O. Painter, and K. Vahala. Ultra-low-loss optical delay line on a silicon chip. *Nature Communications*, 3:867, 2012.

[124] M. Cai, O. Painter, and K. J. Vahala. Observation of critical coupling in a fiber taper to silica-microsphere whispering gallery mode system. *Physical Review Letters*, 85:74–77, 2000.

[125] S. M. Spillane, T. J. Kippenberg, O. J. Painter, and K. J. Vahala. Observation of critical coupling in a fiber taper to silica-microsphere whispering gallery mode system. *Physical Review Letters*, 85:74–77, 2000.

[126] T. Chen, H. Lee, J. Li, and K. Vahala. A general design algorithm for low optical loss adiabatic connections in waveguides. *Optics Express*, 20:22819–22829, 2012.

[127] T. J. Kippenberg and K. J. Vahala. Cavity optomechanics: Back-action at the mesoscale. *Science*, 321:1172–1176, 2008.

[128] Dag Roar Hjelme, Alan Rolf Mickelson, and Raymond G Beausoleil. Semiconductor laser stabilization by external optical feedback. *IEEE Journal of Quantum Electronics*, 27(3):352–372, 1991.

[129] J. A. Barnes, A. R. Chi, L. S. Cutler, D. J. Healey, D. B. Leeson, T. E. McGunigal, J. A. Mullen, JR., W. L. Smith, R. L. Sydnor, R. F. C. Vessot, and G. M. R. Winkler. Characterization of frequency stability. *IEEE Transactions on Instrumentation and Measurement*, 20:105–120, 1971.

[130] T. W. Hänsch and B. Couillaud. Laser frequency stabilization by polarization spectroscopy of a reflecting reference cavity. *Optics Communications*, 35:441–444, 1980.

[131] A. Schliesser, R. Riviere, G. Anetsberger, O. Arcizet, and T. J. Kippenberg. Resolved-sideband cooling of a micromechanical oscillator. *Nature Physics*, 4:415–419, 2008.

[132] Michael L Gorodetsky and Ivan S Grudinin. Fundamental thermal fluctuations in microspheres. *JOSA B*, 21(4):697–705, 2004.

[133] Andrey B Matsko, Anatoliy A Savchenkov, Nan Yu, and Lute Maleki. Whispering-gallery-mode resonators as frequency references. i. fundamental limitations. *JOSA B*, 24(6):1324–1335, 2007.

[134] James A Barnes, Andrew R Chi, Leonard S Cutler, Daniel J Healey, David B Leeson, Thomas E McGunigal, James A Mullen, Warren L Smith, Richard L Sydnor, Robert FC Vessot, et al. Characterization of frequency stability. *IEEE transactions on instrumentation and measurement*, 1001(2):105–120, 1971.

[135] A. Hati, C.W. Nelson, C. Barnes, D. Lirette, J.A. DeSalvo, T. Fortier, F. Quinlan, A. Ludlow, T. Rosenband, S.A. Diddams, and D.A. Howe. Ultra-low-noise regenerative frequency divider for high-spectral-purity RF signal generation. In *Frequency Control Symposium (FCS), 2012 IEEE International,*, 2012.

[136] Joerg Pfeifle, Victor Brasch, Matthias Lauermann, Yimin Yu, Daniel Wegner, Tobias Herr, Klaus Hartinger, Philipp Schindler, Jingshi Li, David Hillerkuss, et al. Coherent terabit communications with microresonator kerr frequency combs. *Nature photonics*, 8(5):375–380, 2014.

[137] C. J. Karlsson, F. A. A. Olsson, D. Letalick, and M. Harris. All-fiber multifunction continuous-wave coherent laser radar at 1.55 μm for range, speed, vibration, and wind measurements. *Applied Optics*, 39:3716–3726, 2000.

[138] R. J. Rafac, B. C. Young, J. A. Beall, W. M. Itano, D. J. Wineland, and J. C. Bergquist. Sub-dekahertz ultraviolet spectroscopy of $^{199}Hg^{+}$. *Physical Reivew Letters*, 85:2462–2465, 2000.

[139] Grégoire Pillet, Loic Morvan, Marc Brunel, Fabien Bretenaker, Daniel Dolfi, Marc Vallet, Jean-Pierre Huignard, and Albert Le Floch. Dual-frequency laser at 1.5 μm for optical distribution and generation of high-purity microwave signals. *Journal of Lightwave Technology*, 26(15):2764–2773, 2008.

[140] Jihong Geng, Sean Staines, and Shibin Jiang. Dual-frequency brillouin fiber laser for optical generation of tunable low-noise radio frequency/microwave frequency. *Optics letters*, 33(1):16–18, 2008.

[141] Shilong Pan and Jianping Yao. A wavelength-switchable single-longitudinal-mode dual-wavelength erbium-doped fiber laser for switchable microwave generation. *Optics express*, 17(7):5414–5419, 2009.

[142] Michael C Gross, Patrick T Callahan, Thomas R Clark, Dalma Novak, Rodney B Waterhouse, and Michael L Dennis. Tunable millimeter-wave frequency synthesis up to 100 ghz by dual-wavelength brillouin fiber laser. *Optics express*, 18(13):13321–13330, 2010.

[143] Patrick T Callahan, Michael C Gross, and Michael L Dennis. Frequency-independent phase noise in a dual-wavelength brillouin fiber laser. *IEEE Journal of Quantum Electronics*, 47(8):1142–1150, 2011.

[144] Guillermo Carpintero, Efthymios Rouvalis, Katarzyna Ławniczuk, Martyn Fice, Cyril C Renaud, Xaveer JM Leijtens, Erwin AJM Bente, Mourad Chitoui, Frederic Van Dijk, and Alwyn J Seeds. 95 ghz millimeter wave signal generation using an arrayed waveguide grating dual wavelength semiconductor laser. *Optics letters*, 37(17):3657–3659, 2012.

[145] William C Swann, Esther Baumann, Fabrizio R Giorgetta, and Nathan R Newbury. Microwave generation with low residual phase noise from a femtosecond fiber laser with an intracavity electro-optic modulator. *Optics express*, 19(24):24387–24395, 2011.

[146] Giorgio Santarelli, Ph Laurent, Pierre Lemonde, André Clairon, Anthony G Mann, S Chang, Andre N Luiten, and Christophe Salomon. Quantum projection noise in an atomic fountain: A high stability cesium frequency standard. *Physical Review Letters*, 82(23):4619, 1999.

[147] S Weyers, B Lipphardt, and H Schnatz. Reaching the quantum limit in a fountain clock using a microwave oscillator phase locked to an ultrastable laser. *Physical Review A*, 79(3):031803, 2009.

[148] J Millo, M Abgrall, M Lours, EML English, H Jiang, J Guéna, A Clairon, ME Tobar, S Bize, Y Le Coq, et al. Ultralow noise microwave generation with fiber-based optical frequency comb and application to atomic fountain clock. *Applied Physics Letters*, 94(14):141105, 2009.

[149] George C Valley. Photonic analog-to-digital converters. *Optics Express*, 15(5):1955–1982, 2007.

[150] Jim Scheer and James L Kurtz. *Coherent radar performance estimation*. Boston: Artech House, 2012.

[151] Scott B Papp, Katja Beha, Pascal DelHaye, Franklyn Quinlan, Hansuek Lee, Kerry J Vahala, and Scott A Diddams. Microresonator frequency comb optical clock. *Optica*, 1(1):10–14, 2014.

[152] Jiang Li, Xu Yi, Hansuek Lee, Scott A Diddams, and Kerry J Vahala. Electro-optical frequency division and stable microwave synthesis. *Science*, 345(6194):309–313, 2014.

[153] J Li, X Yi, H Lee, SA Diddams, and KJ Vahala. Electro-optical frequency division and stable microwave synthesis. 2014.

[154] RWP Drever, JL Hall, FV Kowalski, J Hough, and GM Ford. Laser phase and frequency stabilization using an optical resonator. 1983.

[155] Jiang Li, Myoung Gyun Suh, and Kerry Vahala. Microresonator brillouin gyroscope. *Optica*, 4(3):346–348, 2017.

[156] Amnon Yariv. *Quantum Electronics, 3rd Edition*. Wiley, 1989.

[157] Andrey Kobyakov, Shiva Kumar, Dipak Q Chowdhury, A Boh Ruffin, Michael Sauer, Scott R Bickham, and Raj Mishra. Design concept for optical fibers with enhanced sbs threshold. *Optics Express*, 13(14):5338–5346, 2005.

[158] S Le Floch and P Cambon. Study of brillouin gain spectrum in standard single-mode optical fiber at low temperatures (1.4–370 k) and high hydrostatic pressures (1–250 bars). *Optics communications*, 219(1):395–410, 2003.

[159] WW Chow, J Gea-Banacloche, LM Pedrotti, VE Sanders, Wo Schleich, and MO Scully. The ring laser gyro. *Reviews of Modern Physics*, 57(1):61, 1985.

[160] Herve C Lefevre. *The fiber-optic gyroscope*. Artech house, 2014.

[161] Kai Liu, Weiping Zhang, Wenyuan Chen, Kai Li, Fuyan Dai, Feng Cui, Xiaosheng Wu, Gaoyin Ma, and Qijun Xiao. The development of micro-gyroscope technology. *Journal of Micromechanics and Microengineering*, 19(11):113001, 2009.

[162] F Zarinetchi, SP Smith, and S Ezekiel. Stimulated brillouin fiber-optic laser gyroscope. *Optics letters*, 16(4):229–231, 1991.

[163] G Sagnac. The demonstration of the luminiferous aether by an interferometer in uniform rotation. *C. R Acad. Sci*, 157:708, 1913.

[164] Huilian Ma, Wenyi Wang, Yang Ren, and Zhonghe Jin. Low-noise low-delay digital signal processor for resonant micro optic gyro. *IEEE Photonics Technology Letters*, 25(2):198–201, 2013.